



JAN 27 1995  
ORNL/Sub/87-SB045/2

**OAK RIDGE  
NATIONAL  
LABORATORY**

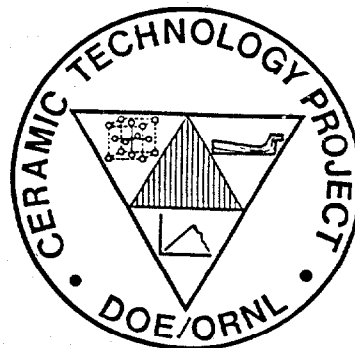
**MARTIN MARIETTA**

**ANALYTICAL AND EXPERIMENTAL  
EVALUATION OF JOINING SILICON  
CARBIDE TO SILICON CARBIDE AND  
SILICON NITRIDE TO SILICON NITRIDE  
FOR ADVANCED HEAT ENGINE  
APPLICATIONS PHASE II**

**FINAL REPORT**

Glenn J. Sundberg  
Ara M. Vartabedian  
Jon A. Wade  
Charles S. White

*CERAMIC TECHNOLOGY PROJECT*



MANAGED BY  
MARTIN MARIETTA ENERGY SYSTEMS, INC.  
FOR THE UNITED STATES  
DEPARTMENT OF ENERGY

This report has been reproduced directly from the best available copy.

Available to DOE and DOE contractors from the Office of Scientific and Technical Information, P.O. Box 62, Oak Ridge, TN 37831; prices available from (615) 576-8401, FTS 626-8401.

Available to the public from the National Technical Information Service, U.S. Department of Commerce, 5285 Port Royal Rd., Springfield, VA 22161.

This report was prepared as an account of work sponsored by an agency of the United States Government. Neither the United States Government nor any agency thereof, nor any of their employees, makes any warranty, express or implied, or assumes any legal liability or responsibility for the accuracy, completeness, or usefulness of any information, apparatus, product, or process disclosed, or represents that its use would not infringe privately owned rights. Reference herein to any specific commercial product, process, or service by trade name, trademark, manufacturer, or otherwise, does not necessarily constitute or imply its endorsement, recommendation, or favoring by the United States Government or any agency thereof. The views and opinions of authors expressed herein do not necessarily state or reflect those of the United States Government or any agency thereof.

ANALYTICAL AND EXPERIMENTAL EVALUATION OF JOINING SILICON  
CARBIDE TO SILICON CARBIDE AND SILICON NITRIDE TO SILICON NITRIDE  
FOR ADVANCED HEAT ENGINE APPLICATIONS PHASE II

Glenn J. Sundberg  
Ara M. Vartabedian  
Jon A. Wade  
Charles S. White

Date Published-October 1994

FINAL REPORT

Prepared by Norton Company  
Advanced Ceramics  
Goddard Road  
Northboro, Massachusetts 01532-1545

Funded by  
Propulsion System Materials Program  
Office of Transportation Technologies  
the Assistant Secretary for Energy Efficiency  
and Renewable Energy  
U.S. Department of Energy  
EE 51 01 00 0

Subcontract No. 86X-SB045C

for  
OAK RIDGE NATIONAL LABORATORY  
Oak Ridge, Tennessee 37831  
managed by  
MARTIN MARIETTA ENERGY SYSTEMS, INC.  
for the  
U.S. DEPARTMENT OF ENERGY  
under Contract DE-AC05-84OR21400





## TABLE OF CONTENTS

|   |   |      |
|---|---|------|
| 1 | EXECUTIVE SUMMARY . . . . .   | iii  |
| 2 | LIST OF TABLES . . . . .  | vii  |
| 3 | LIST OF FIGURES . . . . .   | viii |
| 4 | ABSTRACT . . . . .  | 1    |
| 5 | INTRODUCTION . . . . .  | 1    |
| 6 | PROGRAM OBJECTIVES . . . . .  | 3    |
| 7 | MECHANICAL EVALUATION PROCEDURE . . . . .   | 5    |
|   | 7.1 TENSILE CREEP . . . . .   | 5    |
|   | 7.1.1 Specimen Preparation . . . . .  | 5    |
|   | 7.1.2 Load Application . . . . .  | 5    |
|   | 7.1.3 Temperature Profile . . . . .   | 5    |
|   | 7.1.4 Extensometry . . . . .  | 5    |
|   | 7.1.5 Data Acquisition . . . . .  | 10   |
|   | 7.2 GREEN SHEAR STRENGTH . . . . .  | 10   |
|   | 7.3 FIRED SHEAR STRENGTH . . . . .  | 10   |
|   | 7.4 FLEXURE STRENGTH . . . . .  | 13   |
|   | 7.4.1 Specimen Preparation - Silicon Nitride Curved<br>Join Development . . . . .       | 13   |
|   | 7.4.2 Specimen Preparation - Final Testing of Curved<br>Silicon Nitride Joins . . . . . | 13   |
|   | 7.4.3 Specimen Preparation - SiC Butt Join<br>Development . . . . .                     | 13   |
|   | 7.4.4 Test Method . . . . .   | 13   |
|   | 7.5 SILICON NITRIDE SPIN TEST . . . . .   | 13   |
|   | 7.6 TENSILE FAST FRACTURE . . . . .   | 17   |
| 8 | JOIN DEVELOPMENT . . . . .  | 20   |
|   | 8.1 SILICON NITRIDE CURVED JOIN DEVELOPMENT (TASK 1.2) . . . . .                        | 20   |
|   | 8.1.1 Initial Join Development Trial . . . . .  | 20   |
|   | 8.1.2 Second Curved Join Development Trial . . . . .                                    | 26   |
|   | 8.2 FINAL SILICON NITRIDE CURVED JOIN MECHANICAL EVALUATION<br>(TASK 1.2) . . . . .     | 29   |
|   | 8.2.1 Room Temperature . . . . .  | 29   |
|   | 8.2.2 1370°C Fast Fracture . . . . .  | 29   |
|   | 8.2.3 Shear Testing . . . . .   | 32   |
|   | 8.3 SILICON NITRIDE SHAFT-TO-DISK JOIN (TASK 1.4) . . . . .                             | 33   |
|   | 8.3.1 Tensile Strength . . . . .  | 33   |
|   | 8.3.2 Spin Test (Task 1.4B) . . . . .   | 39   |
|   | 8.3.3 Modeling . . . . .  | 39   |
|   | 8.4 SILICON CARBIDE PLANAR BUTT JOIN DEVELOPMENT (TASK 2.1A) . . . . .                  | 42   |
|   | 8.4.1 Initial Join Development Trial . . . . .  | 42   |
|   | 8.4.2 Final Join Development Trial . . . . .  | 45   |
| 9 | SILICON NITRIDE TENSILE CREEP EVALUATION (TASK 1.1) . . . . .                           | 56   |
|   | 9.1 TENSILE CREEP RESULTS . . . . .   | 56   |
|   | 9.2 MODELING OF CREEP . . . . .   | 58   |
|   | 9.2.1 Steady State Creep Rate Model . . . . .   | 58   |
|   | 9.2.2 Failure Modeling . . . . .  | 68   |

|    |       |  |    |
|----|-------|--|----|
|    | 9.2.3 | Prediction of Creep Failure of Notched Tensile Specimens . . . . . | 68 |
|    | 9.2.4 | Internal Variable Model . . . . .                                  | 76 |
|    | 9.2.5 | Theta Projection Method . . . . .                                  | 79 |
| 10 |       | CONCLUSIONS . . . . .  | 82 |
| 11 |       | ACKNOWLEDGEMENTS . . . . .   | 85 |
| 12 |       | REFERENCES . . . . .   | 86 |

---

Research sponsored by the U.S. Department of Energy, Assistant Secretary for Energy Efficiency and Renewable Energy, Office of Transportation Technologies, as part of the Ceramic Technology Project of the Propulsion System Materials Program, under contract DE-AC05-84OR21400 with Martin Marietta Energy Systems, Inc.

## 1 EXECUTIVE SUMMARY

Joins of hot isostatically pressed (HIP'ed)  $\text{Si}_3\text{N}_4$ -4wt%  $\text{Y}_2\text{O}_3$  (NCX-5100 family) and sintered Beta-SiC (NCX-4500) developed during Phase I of the contract demonstrated attractive mechanical properties for advanced heat engine applications.<sup>1</sup> An experimental database was developed for both materials based upon limited MOR and buttonhead tensile tests. Within the limitations of this database, analytical/numerical models were developed for prediction of join life. The purpose of joining Phase II was to develop joining technologies for HIP'ed  $\text{Si}_3\text{N}_4$  with 4wt%  $\text{Y}_2\text{O}_3$  (NCX-5101) and for a siliconized SiC (NT230) for various geometries including: butt joins, curved joins and shaft to disk joins. In addition, more extensive mechanical characterization of silicon nitride joins to enhance the predictive capabilities of the analytical/numerical models for structural components in advanced heat engines was provided. Mechanical evaluation were performed by: flexure strength at 22°C and 1370°C, stress rupture at 1370°C, high temperature creep, 22°C tensile testing and spin tests.

Silicon nitride joins with excellent room temperature and high temperature (1370°C) mechanical properties were developed during Joining, Phase I using an albeit simple, planar butt join geometry. Certain heat engine components could benefit from development of curved join geometries with mechanical performance similar to the planar butt joins. Consequently, considerable effort during Joining Phase II was spent on development and testing of silicon nitride curved joins.

The selection of joining methods was guided by an objective to produce join interlayers with properties similar to the parent materials. The method for silicon nitride joining developed within this contract resulted from improvements upon the approach used during Phase I and incorporation of independent developmental efforts by Norton Advanced Ceramics (NAC) Division of Saint-Gobain/Norton Industrial Ceramics Corporation (SGNICC). The silicon nitride joining method consisted of the following steps.

NCX-5101  $\text{Si}_3\text{N}_4$ , formed by cold isostatic pressing and green machining into curved shapes, was joined in the green state prior to HIP densification. Join interlayers were made from various types of aqueous dispersions (or slips) of NCX-5101 powder, or made without slip. The aqueous slips although applied similarly, differed in method of preparation, additive content and the manner in which silicon nitride green joins were pre-conditioned.

Improved green strength was desired for silicon nitride joins to minimize the handling rejections experienced prior to hot isostatic pressing during Phase I of the contract. Curved silicon nitride joins demonstrated a 5.5-fold improvement of pre-sintered green strength compared with methods used for Phase I of the contract. The mechanical properties of the improved joining method were also measured by flexure strength tests at 22°C and 1370°C. There was no statistical difference between the 22°C and 1370°C flexure strength populations as a function of location within joined samples. The combined average 22°C flexure strength for curved silicon nitride joins was 886.3 MPa with a Weibull modulus of 16.4 as determined by 156 flexure specimens from five curved join disks. The combined average 1370°C flexure strength for curved silicon nitride joins was 516 MPa with a Weibull modulus of 16.0 as determined by 59 flexure specimens from five curved join disks. Only 1.2% of the 22°C flexure failures and 5.1% of the 1370°C flexure failures originated within the join interlayer. Shear tests of densified joins were not able to fail specimens at the join interlayer due to the high strength of joins relative to the parent material.

The demonstration of curved join quality similar to planar butt joins developed during Phase I of the contract allowed application of the joining technique to more complex shapes, such as a simulated rotor geometry. Shaft to disk joins made by the procedure developed for curved joins were ground to obtain spin test specimens. Additional joins of the shaft-to-disk configuration were used to manufacture tensile specimens to determine tensile strength of the actual spin test specimen join geometry.

Tensile strength of curved joins averaged 636 MPa with an estimated Weibull modulus of 8.2 with no failure originating from the join interlayer. The spin test specimens failed at angular velocities ranging between 17,000 and 42,530 revolutions per minute corresponding to a maximum principal stress from finite element analysis between 88.0 and 550.6 MPa. The angular velocity and stress at failure were less than predicted by the models developed within this contract due to failure origination from grinding damage. The size of surface flaws as determined by fractography were consistent with the flaw size calculated from the Griffith relationship for brittle failure of solids. This emphasizes the need for development of improved machining techniques for complex shaped structural ceramic components.

Tensile creep tests of the silicon nitride planar butt joins demonstrated behavior that was similar to the parent unjoined material. Creep was evaluated between temperature of 1250°C to 1420°C and stress between 100 and 250 MPa. Creep curves display a well defined primary creep regime with a gradual transition into secondary creep. None of the creep tests exhibited tertiary creep even though some tests were as long as 1,692 hours. A novel method of data acquisition allowed the measurement of creep strain from different positions upon the gauge length within a single creep specimen during each test. As a consequence, it was noted that the largest variations of creep strain at test termination were observed within specimens as opposed to between specimens. The percent difference of total strain at test termination between opposing halves of the parent material typically ranged from 5% to 57%. This was attributed to the inherent variable nature of creep within typical ceramic materials. Five of the 29 failures during tensile creep tests, originated within the join interlayer. Failed specimens exhibited cavitation at bi-grain junctions and wedge cracking at triple grain junctions. The creep data was incorporated into three models to develop a predictive tool that could be utilized for specimens of different geometry.

The widely accepted Norton's (or Arrhenius) equation approach was first considered to model creep behavior. Values of activation energy ( $Q$ ), stress exponent ( $n$ ) and material constant ( $A$ ) were determined for the creep experiments using an iterative procedure. This was done to determine a single estimate of these parameters for the entire creep matrix from which a reasonable, good correlation of predicted and actual creep strain rate was obtained.

The above model used the minimum creep rate for a given experiment since this represented the creep rate at failure or test suspension within the secondary creep regime.

A less widely accepted approach, but interesting alternative to the Arrhenius equation approach, was to model the creep behavior theta projection. The theta projection method described time dependent creep strain with a series of shape terms to reproduce the creep strain curve at a specific stress and temperature. One term of the equation represented the decaying primary component and another an accelerating tertiary component of creep strain. The theta projection method deviated from classical creep modeling by defining the secondary creep regime mathematically as the resultant contribution of the tertiary and primary

creep. Alternatively, the theta projection method provided a way to not only represent the experimental creep curves, but to interpolate to other testing conditions as well. However, some of the experimental data were not satisfactorily fit by this method. The theta projection method is limited by a dependence upon modeling tertiary creep, which was not observed experimentally. In addition, the method requires determination of sixteen coefficients, which is excessive. The highly variable behavior within the primary creep regime experienced between specimens strongly contributed to an unacceptable error for predicted creep strain values. The third model that was applied to the data involved an internal variable. This method predicts the primary creep through the evolution of a scalar internal variable. The creep strain is determined by the integration of a system of two, first order, differential equations. Validation of the approach was obtained through comparison with the actual creep behavior of nine specimens that were tested to failure.

Creep failure modeling was facilitated by a correlation of creep strain rate with time to failure which allowed application of a Monkman-Grant relationship. It was unnecessary to plot separate curves for each temperature since a good correlation of all the experimental data was obtained with a single curve.

The development of material models above was useful only if the model could predict the performance of structural components. The Norton's law was used to predict the behavior of a notched tensile specimen which served to simulate behavior of an actual component. Reasonable prediction of the time of failure for three specimens tested under different loads was an encouraging demonstration of the value of the use of a finite element code such as ANSYS in conjunction with the Norton's law model.

Attempts to join NT230 silicon carbide began with manufacture of planar butt joints. If the planar butt joint quality proved acceptable then curved joint geometries were to be undertaken. The processing steps to manufacture the NT230 material were to form green components by pressure casting and subsequently pre-sinter and siliconize. This contract attempted to join like parent billets at two different stages of processing: siliconized and pre-sintered, unsiliconized. The joining approach to be evaluated borrowed from the successful silicon nitride joining attempts whereby the join interlayers were applied as aqueous dispersions, or slips, of the parent material with other additives. The aggregate bodies joined with slip were subsequently pre-sintered and siliconized.

Initial screening trials using two types of slip interlayer for joining siliconized and unsiliconized parent materials resulted with joins of lower strength than the parent materials. Join quality was affected by pronounced silicon enrichment and porosity. Additional silicon carbide joins were made to improve quality. A total of six interlayer types consisting of various mixtures of silicon carbide and other additives were applied to join both siliconized and unsiliconized parent materials. Quality of the silicon carbide joins was evaluated by room temperature flexure strength tests of specimens ground from the joined bodies. All flexure specimens failed at the join interlayer. Join strength was lower than the strength of unjoined NT230 of similar cross sectional thickness, with respective average strengths of 152 MPa and 233 MPa. Although, the joins exhibited an improved, more homogeneous distribution of silicon carbide and silicon, all of the joins lacked a contiguous network of silicon carbide that extended into the parent material. All of the join methods resulted in join interlayers that were discrete relative to the parent materials and of higher silicon concentration. The distinct interface between the join interlayer and

parent material consisted largely of silicon within the join and silicon carbide within the parent material with an absence of interpenetration across the interface. In addition, voids within the join interlayer were strength limiting.

While the silicon nitride joins were produced with sufficient integrity for many applications, the lower join strength would limit its use in the more severe structural applications. Thus, the silicon carbide join quality was deemed unsatisfactory to advance to more complex, curved geometries. The silicon carbide joining methods covered within this contract, although not entirely successful, have emphasized the need to focus future efforts upon ways to obtain a homogeneous, well sintered parent/join interface prior to siliconization. In conclusion, the improved definition of the silicon carbide joining problem obtained by efforts during this contract have provided avenues for future work that could successfully obtain heat engine quality joins.

## 2 LIST OF TABLES

|    |   |    |
|----|---|----|
| 1  | Silicon Nitride Curved Join - Green Shear Strength at 22°C . . .                  | 25 |
| 2  | Silicon Nitride Curved Join - Flexure Strength at 22°C . . .                      | 25 |
| 3  | Silicon Nitride Curved Join - Flexure Strength at 1370°C . . .                    | 25 |
| 4  | Silicon Nitride Curved Join Development - Flexure Strength<br>at 22°C . . . . .   | 27 |
| 5  | Silicon Nitride Curved Join Development - Flexure Strength<br>at 1370°C . . . . . | 28 |
| 6  | Silicon Nitride Curved Join Development - 22°C Flexure<br>Strength . . . . .      | 29 |
| 7  | Silicon Nitride Curved Join Development - 1370°C Flexure<br>Strength . . . . .    | 32 |
| 8  | Silicon Nitride Shear Strength . . . . .  | 32 |
| 9  | Silicon Nitride Shaft-to-Disk Join - Round Gauge Tensile<br>Strength . . . . .    | 35 |
| 10 | Silicon Nitride Spin Test Results . . . . .                                       | 39 |
| 11 | Silicon Carbide Join Summary - Flexure Strength at 22°C . . .                     | 55 |
| 12 | Silicon Nitride Creep Test Summary . . . . .                                      | 57 |
| 13 | Silicon Nitride Notched Tensile Creep Summary . . . . .                           | 71 |
| 14 | Theta Projection Coefficients . . . . .   | 80 |

### 3 LIST OF FIGURES

|    |  |    |
|----|--|----|
| 1  | Tensile Creep Specimen . . . . .   | 6  |
| 2  | Contours of Maximum Principal Stress for Tensile Creep Specimen . . . . .  | 7  |
| 3  | Extensometer Flag Arrangement . . . . .  | 8  |
| 4  | Laser Extensometry Target . . . . .  | 9  |
| 5  | Creep Strain as a Function of Time . . . . .   | 11 |
| 6  | Disk on Ring Shear Fixture . . . . .   | 12 |
| 7  | Configuration of Join Sectioning for Flexure Test Specimen Preparation (Task 1.2 - Final Iteration) . . . . .        | 14 |
| 8  | Spin Test Specimen Blanks (Dimensions in Inches) . . . . .   | 15 |
| 9  | Spin Test Specimen Design (Dimensions in Inches) . . . . .   | 16 |
| 10 | High Speed Photography of Spin Test . . . . .  | 18 |
| 11 | Cylindrical Gauge Tensile Fast Fracture Specimen . . . . .   | 19 |
| 12 | Curved Join Configuration . . . . .  | 21 |
| 13 | Sectioned NCX-5101 Silicon Nitride Curved Join . . . . .   | 22 |
| 14 | Cross-Section of NCX-5101 Silicon Nitride Curved Join . . . . .  | 22 |
| 15 | NCX-5101 Silicon Nitride Curved Join Cross Section With Type "A" Slip Interlayer . . . . .                           | 23 |
| 16 | NCX-5101 Silicon Nitride Curved Join Cross Section With No Slip Interlayer . . . . .                                 | 23 |
| 17 | NCX-5101 Silicon Nitride Curved Join Cross Section With Type "B" Slip Interlayer . . . . .                           | 24 |
| 18 | Weibull Probability Plot for Room Temperature Flexure Strength Evaluation . . . . .                                  | 30 |
| 19 | Weibull Probability Plot for 1370° Flexure Strength Evaluation . . . . .   | 31 |
| 20 | Failed Joined Disk . . . . .   | 34 |
| 21 | Failure Origin of a Silicon Nitride Round Gauge Tensile Specimen #17-1 . . . . .                                     | 36 |
| 22 | Weibull Probability Plot of the Round Gauge Tensile Specimens . . . . .  | 37 |
| 23 | Failure Origin of a Silicon Nitride Spin Test Specimen #11 . . . . .   | 38 |
| 24 | Maximum Principal Stress in the Spin Test Finite Element Model for an Angular Velocity of 50,000 rpm . . . . .       | 40 |
| 25 | Probability of Failure for Joined Silicon Nitride Spin Test as a Function of Angular Velocity . . . . .              | 41 |
| 26 | Fractographs of Silicon Nitride Spin Test Specimens . . . . .  | 43 |
| 27 | Fractographs of Silicon Nitride Spin Test Specimens . . . . .  | 44 |
| 28 | Macrostructure of Join Interlayer for Join Made With Initial Unsiliconized Silicon Carbide Parent Material . . . . . | 46 |
| 29 | Microstructure of Join Interlayer for Join Made With Initial Unsiliconized Silicon Carbide Parent Material . . . . . | 47 |
| 30 | Fracture Origin Within Join Interlayer for Join Made With Initial Siliconized Silicon Carbide . . . . .              | 48 |
| 31 | Optical Micrograph of Join Interlayer B Made With Initially Siliconized Parent Material . . . . .                    | 49 |
| 32 | Optical Micrograph of Join Interlayer C Made With Initially Siliconized Parent Material . . . . .                    | 50 |
| 33 | Optical Micrograph of Join Interlayer D Made With Initially Siliconized Parent Material . . . . .                    | 51 |
| 34 | Optical Micrograph of Join Interlayer E Made With Initially Siliconized Parent Material . . . . .                    | 52 |
| 35 | Optical Micrograph of Join Interlayer F Made With Initially Siliconized Parent Material . . . . .                    | 53 |



|    |  |    |
|----|--|----|
| 36 | Optical Micrograph of Join Interlayer D Made With Initially<br>Unsiliconized Parent Material . . . . .   | 54 |
| 37 | Creep Strain as a Function of Time for Silicon Nitride Butt<br>Join #19-7 at 1392°C and 120 MPa. . . . .   | 59 |
| 38 | Creep Strain as a Function of Time for Silicon Nitride<br>Unjoined Control #46-2 at 1425°C and 100 MPa. . . . .  | 60 |
| 39 | NCX-5101 Silicon Nitride Joined Tensile Specimen After Creep<br>Testing Exhibiting Cavitation . . . . .  | 61 |
| 40 | Determination of the Activation Energy (Q) as a Function of<br>Stress . . . . .  | 62 |
| 41 | Determination of the Stress Exponent (n) as a Function of<br>Temperature . . . . .   | 64 |
| 42 | Determination of a Single Activation Energy (Q) . . . . .  | 65 |
| 43 | Determination of a Single Stress Exponent (n) . . . . .  | 66 |
| 44 | Creep Strain Rate Prediction Versus Experimental Results . . . . .   | 67 |
| 45 | Monkman-Grant Relationship for All Failures . . . . .  | 69 |
| 46 | Monkman-Grant Relationship for Join or Gauge Failures . . . . .  | 70 |
| 47 | Pinloaded, Notched Cylindrical Gauge Section Tensile Creep<br>Specimen With Extensometry Flags . . . . .   | 72 |
| 48 | Notched Cylindrical Tensile Creep Specimen Finite Element<br>Mesh . . . . .  | 73 |
| 49 | Distribution of Stress Component $\sigma_{yy}$ Under 120 MPa Reduced<br>Section Applied Stress at 1370°C . . . . .   | 74 |
| 50 | Distribution of Creep Strain $\epsilon_{yy}$ in Notched Specimen After<br>100 Hours Under 120 MPa Reduced Section Applied Stress at<br>1370°C . . . . .    | 75 |
| 51 | Failure Prediction of Cylindrical Gauge Notched Specimen<br>Using the Monkman-Grant Relationship . . . . .   | 77 |
| 52 | Comparison of Internal Variable Creep Model With Experiment<br>for NCX-5101 Joined Specimens. Solid Curve is Experiment,<br>Dashed Curve is Model. . . . . | 78 |
| 53 | Theta Projection Versus Experimental Creep Curves at 1395°C<br>and 120 MPa . . . . .   | 81 |



W.B.S. Element 1.4.2.1

ANALYTICAL AND EXPERIMENTAL EVALUATION OF JOINING  
SILICON CARBIDE TO SILICON CARBIDE  
AND SILICON NITRIDE TO SILICON NITRIDE  
FOR ADVANCED HEAT ENGINE APPLICATIONS  
PHASE II

Glenn J. Sundberg  
Ara M. Vartabedian  
Jon A. Wade  
Charles S. White

4 ABSTRACT

Techniques were developed to produce reliable silicon nitride to silicon nitride (NCX-5101) curved joins which were used to manufacture spin test specimens as a proof of concept to simulate parts such as a simple rotor. Specimens were machined from the curved joins to measure the following properties of the join interlayer: tensile strength, shear strength, 22°C flexure strength and 1370°C flexure strength. In parallel, extensive silicon nitride tensile creep evaluation of planar butt joins provided a sufficient data base to develop models with accurate predictive capability for different geometries. Analytical models applied satisfactorily to the silicon nitride joins were Norton's Law for creep strain, a modified Norton's Law internal variable model and the Monkman-Grant relationship for failure modeling. The Theta Projection method was less successful. Attempts were also made to develop planar butt joins of siliconized silicon carbide (NT230).

5 INTRODUCTION

The fabrication capabilities for silicon nitride and silicon carbide have improved since the beginning of Joining, Phase I in 1987. However, it is still difficult to fabricate reliable components of silicon nitride and silicon carbide of large size and complex geometries for heat engine applications. Two favored near net shape forming techniques, injection molding and pressure casting, suffer from limitations that become more pronounced when the thickness and complexity of the part increases. Warpage and cracking during binder removal of injection molded heat engine components still occurs. Long casting time, cracking during drying (caused by high capillary forces), density gradients and non-uniform shrinkage are limitations of pressure casting parts.

Consequently, joining of smaller sub-components of simpler geometry to manufacture a larger, complex shaped aggregate component is currently attractive. Theoretically, the reliability of components made by joining simpler shape parts can be superior to the single-part complex shape containing angles and discontinuities. Furthermore, joining is the only viable alternative when a complex component is comprised of sub-

components of dissimilar composition that are each manufactured by separate processes (e.g. reinforced CMC vanes attached to a monolithic hub in a rotor).

Joining serves as an appealing solution to current fabrication problems. Methods developed during Joining, Phase I and II have been the only effective approach available to date to obtain heat engine quality joins with good strength, acceptable creep and stress rupture life at 1370°C.

Silicon nitride joins with excellent room temperature and high temperature (1370°C) mechanical properties were developed during Joining, Phase I using an albeit simple, planar butt join interlayer. Certain heat engine components could benefit from development of curved join interlayer geometries with mechanical performance similar to the planar butt joins. Consequently, considerable effort during Joining, Phase II was spent on development and testing of silicon nitride curved joins. A final evaluation of the joining method was to demonstrate performance of simulated joined rotors by spin testing.

Concurrent, with curved join development was testing of high temperature creep behavior of planar butt joins developed during Joining, Phase I to expand the database begun during Phase I for creation of valid analytical numerical models. A number of models were evaluated to develop acceptable predictive capability for silicon nitride components of different geometries subjected to complex temperature and stress fields.

Silicon carbide joining was also investigated in an attempt to create acceptable join quality for heat engine applications.

## 6 PROGRAM OBJECTIVES

This program had the following main objectives:

- 1) silicon nitride curved join development and optimization
- 2) silicon nitride shaft-to-disk join development
- 3) silicon nitride spin testing
- 4) silicon nitride tensile creep evaluation
- 5) analytical/numerical modeling for life prediction in different conditions of temperature and stress
- 6) silicon carbide planar (flat) butt join development
- 7) silicon carbide curved join development
- 8) silicon carbide shaft-to-disk join development
- 9) silicon carbide spin testing

The program was initially divided into the main tasks, as described below.

Task 1.1      Silicon Nitride Butt Joins - Creep Resistance  
Silicon nitride butt joins shall be evaluated in the primary and secondary or steady state regions. Creep behavior shall be determined at three temperatures and three stresses. Specimens shall be evaluated after fracture by microscopy methods to determine microstructural changes during deformation.

Task 1.2      Silicon Nitride Curved Join - Join Development  
Silicon Nitride - 4wt% yttria disks shall be joined to hollow rings made from the same material. Joining shall be attempted with and without a slip interlayer. Approximately 15 joined sets shall be prepared.

Join strength shall be measured by MOR in 4 point bending at 25°C and 1370°C. One shear strength measurement at 25°C and one at 1370°C shall be attempted on the whole joined disk by supporting the outer ring and loading the inner circle until failure occurs. Optical and SEM fractography shall be performed on both MOR bars and sheared parts to identify fracture mode and origin.

Task 1.4      Silicon Nitride Shaft to Disk - Join Development  
Ten components of a shaft to disk configuration will be fabricated. The shaft/disk assembly shall be evaluated by using microfocus x-ray radiography to detect flaws in the join interface.

Task 1.4B      Silicon Nitride Shaft to Disk - Spin Test  
The database developed in Phase I and the tensile test specimens prepared in this task shall be used to model fast fracture behavior of the shaft to disk join during a spin test. Five of the components prepared in Task 1.4A shall be machined into a rotor configuration and spin tested to failure using high speed photography. Following testing, fractographic analysis shall be attempted to determine fracture mode and origin. Spin test results shall be utilized to verify the analytical model.

Task 2.1A     Siliconized Silicon Carbide Butt Joins  
 Join Development of Siliconized (dense) materials shall be joined by using slip interlayers which are subsequently sintered and siliconized. Joining shall use billets 2 X 2 X 1.5 inch. The effect of slip composition and grain size shall be evaluated. Later studies shall consist of evaluating the joining of unsiliconized bodies with slip interlayers followed by sintering and siliconization.

MOR bars shall be machined to include the joined region, then tested for join strength at 25°C and 1370°C. Results shall provide feedback to optimize slip composition and processing conditions. Control (no join) MOR bars shall also be tested. Flexural stress rupture performance at 1370°C shall be evaluated on joined materials exhibiting the best MOR performance. Optical and SEM microscopy shall be utilized to identify fracture mode and origins.

Task 2.1B     Siliconized SiC Butt Joins  
 Creep Resistance Time dependent strain deformation in siliconized silicon carbide butt joins shall be evaluated and compared to results obtained with unjoined material. Creep deformation prediction capabilities developed in Phase I and verified with silicon nitride butt joins shall be utilized.

Task 2.2       Siliconized Silicon Carbide Curved Join - Join Development  
 The approach for this effort is essentially the same as described in Task 1.2 for curved silicon nitride joins. However, the siliconized silicon carbide join may be prepared by machining green (unsiliconized) material or dense (siliconized) material depending on the results from butt joining this material (Task 2.1A). Flexural and shear strengths of the join shall be measured.

Task 2.4A     Siliconized Silicon Carbide Shaft to Disk - Join Development  
 The joining method for siliconized silicon carbide shall be as developed in Task 2.1A. The approach shall be identical to that for silicon nitride as described in Task 1.4A.

Task 2.4B     Siliconized Silicon Carbide Shaft to Disk - Spin Test  
 The model developed in Task 1.4B shall be utilized to predict failure. Five of the components in Task 2.4A shall be spin tested to failure. Fractographic analysis of failed parts shall be utilized to determine fracture mode and origin. A database consisting of 45 MOR specimens tested at room temperature shall be utilized to predict spin performance of the component. The spin test results shall be utilized to further verify the analytical model.

During Task 2.1A, Siliconized Silicon Carbide Butt Joins - Join Development, difficulties with manufacture of heat engine quality joins could not be overcome. Consequently, the dependent Tasks 2.1B, 2.2, 2.4A and 2.4B were removed from the Statement of Work.

## 7 MECHANICAL EVALUATION PROCEDURE

### 7.1 TENSILE CREEP

#### 7.1.1 Specimen Preparation

The tensile creep specimen is shown in Figure 1. It has a dogbone shape with grip end holes for pin loading. The specimen is 3.5" long, 0.100" thick and has a grip end width of 0.750". The gauge region is 1.00" long and 0.1" wide. A large radius transition region (radius = 1.0") was used to minimize stress concentration within the grip and transition regions. A detailed finite element study was conducted to optimize the specimen geometry. A requirement is that the highest creep strain rates should be confined to the gauge section. The finite element analysis suggests that the maximum stress at the pin hole is less than 0.9 of the stress magnitude in the gauge length (Figure 2), which is acceptable. There is a stress concentration at the surface where the transition region blends into the gauge length. The stress concentration at the transition is 1.03 which is typical of other tensile specimens<sup>2</sup>.

#### 7.1.2 Load Application

The typical profile included a pre-load of 20 lbs. The pre-load was maintained throughout the temperature ramp and pre-soak. After 24 hours, the load was ramped at a rate of 50 pounds per minute to 85% of the final load. The rate was then reduced to 25 pounds per minute to the final load and maintained +/- 1 pound for the duration of the test.

#### 7.1.3 Temperature Profile

The furnaces were ramped from 22°C to the temperature of creep evaluation. The furnace was heated to 1200°C at 25°C per minute, then to soak temperature at 10°C per minute, and maintained +/- 1°C to the conclusion of the test.

#### 7.1.4 Extensometry

Multiple laser extensometer targets are positioned about the join to determine the variation of strain rate within the region containing the join as compared with the two regions not containing the join (Figure 3). Two targets positioned at the extremities of the gauge section and two targets positioned adjacent to the join provide the comparative strain data.

A modified target (Figure 4) with a 45° bevel slot and the thickness decreased to 1.27 mm minimized the tendency for slipping as the gauge section elongates. Additionally, a longer moment arm increased the normal force along the line contact and improved the resistance to slipping. This change proved to be more effective than the original unslotted targets.

The actual strain is measured with laser dimensional sensors manufactured by Z-Mike Corporation.<sup>3</sup> Z-Mike model 1101 sensors were modified for hot object measurement and an increased passline extension for ten to twelve inch transmitter to object separation to accommodate the furnace. The system measurement resolution is 0.1  $\mu\text{m}$ , and the measurement precision is +/- 1  $\mu\text{m}$  at 1400°C. Both the laser transmitter and receiver are mounted on precision linear translation tables with one inch manual barrel micrometer drives.

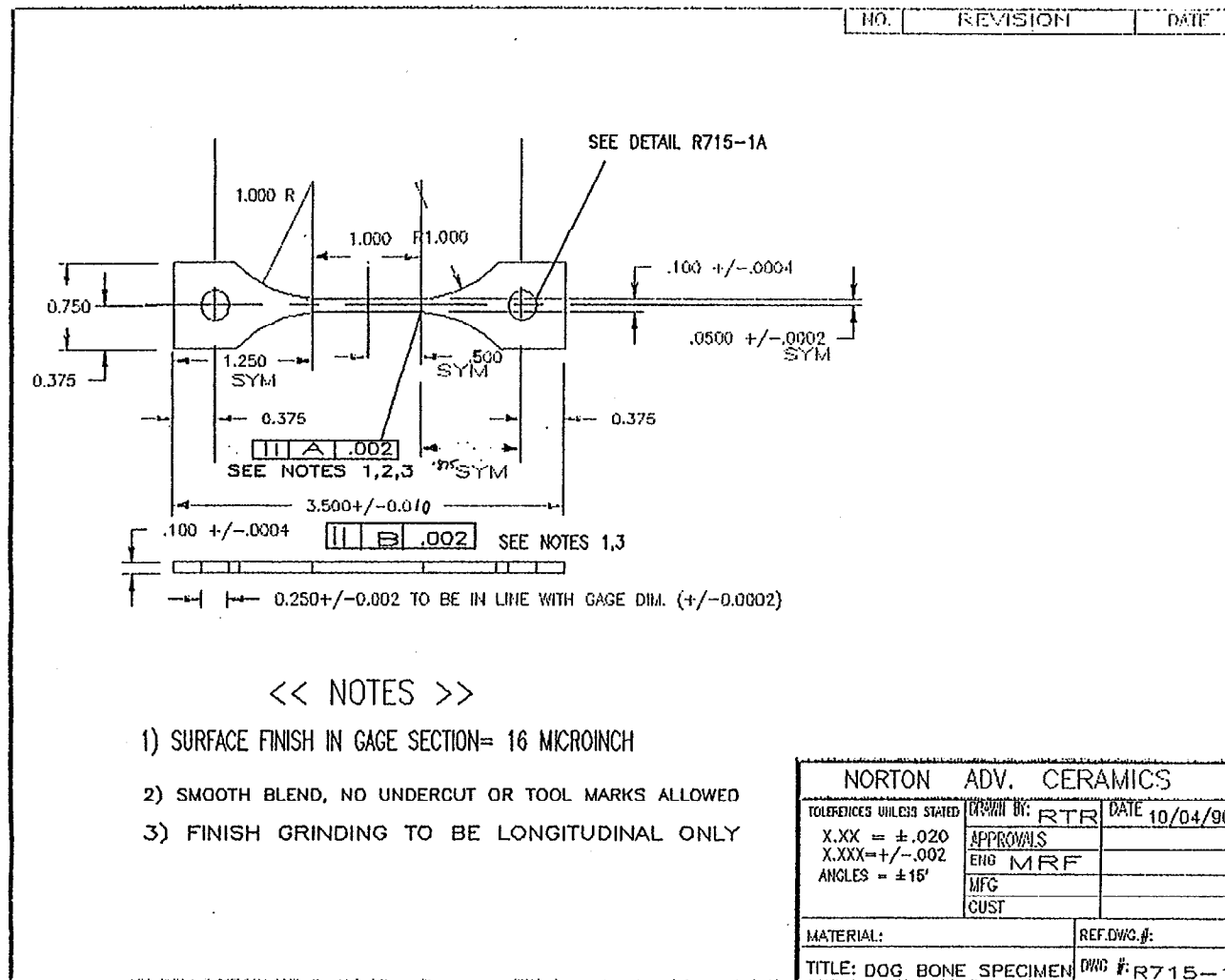


Figure 1: Tensile Creep Specimen



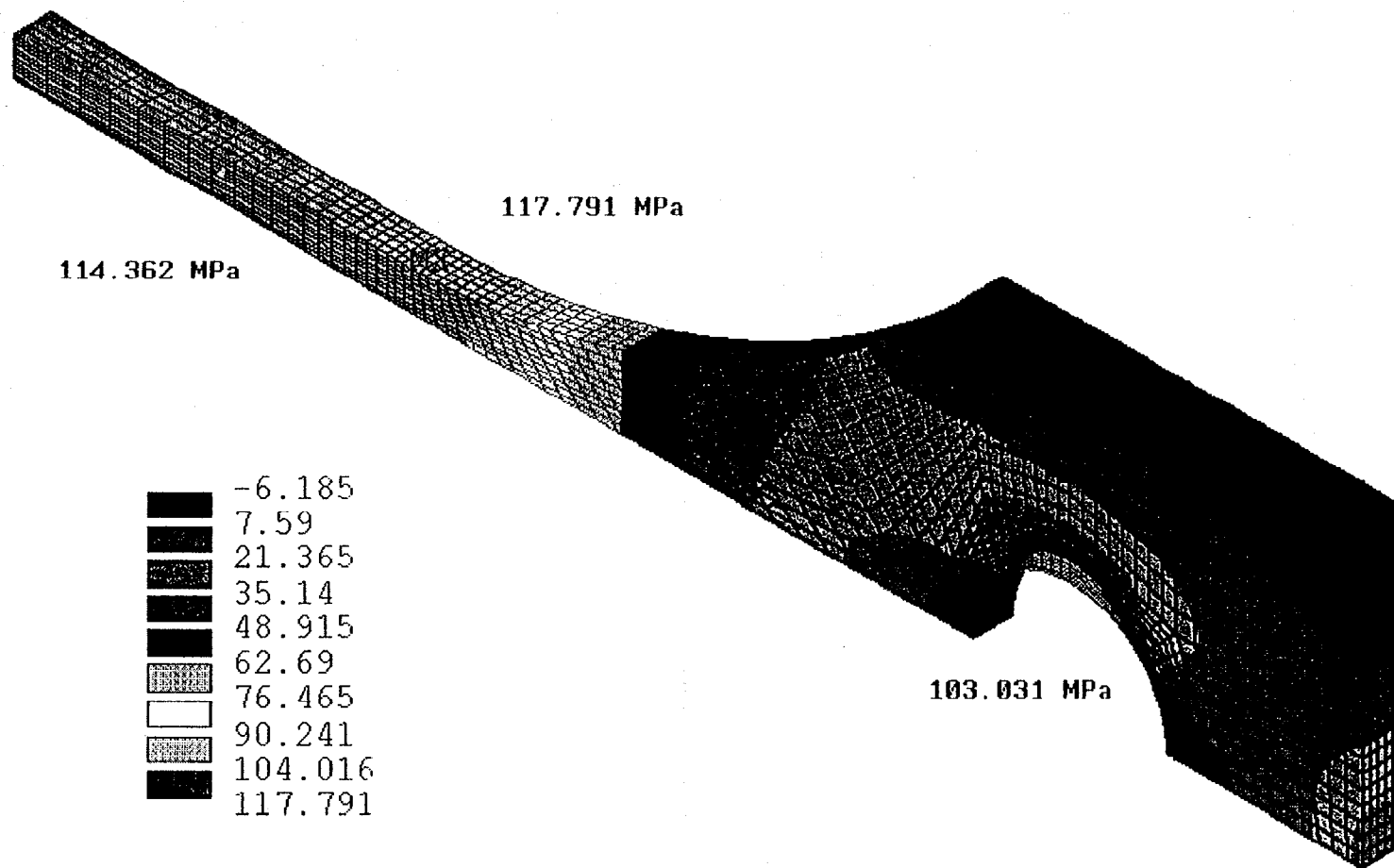


Figure 2: Contours of Maximum Principal Stress for Tensile Creep Specimen

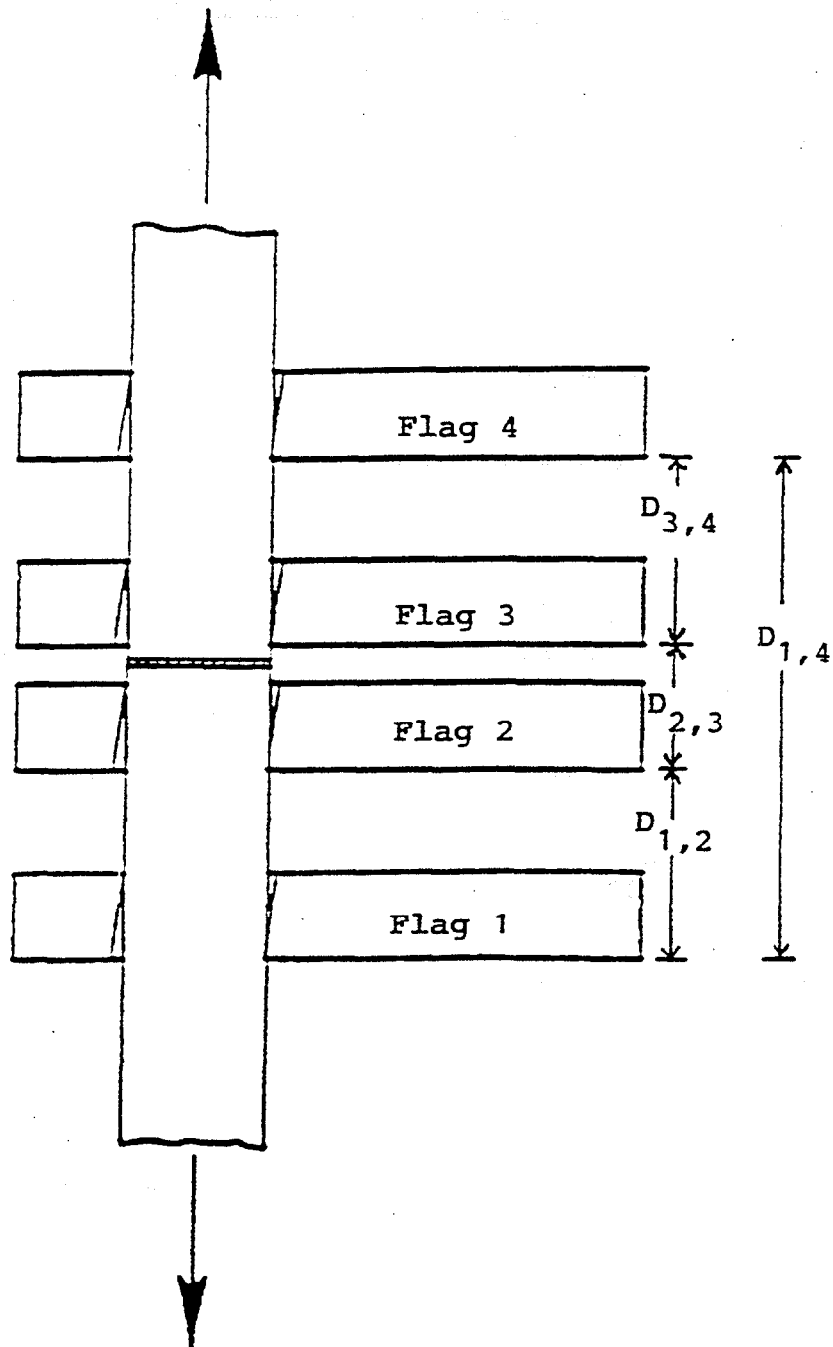


Figure 3: Extensometer Flag Arrangement

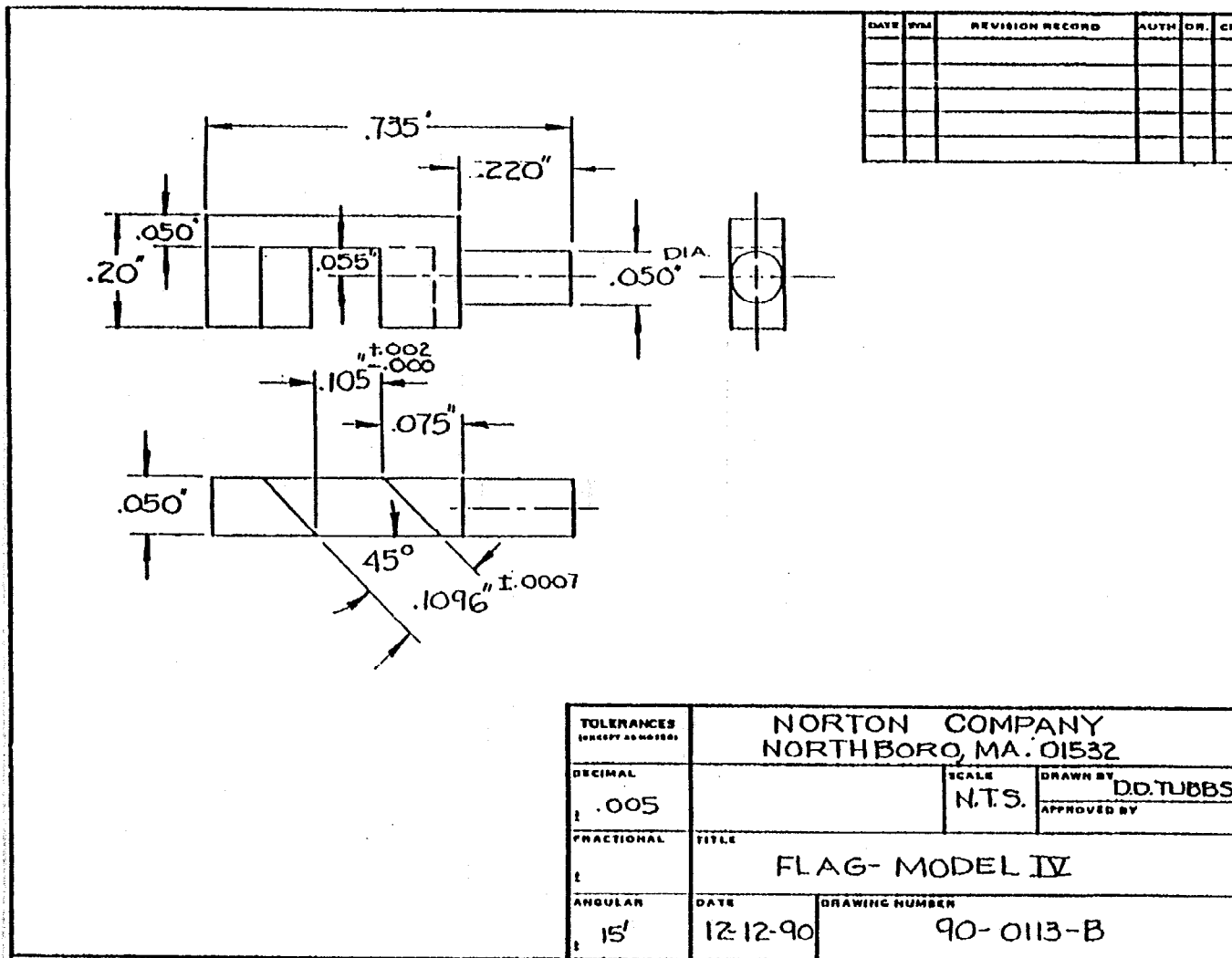


Figure 4: Laser Extensometry Target

The laser extensometry system was used to measure and store the displacement of four flags upon each tensile creep specimen (Figure 3). The relative displacement between any two flags has been used to calculate the strain of different segments of the gauge section. Creep data is reported for a specific flag couple. For example, the creep of the parent material (segments D1,2 and D3,4) and the join (segment D2,3) may be calculated independently or the combined creep of parent material and the join (segment D1,4) may be determined. In this manner, creep strain as a function of time has been plotted to compare the creep of the join interlayer and the parent material at varying temperature and applied stress.

The measurement data was conditioned and formatted in the Z-Mike-1100 processor. The system can be programmed to measure several dimensions simultaneously. Measurements were always taken between the same side of laser target pairs to allow for any uniform dimensional changes of the targets due to oxidation or other reactions at high temperature.

#### 7.1.5 Data Acquisition

The testing supervisory computer was linked to the Z-Mike-1100 processor via synchronous RS-232 communication line. The test system control program prompts the 1100 processor for the average of the 100 most recent measurements in a moving queue. The data was parsed and logged into fields with a time stamp. The load was also logged with a time stamp in a separate file or recorded on a stripchart. At the end of a test, the data is run through an RPL procedure in RS/1<sup>4</sup> to check for proper column entry and deletion of errors and empty fields. A preliminary creep strain versus time plot is generated at this time to evaluate the test run. A sample curve of the raw data (Figure 5) displays creep strain for the entire gauge section (*Strain 1-4*) and the regions above and below the join (*Strain 3-4* and *Strain 1-2*). The curve labeled *Strain Independent Laser Target* is used to record the linearity of the laser system over time. This curve should be near zero strain for the entire length of the test. The test is useful in distinguishing actual strain related phenomena from logging errors and is a good check of the system.

#### 7.2 GREEN SHEAR STRENGTH

Green shear strength tests were used to guide silicon nitride curved join development to obtain a joined, pre-sintered body with improved strength. Join shear strength was measured after a pre-sintering step, prior to hot isostatic pressing on the entire green join. A disc on ring shear fixture (Figure 6) was mounted on an Instron 4206. The load rate was 0.02 inches per minute. The shear fixture had a load/support ring diameter ratio of 0.802.

#### 7.3 FIRED SHEAR STRENGTH

The fired shear strength of curved joints were measured after completion of join development stage. Three shear test specimens were ground from each dense join by sectioning across the diameter to create three disks of 2.50 mm thickness x 70 mm diameter. This decreased the load required to fracture the dense join to a level acceptable to the testing on the Instron 4206. Five specimens were shear tested at 25°C and one at 1370°C. Two load-disc/support-ring diameter ratios were used (0.802 and 0.918) at room temperature to observe difference of failure mode.

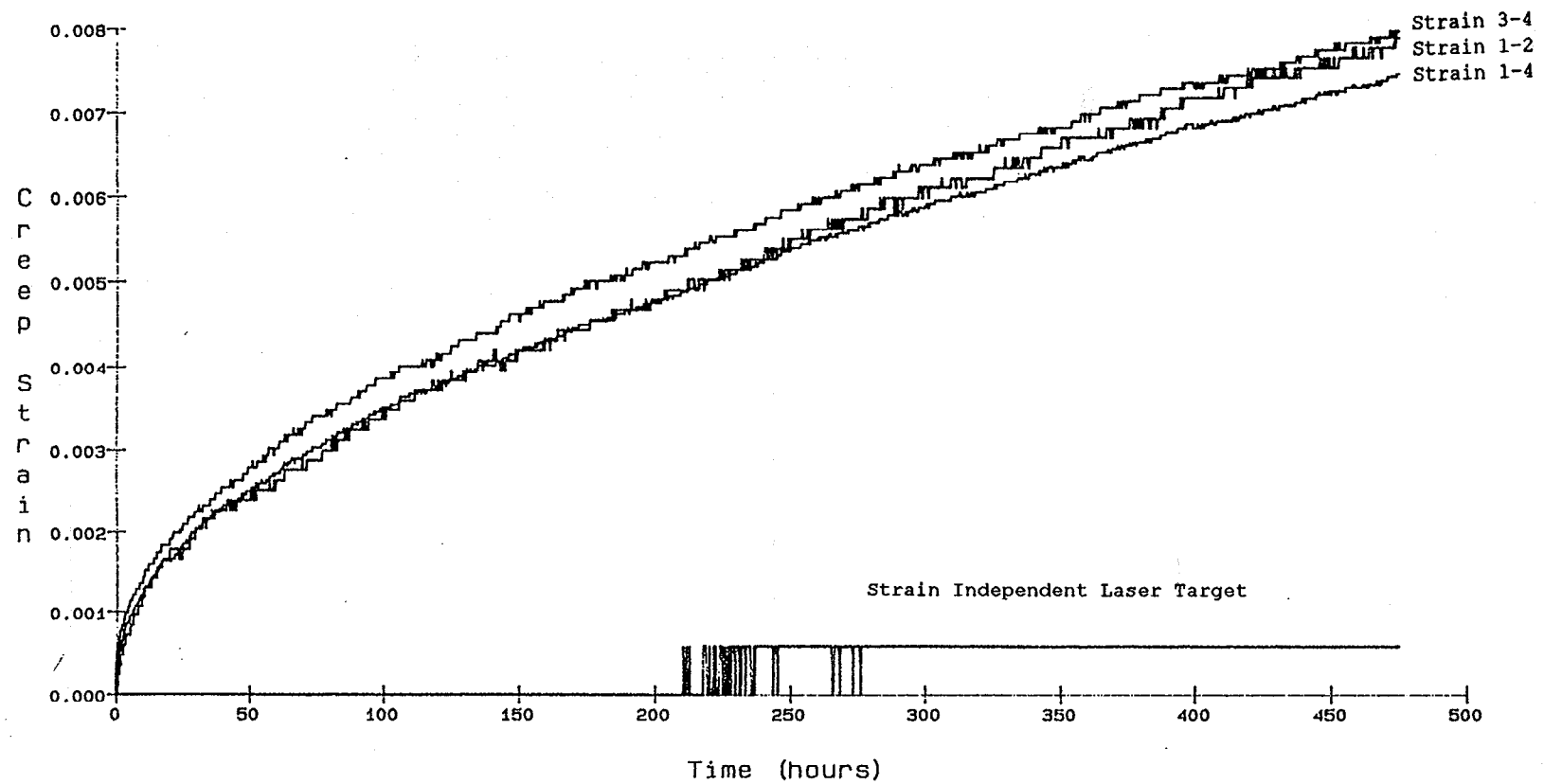


Figure 5: Creep Strain as a Function of Time

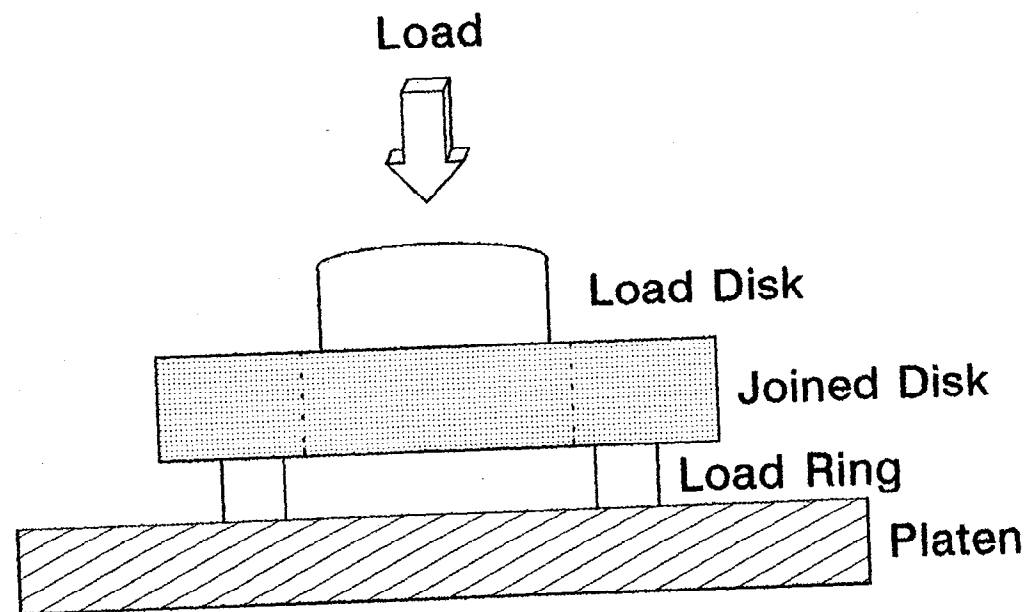


Figure 6: Disk on Ring Shear Fixture

## 7.4 FLEXURE STRENGTH

### 7.4.1 Specimen Preparation - Silicon Nitride Curved Join Development

All joins were diamond sectioned after x-ray microfocus radiography for optical inspection to determine join integrity. Additional diamond grinding yielded 12 flexure specimens per each curved join. Flexure specimens were made and tested according to the ASTM C1161-90 A geometry specifications. Deviation from the ASTM C1161-90 during tests will be explained in section 7.4.4, Flexure Strength Test Method. The join plane was located at the center of the bar, perpendicular to the longitudinal (tensile) axis of the specimen.

### 7.4.2 Specimen Preparation - Final Testing of Curved Silicon Nitride Joins

Experience with grinding flexure specimens from the curved joins allowed a greater yield of flexure specimens from each curved join. Thirty-two ASTM C1161-90 A-geometry flexure specimens were obtained from each curved join billet according to the configuration illustrated in Figure 7. Deviation from the ASTM C1161-90 during tests will be explained in section 7.4.4 Flexure Strength Test Method.

### 7.4.3 Specimen Preparation - SiC Butt Join Development

Specimens were diamond sectioned for optical inspection to determine join integrity. Additional machining yielded 15 flexure specimens per each join. Flexure specimens were made and tested according to ASTM C1161-90 B geometry specifications. Deviation from the ASTM C1161-90 during tests will be explained in section 7.4.4 Flexure Strength Test Method.

### 7.4.4 Test Method

Room temperature testing utilized a Sintech Model 1 test frame. An Instron 4206 test frame was used for high temperature tests. Flexure tests for silicon nitride curved join development used an outer span of 20 mm and an inner span of decreased size, 5 mm, on a rolling pin fixture to increase the probability of failure within the join. Flexure tests for silicon carbide join development used an outer span of 40 mm with the same inner of 5 mm. Flexure fixtures were manufactured from silicon carbide (NC-203) and complied with ASTM C1161-90 B. The fixture was mounted horizontally with the load applied normally, transmitted through a ball bearing, at room temperature. A hemispherical anvil was used at elevated temperatures to compensate for any loading eccentricity. The specimens were loaded at a cross-head speed of 0.20 mm/minute and data acquisition was handled by automated machine control. Specimen width and thickness was measured and recorded using a digital micrometer to accuracy of 0.01 mm. Peak load, break load, peak stress, and percent strain at break data were recorded and saved on computer file. Elevated temperature testing was performed in air using a CM Rapid Temp molybdisilicide furnace heated at a rate of 50°C per minute to the test temperature and equilibrated at the test temperature for 10 minutes prior to testing.

## 7.5 SILICON NITRIDE SPIN TEST

Shaft to disk joins (Figure 8) were ground to yield the four-bladed spin test specimens (Figure 9). Five additional joins of the shaft-to

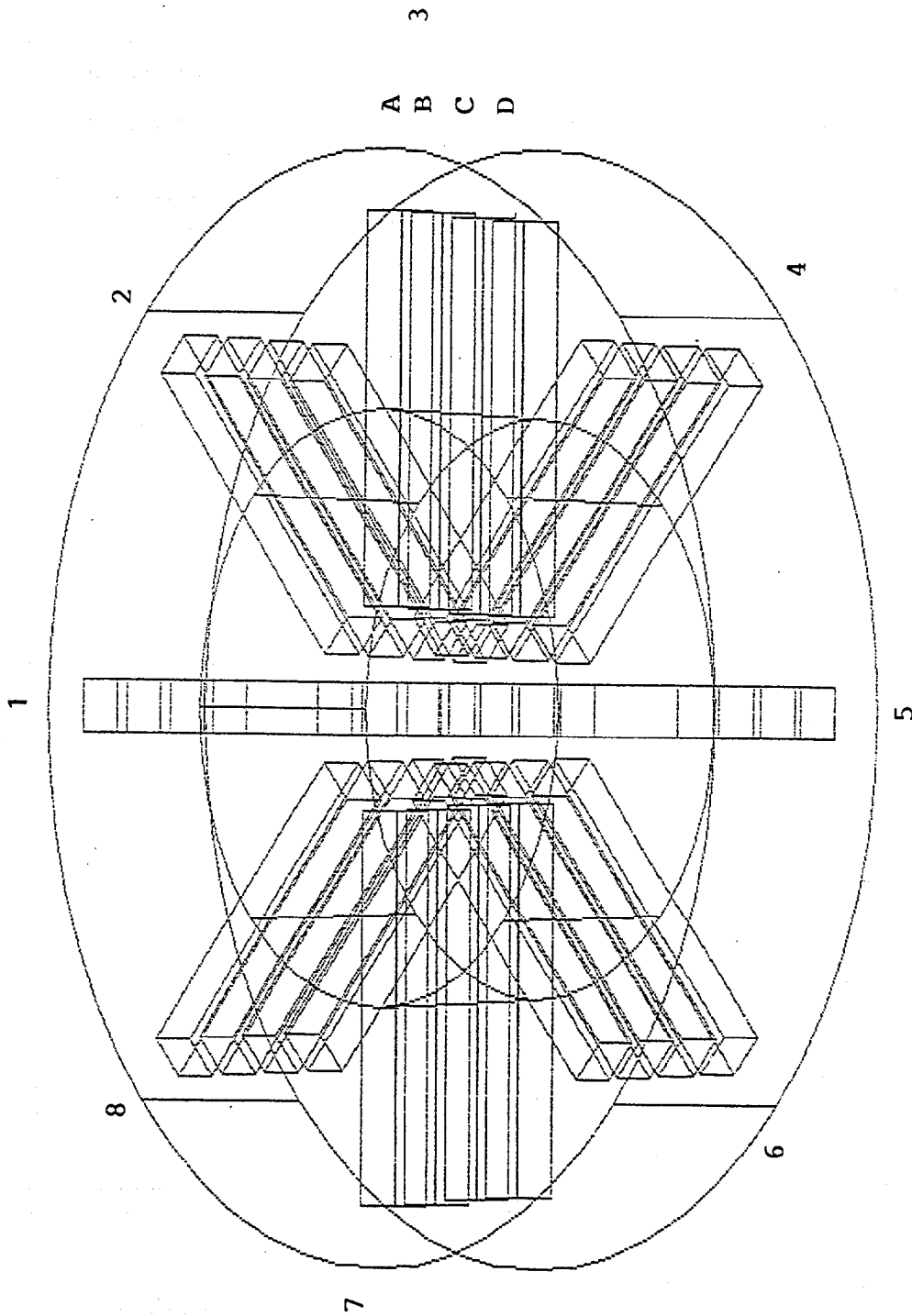


Figure 7: Configuration of Joint Sectioning for Flexure Test Specimen Preparation (Task 1.2 - Final Iteration)



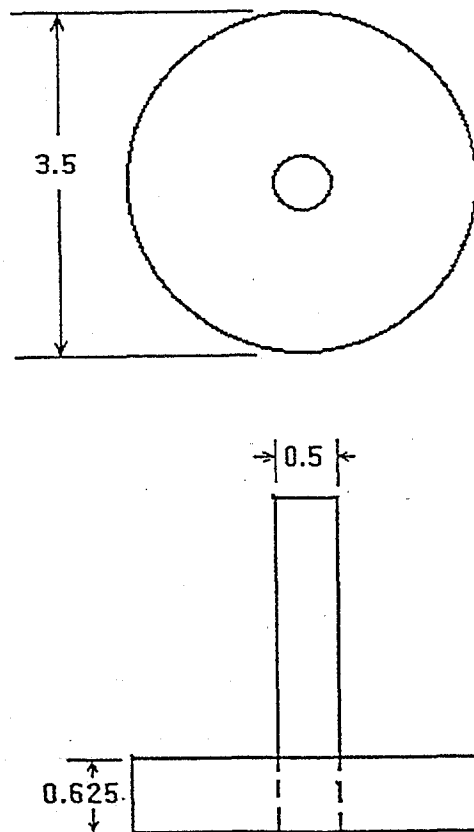


Figure 8: Spin Test Specimen Blanks (Dimensions in Inches)

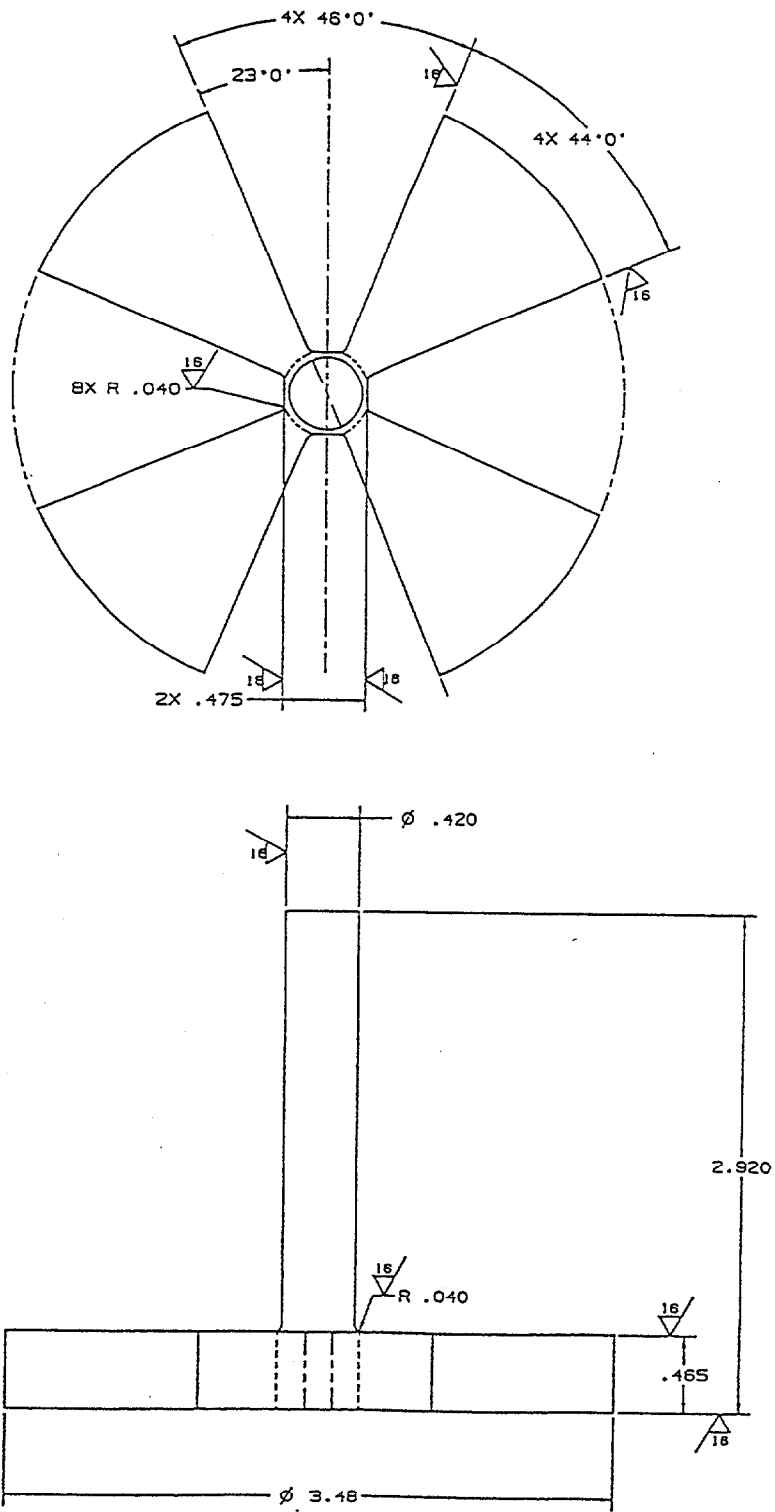


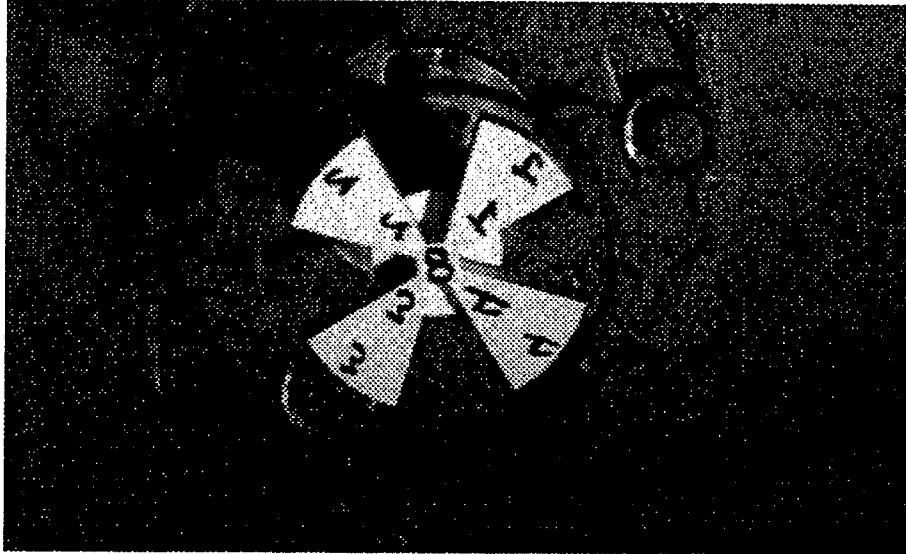
Figure 9: Spin Test Specimen Design (Dimensions in Inches)

-disk configuration were used to manufacture tensile specimens to determine tensile strength of the actual spin test specimen join geometry.

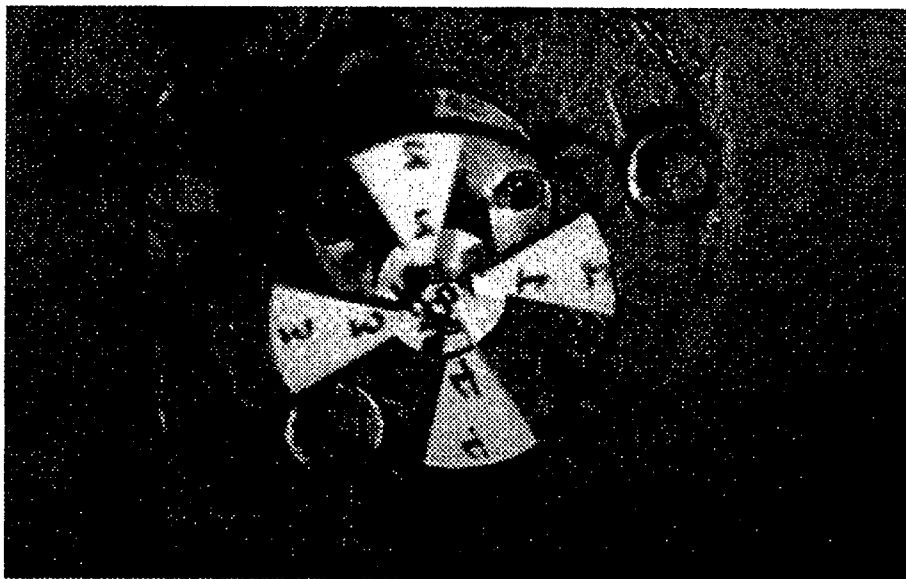
The spin specimens were tested by The Balancing Company, Vandalia, Ohio. Specimens were balanced and slowly accelerated at a rate of approximately 8.0 revolutions/sec<sup>2</sup>, to limit rotational acceleration stress effects, until a failure occurred. Failures were recorded by high speed photography (Figure 10).

#### 7.6 TENSILE FAST FRACTURE

Tensile specimens ground from shaft-to-disk joins contained two join interlayers within the gauge length and these were oriented perpendicular to the gauge length. The fast fracture tensile specimens had flat grip heads and 0.1" diameter by 1.0" in length cylindrical gauge sections (Figure 11). These specimens were tested at room temperature on an Instron Model 8562 utilizing the Instron "supergrips". In the load train the tensile specimen was attached to two stainless steel rods which were connected to the "supergrips". The specimen was attached to the rods in a pin and clevis arrangement using stainless steel dowel pins. The specimens were loaded to failure using a displacement rate of 0.100 inches per minute.



A) Prior To Failure



B) Immediately After Failure

Figure 10: High Speed Photography of Spin Test

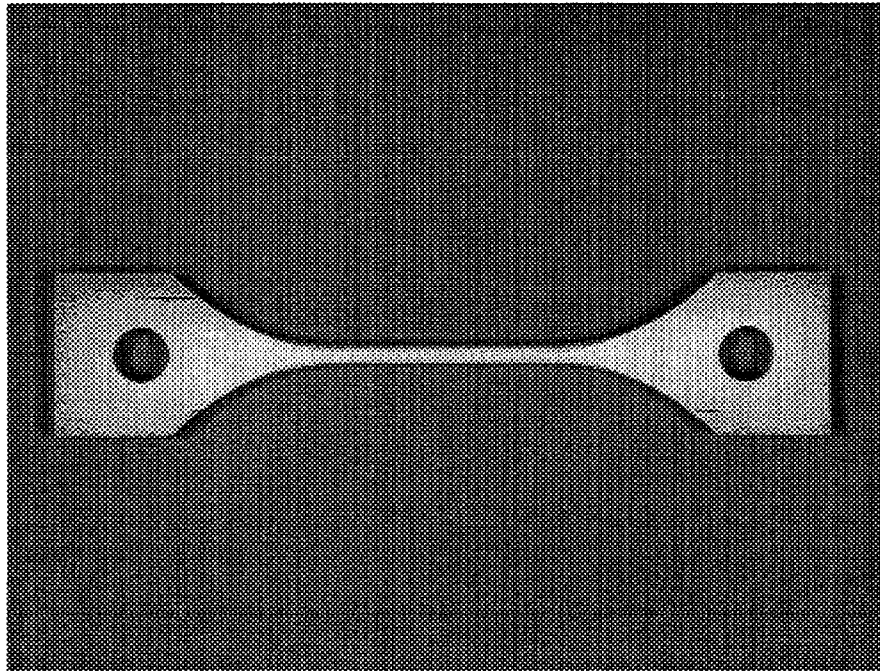


**Figure 11: Cylindrical Gauge Tensile Fast Fracture Specimen**

## 8 JOIN DEVELOPMENT

## 8.1 SILICON NITRIDE CURVED JOIN DEVELOPMENT (TASK 1.2)

Silicon nitride joins with excellent room temperature and high temperature (1370°C) mechanical properties were developed during Joining, Phase I using an, albeit simple, planar butt join geometry. Certain heat engine components could benefit from development of curved join geometries with mechanical performance similar to the planar butt joins. Consequently, considerable effort during Joining, Phase II was spent on development and testing of silicon nitride curved joins.

NCX-5101  $\text{Si}_3\text{N}_4$  was formed by cold isostatic pressing, green machined into curved shapes, joined in the green state and HIP densified to theoretical density. Join interlayers were either of various types of aqueous dispersions (or slips) made with NCX-5101 powder, or without slip. The aqueous slips although applied similarly, differ in method of preparation, additive content and the manner in which silicon nitride green joins were pre-conditioned. The resultant aggregate curved silicon nitride join after HIP densification was comprised of two joined sub-components: a disk of 83.8 mm outside diameter and 41.9 mm inside diameter into which a solid cylindrical disk was bonded. The join plane, within the resultant aggregate body, was formed at the contact of the two disks at a diameter of 41 mm (Figure 12).

8.1.1 Initial Join Development Trial

Initial curved joining trials were conducted on a small-scale with three types of join interlayers: no slip and two different aqueous slips, designated A and B. The Slip A and method of application was formerly used for the mechanical characterization and analytical modeling<sup>1</sup> tasks in Joining, Phase I and also Task 1.1 of Joining, Phase II. The aggregate join were determined to be theoretically dense after HIPing. ASTM C373-88 Microfocus x-radiography of each join showed complete densification of the join interlayer, with the exception of two areas of 1 mm x 0.5 mm dimension on the Type A join at the external surface. All joins were diamond sectioned after x-ray microfocus radiography for optical inspection to determine join integrity (Figures 13 and 14). The sectioned Slip A join and no slip join both exhibit incomplete closure of the join interlayer at the external surface of the joins (Figures 15 and 16). Sectioned surfaces of the Type B join appeared entirely dense. The Slip B join could be observed as a dark line in Figure 17 while the dense regions of the Slip A and no slip joins were not optically detected.

Mechanical Evaluation

Improved green strength was desired for silicon nitride joins to minimize handling rejections experienced prior to hot isostatic pressing during Joining, Phase I. Green shear strength tests were performed according to procedure of Section 7.2. The Type B slip join interlayer provided a significant improvement in green shear strength over no slip and Type A join interlayer (Table 1). The Type A joins and the no slip joins failed at the join interlayer. Type B joins after failure exhibited separation at the join interlayer in addition to fracture of the external and internal join disk. The origin of fracture for the Type B joins was uncertain. However, it is known that the B joins had markedly improved shear strength over the other treatments. Analysis of

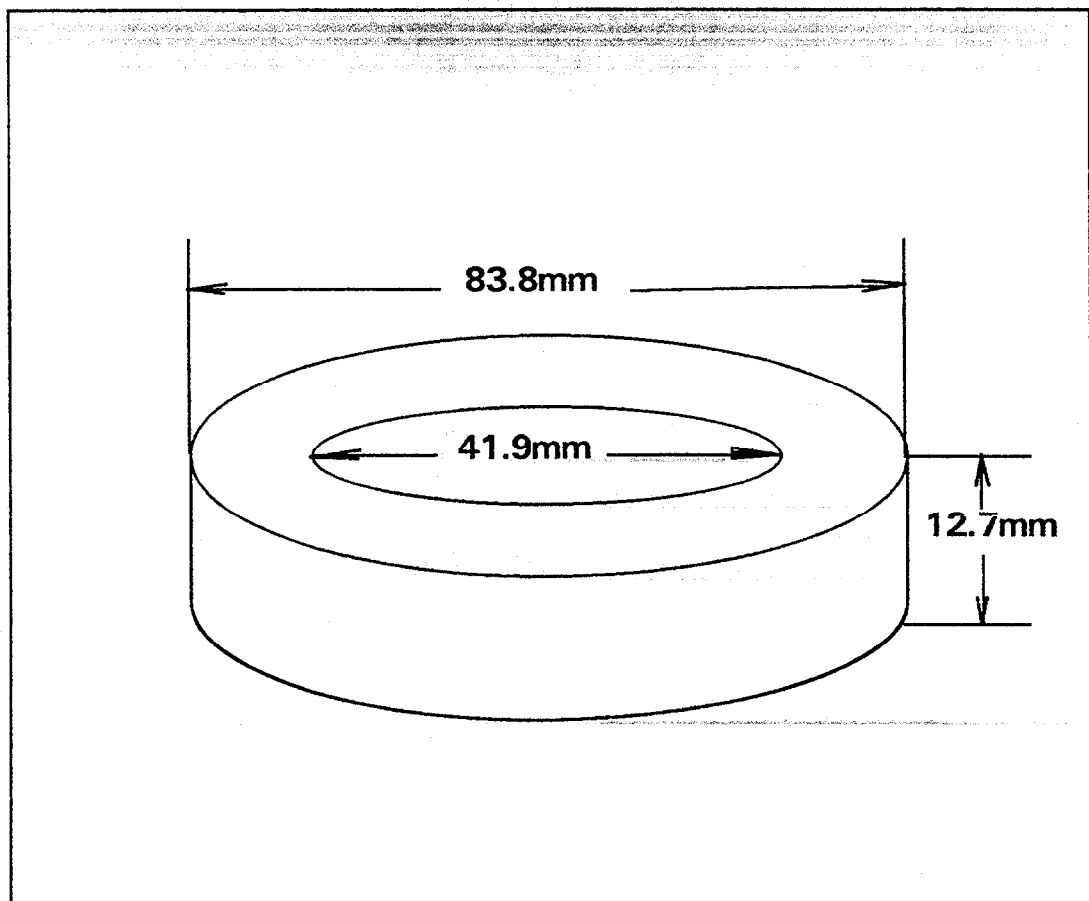


**Figure 12: Curved Join Configuration**

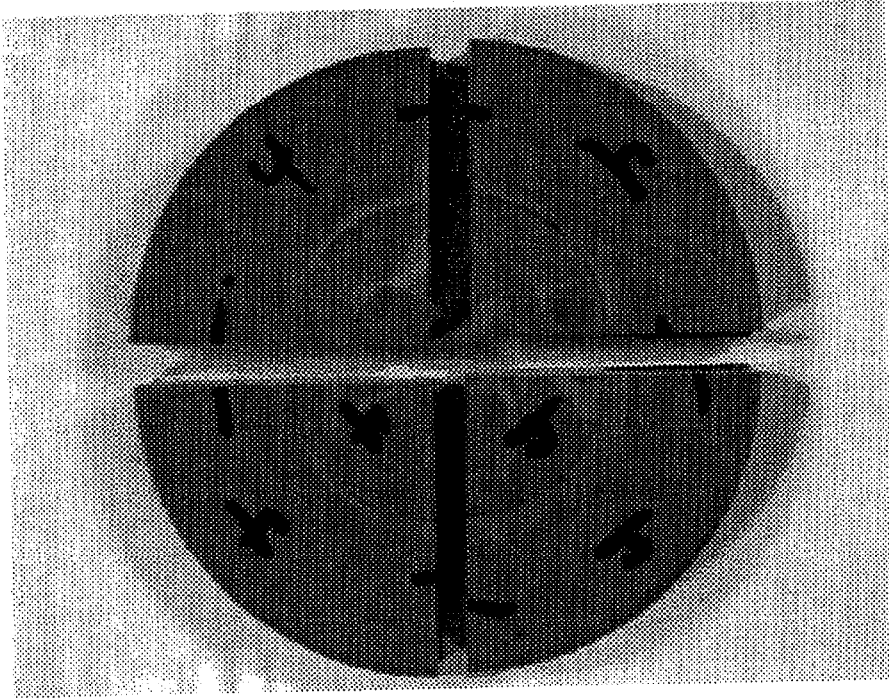


Figure 13: Sectioned NCX-5101 Silicon Nitride Curved Join

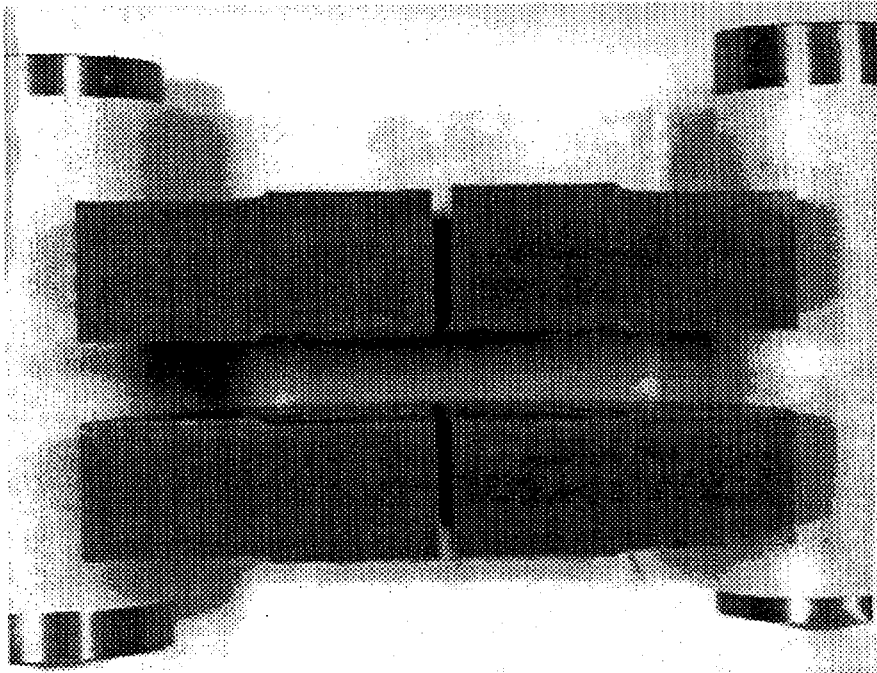
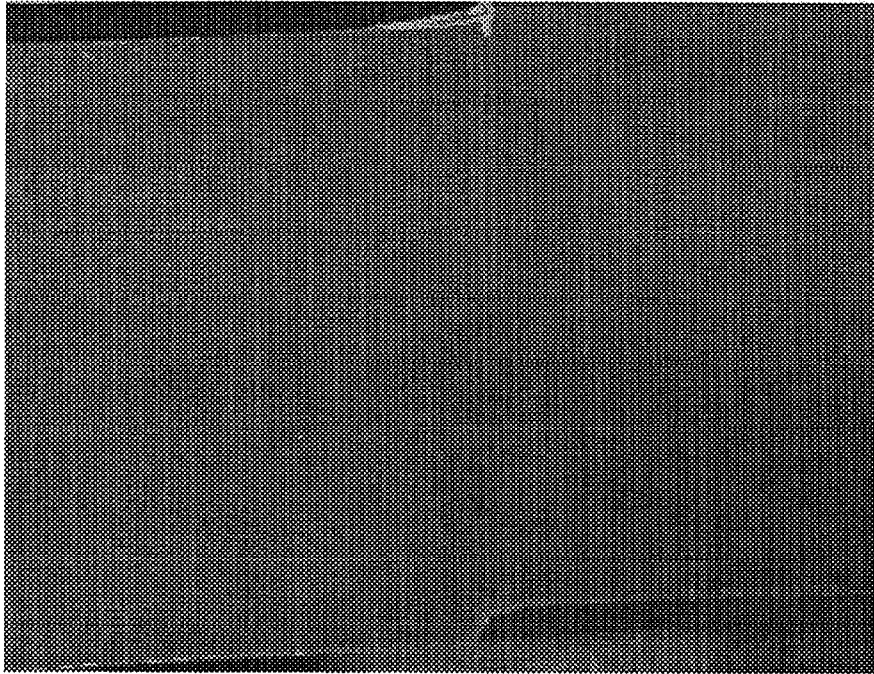
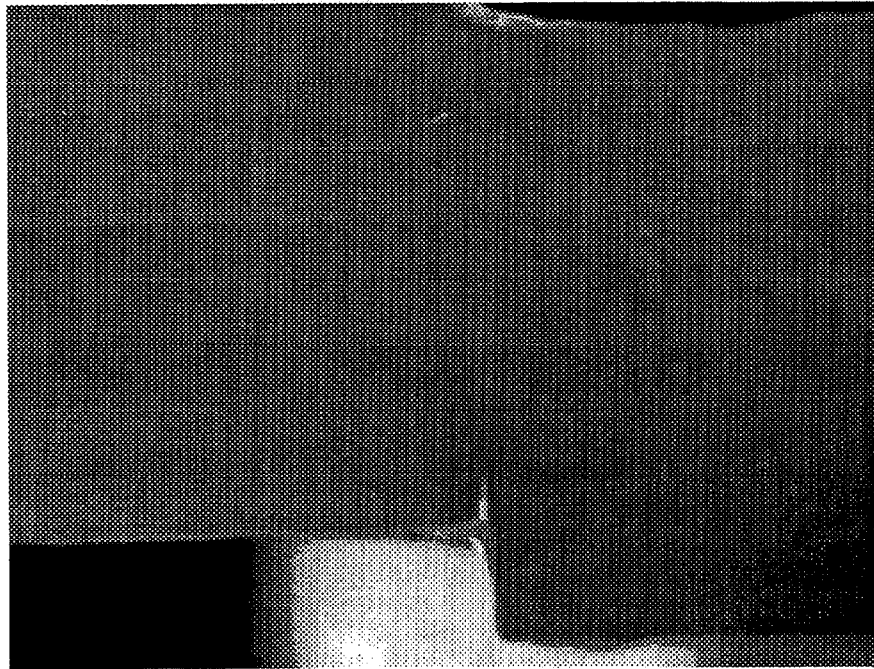


Figure 14: Cross-Section of NCX-5101 Silicon Nitride Curved Join





**Figure 15: NCX-5101 Silicon Nitride Curved Join Cross Section With Type "A" Slip Interlayer**



**Figure 16: NCX-5101 Silicon Nitride Curved Join Cross Section With No Slip Interlayer**

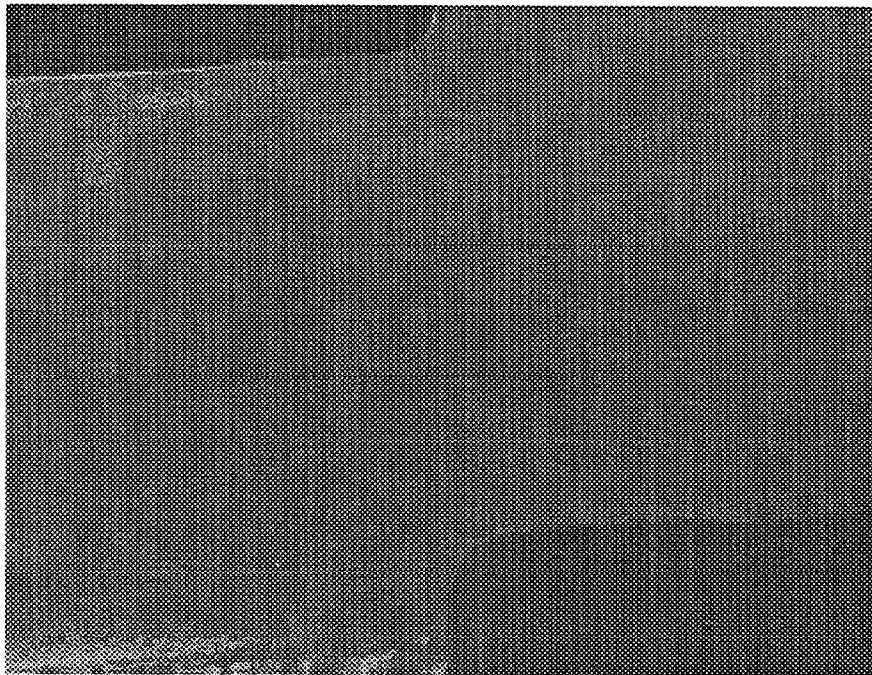


**Figure 17: NCX-5101 Silicon Nitride Curved Join Cross Section With Type "B" Slip Interlayer**

post shear tested Type A join interlayers exhibited a powdery slip residue that was easily removed. Slip residue of Type B join interlayers was firmly bonded to the parent materials.

**Table 1: Silicon Nitride Curved Join - Green Shear Strength at 22°C**

| Slip Type | Join I.D. | Mean Green Shear Strength (kPa) | Standard Deviation (MPa) | Quantity Tested |
|-----------|-----------|---------------------------------|--------------------------|-----------------|
| No Slip   | 8, 9      | 589.8                           | 121.8                    | 2               |
| A         | 5, 6      | 330.9                           | 81.3                     | 2               |
| B         | 2, 3      | 1831.3                          | 515.9                    | 2               |

The results of 22°C and 1370°C flexure strength tests of specimens ground from the curved silicon nitride joins are summarized in Tables 2 and 3. The first attempts with joining of silicon nitride curved joins were promising although the small number of flexure tests of each join type made the analysis preliminary.

**Table 2: Silicon Nitride Curved Join - Flexure Strength at 22°C**

| Slip Type | Join I.D. | Mean Flexure Strength (MPa) | Standard Deviation (MPa) | Quantity Tested | Join Interlayer Failures |
|-----------|-----------|-----------------------------|--------------------------|-----------------|--------------------------|
| B         | 1         | 771                         | 108                      | 6               | 0                        |
| A         | 4         | 832                         | 130                      | 5               | 1                        |
| No Slip   | 7         | 722                         | 132                      | 7               | 3                        |

**Table 3: Silicon Nitride Curved Join - Flexure Strength at 1370°C**

| Slip Type | Join I.D. | Mean Flexure Strength (MPa) | Standard Deviation (MPa) | Quantity Tested | Join Interlayer Failures |
|-----------|-----------|-----------------------------|--------------------------|-----------------|--------------------------|
| B         | 1         | 626                         | 28                       | 5               | 1                        |
| A         | 4         | 623                         | 28                       | 6               | 0                        |
| No Slip   | 7         | 582                         | 30                       | 4               | 1                        |

There appeared to be an insignificant statistical difference between the 22°C and 1370°C flexure strengths of each type of joining method. However, the joints manufactured without slip exhibited the lowest mean flexure strength and the highest frequency of failures within the join interlayer at 22°C and 1370°C. Join interlayers without slip were not pursued further. Additional join manufacture and testing of slip join interlayers was undertaken to obtain a conclusive analysis.

#### 8.1.2 Second Curved Join Development Trial

Encouraging results of the screening trial prompted a more rigorous application of the slip interlayer joining method using two of the slips from the screening trial (A and B) and the inclusion of two more, designated C and D. Two curved joints were made for each of four different types of slip interlayer to yield a total of 8 joints. Ground joint sections indicate that incomplete closure of the near external surface of the join interlayer (~1 mm depth) was not controlled by application of a varying amounts of slip to the external join seam. No apparent trend of incomplete closure of the near external surface of the joints with the type of slip interlayer was noted as with earlier work.<sup>6</sup> More work was required to address this limitation of the joining method.

All joints were HIP'ed to theoretical density and provided sufficient flexure strength data to statistically evaluate the mechanical properties of joints made with Types A, B and variations of these slip interlayers. Flexure strength tests of specimens machined from the dense joints were performed at 22°C and 1370°C.

#### Mechanical Evaluation

##### 22°C Flexure Strength

Mechanical evaluation of the final iteration of silicon nitride curved joint development is summarized in Table 4. While certain disk joints have visible join lines the failures do not often originate at the join. Joints 11 and 13 had the highest frequency of join failures with incomplete join interlayer closure during hot isostatic pressing as the primary cause. A statistical comparison of data sets using a non-parametric robust analysis<sup>5</sup> found no difference between most of the flexure strengths at the 95% confidence level. Joints 15 and 16, made with Slip D, showed a significantly greater room temperature strength and Weibull modulus relative to the other join types, complete join closure and an absence of failures originating in the join interlayer. The Type D slip was chosen for the remainder of silicon nitride joining on this contract.

##### 1370°C Flexure Strength

Results from 1370°C temperature fast fracture of MIL STD 1942A, Specimen A type bars for the second iteration of curved joint development are shown in Table 5. There were no statistically significant differences of 1370°C strength as a function of slip type. The joints made with Types B and D slips demonstrated an absence of failure initiation within the join interlayer at 1370°C and gave the best high temperature strength. The high temperature performance and the room temperature properties for Type D joints supported selection of Type D joints for the remainder of the contract.

**Table 4: Silicon Nitride Curved Join Development - Flexure Strength at 22°C**

| Disk Number | Interlayer Slip | Specimens Tested | Mean Strength (Mpa) | Std. Dev. (Mpa) | Min. Strength (Mpa) | Join Failures | Join Non Closure | Weibull Modulus |
|-------------|-----------------|------------------|---------------------|-----------------|---------------------|---------------|------------------|-----------------|
| 10          | A               | 11               | 765                 | 103             | 593                 | 1             | 0                | 9.5             |
| 11          | A               | 11               | 572                 | 228             | 193                 | 4             | 3                | 2.9             |
| 12          | C               | 11               | 738                 | 159             | 276                 | 0             | 0                | 6.7             |
| 13          | C               | 11               | 745                 | 214             | 262                 | 4             | 2                | 5               |
| 15          | D               | 11               | 855                 | 76              | 676                 | 0             | 0                | 14.9            |
| 16          | D               | 11               | 793                 | 55              | 710                 | 0             | 0                | 14.2            |
| 17          | B               | 11               | 793                 | 62              | 717                 | 0             | 0                | 11.7            |
| 18          | B               | 11               | 765                 | 110             | 448                 | 1             | 0                | 12.1            |

**Table 5: Silicon Nitride Curved Join Development - Flexure Strength at 1370°C**

| Disk Number | Interlayer Slip | Specimens Tested | Mean Strength (Mpa) | Std. Dev. (Mpa) | Min Strength (Mpa) | Join Failures | Weibull Modulus |
|-------------|-----------------|------------------|---------------------|-----------------|--------------------|---------------|-----------------|
| 10          | A               | 7                | 530                 | 40              | 462                | 0             | 14.6            |
| 11          | A               | 7                | 455                 | 110             | 186                | 2             | 6.4             |
| 12          | C               | 7                | 524                 | 41              | 455                | 1             | 17.5            |
| 13          | C               | 7                | 448                 | 131             | 131                | 1             | 5               |
| 15          | D               | 7                | 524                 | 48              | 462                | 0             | 12.1            |
| 16          | D               | 7                | 538                 | 35              | 469                | 0             | 16.1            |
| 17          | B               | 7                | 538                 | 41              | 462                | 0             | 13.2            |
| 18          | B               | 7                | 531                 | 28              | 503                | 0             | 19.8            |

## 8.2 FINAL SILICON NITRIDE CURVED JOIN MECHANICAL CHARACTERIZATION (TASK 1.2)

### 8.2.1 Room Temperature Fast Fracture

Results of flexure tests on a 5 mm x 20 mm span are summarized in Table 6. Data was labelled by the curved join disk number and the layer (A, B, C or D) within the disk from which specimens originated (Figure 7). A statistical comparison of the outer layers (A, D) to the inner layers (B, C) using a robust non-parametric paired analysis found no difference at the 95% confidence interval within each joined disk. A similar analysis was run for all layers of a disk with each of the other disks. The results indicated a lower strength in joins 20 and 24. The cause of the lower strength of join 24 was not apparent, although, it may be related to a slightly lower density relative to other joins. Optical fractography showed failure origins to be located primarily at the surface and in most cases near a chamfer. The Weibull modulus for all outer layers (A, D) and all inner layers (B, C) were essentially identical at 16.4 and 16.5 respectively (Figure 18). The Weibull modulus for the combined groups was 16.4. The combined average strength was 886.3 +/- 56 MPa.

**Table 6: Silicon Nitride Curved Join Development - 22°C Flexure Strength**

| Room Temperature Fast Fracture Data (Task 1.2) |       |           |               |           |          |             |         |
|--|-------|-----------|---------------|-----------|----------|-------------|---------|
| Disk   | Slice | Specimens | Mean Strength | Std. Dev. | Join     | Join        | Density |
| Number   |       | Tested    | (Mpa)         | (Mpa)     | Failures | Non Closure | gms/cc  |
| 19   | A-D   | 16        | 925.3         | 38.6      | 0        | 0           | 3.229   |
| 19   | B-C   | 16        | 914.3         | 75.2      | 0        | 0           |         |
| 20   | A-D   | 16        | 840.5         | 55.2      | 2        | 0           | 3.208   |
| 20   | B-C   | 16        | 843.2         | 42.1      | 0        | 0           |         |
| 21   | A-D   | 16        | 906.1         | 69        | 0        | 0           | 3.229   |
| 21   | B-C   | 15        | 926           | 60.7      | 0        | 0           |         |
| 23   | A-D   | 14        | 885.3         | 61.4      | 0        | 0           | 3.226   |
| 23   | B-C   | 16        | 885.3         | 51.7      | 0        | 0           |         |
| 24   | A-D   | 15        | 867.4         | 49        | 0        | 0           | 3.229   |
| 24   | B-C   | 16        | 869.4         | 64.1      | 0        | 0           |         |

### 8.2.2 1370°C Fast Fracture

There were no significant differences between join strength at 1370°C as a function of position within the join (Table 7). The average strength for all specimens tested was 516 MPa +/- 47 MPa. The Weibull modulus was 16.0 (Figure 19).

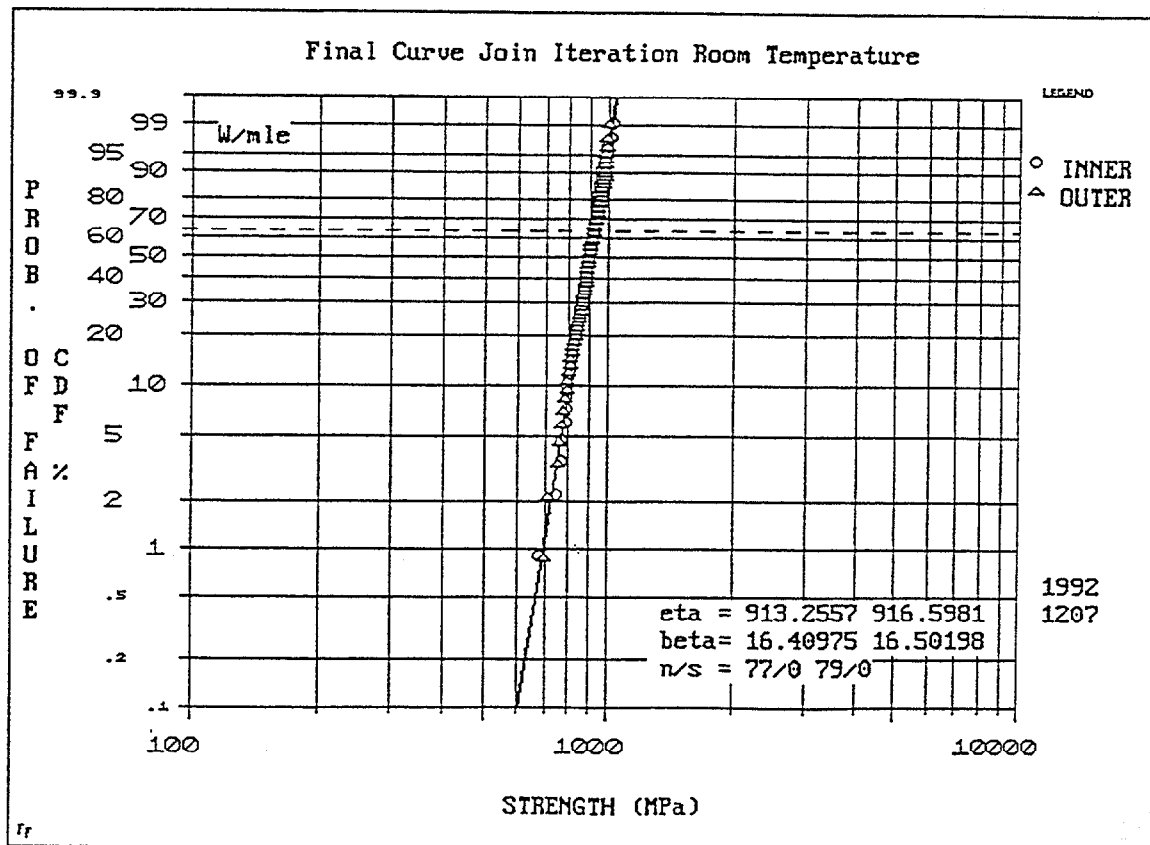
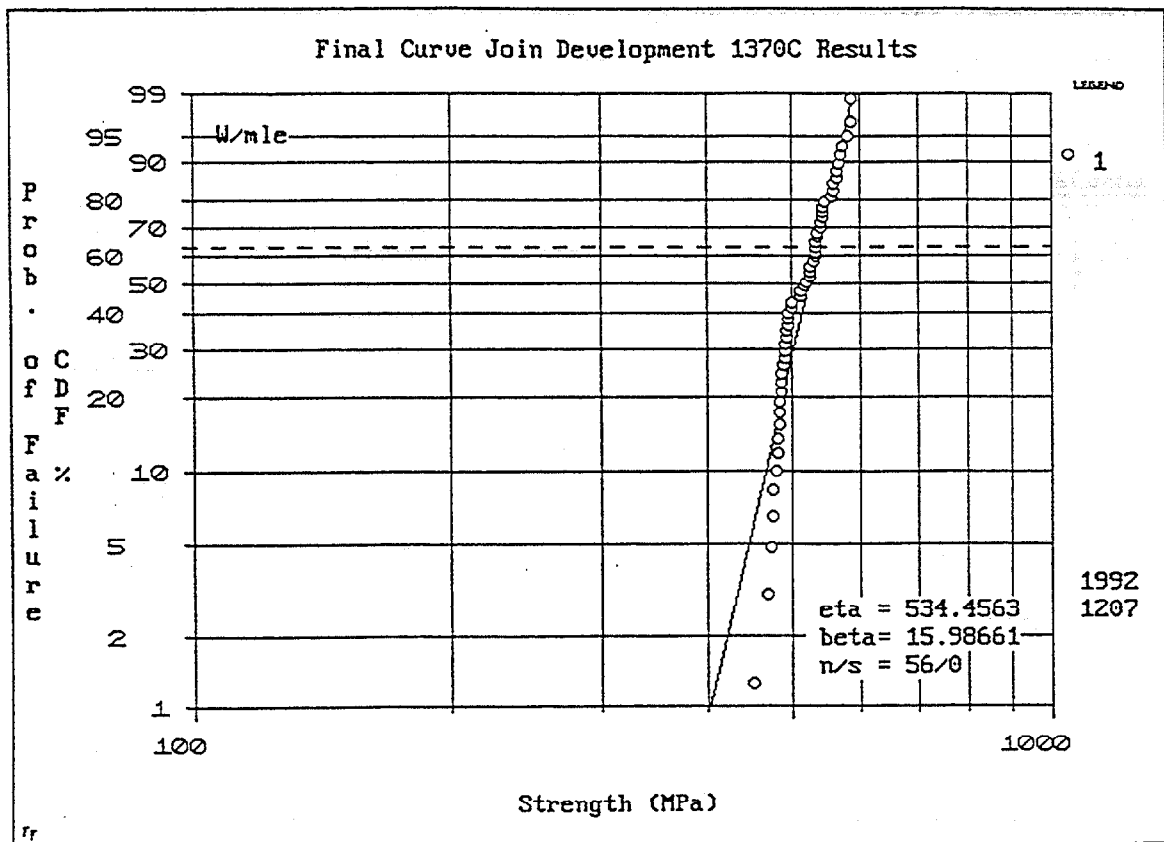


Figure 18: Weibull Probability Plot for Room Temperature Flexure Strength Evaluation





**Figure 19: Weibull Probability Plot for 1370° Flexure Strength Evaluation**

**Table 7: Silicon Nitride Curved Join Development - 1370°C Flexure Strength**

| 1370 Celsius Fast Fracture Data (Task 1.2) |            |           |               |           |          |             |         |
|--|------------|-----------|---------------|-----------|----------|-------------|---------|
| Disk                                       | Interlayer | Specimens | Mean Strength | Std. Dev. | Join     | Join        | Density |
| Number                                     |            | Tested    | (Mpa)         | (Mpa)     | Failures | Non-closure | gms/cc  |
| 26   | A,D        | 14        | 506.8         | 35        | 1        | 0           | 3.228   |
| 26   | B,C        | 16        | 490.2         | 74.5      | 2        | 1           |         |
| 28   | A,D        | 15        | 523.3         | 32.1      | 0        | 0           | 3.232   |
| 28   | B,C        | 14        | 544           | 45.5      | 0        | 0           |         |

### 8.2.3 Shear Testing

Two densified silicon nitride joined disks were sliced perpendicular to the axis to make three test specimens 2.50 mm thick by 70 mm diameter from each disk for a total of six specimens. Five specimens were shear tested at 25°C and one at 1370°C. The loading configuration is shown in Figure 6. Two different load/support ring diameter ratios were used. The results are summarized in Table 8.

**Table 8: Silicon Nitride Shear Strength**

| Sample | Temp  | R Loading Ring/<br>R Support | Load<br>(kg) | Biaxial<br>Flexural<br>Stress<br>(MPa) | Ave.<br>Shear<br>Stress<br>(MPa) | Flaw<br>Origin | Join<br>Failure |
|--------|-------|------------------------------|--------------|--|----------------------------------|----------------|-----------------|
| 1      | Room  | 0.802                        | 1684         | 407.0                                  | 55.0                             | Surface        | No              |
| 2      | Room  | 0.802                        | 1838         | 447.4                                  | 60.1                             | Surface        | No              |
| 3      | Room  | 0.802                        | 1830         | 444.8                                  | 59.8                             | Surface        | No              |
| 4      | 1370C | 0.918                        | 3240         | 329.6                                  | 105.9                            | Unknown        | Unknown         |
| 5      | Room  | 0.918                        | 2000         | 203.5                                  | 65.4                             | Surface        | No              |
| 6      | Room  | 0.918                        | 1853         | 188.5                                  | 60.6                             | Surface        | No              |

Besides the shear stress that develops in the annulus between load disk and support ring, an additional stress field of importance that develops in this test is the flexural field below the load disk. The average shear stress and maximum flexural stress are given by:

$$\tau = \frac{P}{2\pi ct} \quad (1)$$

$$\sigma = \frac{3P}{2\pi t^2} \left[ (1-\nu) \frac{a^2 - r^2}{2b^2} + (1+\nu) \ln \frac{a}{r} \right] \quad (2)$$

where

a = support radius  
 b = specimen radius  
 r = loading ring radius  
 c = join radius  
 t = specimen thickness  
 P = applied load

The flexural stress relationship was presented in reference 5.

Load/support ring ratios of 0.802 and 0.918 were used in the tests. These provide shear/flexure stress ratios of 0.14 and 0.32, respectively.

Failure origins in the fine room temperature tests were located on the bottom of the specimens, within the region of uniform biaxial flexure. None of these were associated with the join. Figure 20 shows the fracture pattern which developed in specimen 3. The failure origin for the 1370°C test was not discernable from the fragments of this specimen.

The flexural strength of the room temperature specimens ranged from 189 to 447 MPa. These specimen failed within the uniform flexure region and thus the 60 MPa level shear stress present in the specimens did not composite to these failures. The high temperature specimen failed at flexure and shear stress levels of 330 and 106 MPa, respectively. The lack of information on the failure origin in this case prevents a determination of the role of the shear stress component in this failure.

### 8.3 SILICON NITRIDE SHAFT-TO-DISK JOIN (TASK 1.4)

The demonstration of curved join quality similar to planar butt joints developed during Phase I of this contract allowed application of the joining technique to more complex shapes, such as a simulated rotor geometry. Ten curved NCX-5101 joins of a shaft-to-disk configuration were fabricated (Figure 8). Five of the densified joins were machined into four-bladed spin test specimens (Figure 9). The remaining shaft-to-disk samples were used to manufacture tensile specimens to determine tensile strength of the actual spin test specimen join geometry.

#### 8.3.1 Tensile Strength

The tensile specimens were pin-loaded with flat grip sections and cylindrical gauge section with a 0.1" diameter and 1.0" length (Figure 11). Two join interlayers oriented perpendicular to the gauge length were within the gauge of each tensile specimen. The tensile specimens are identified with two numbers: the first number denotes the shaft-to-

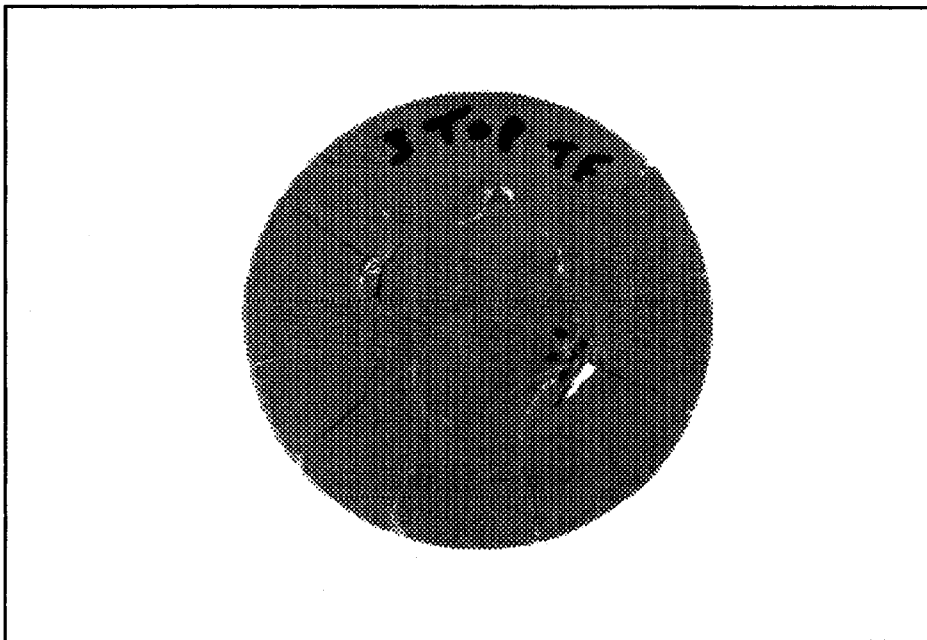


Figure 20: Failed Joined Disk

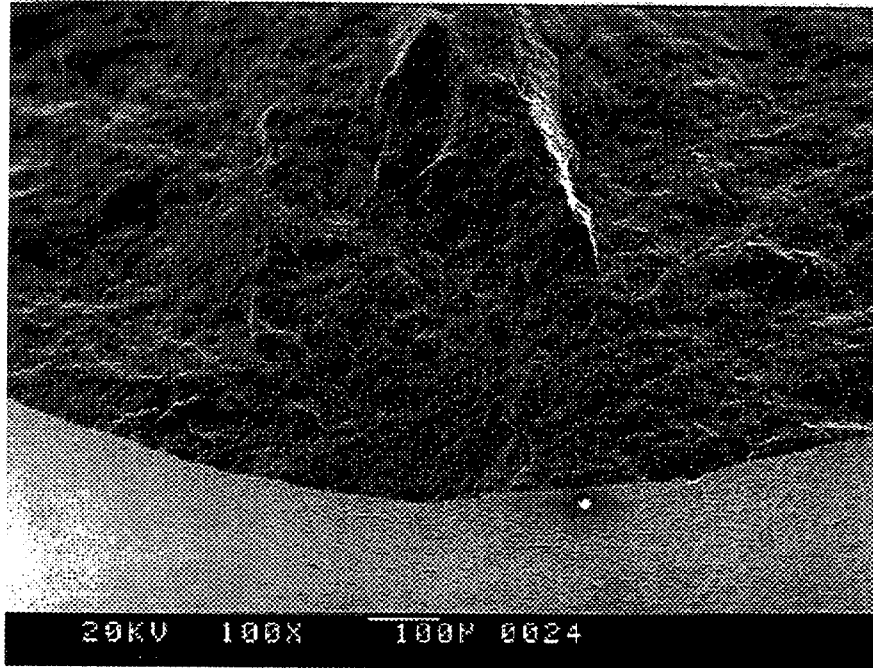
-disk join from which the specimen was machined and the second number differentiates between specimens from the same parent join (Table 9).

**Table 9: Silicon Nitride Shaft-To-Disk Join - Round Gauge Tensile Strength**

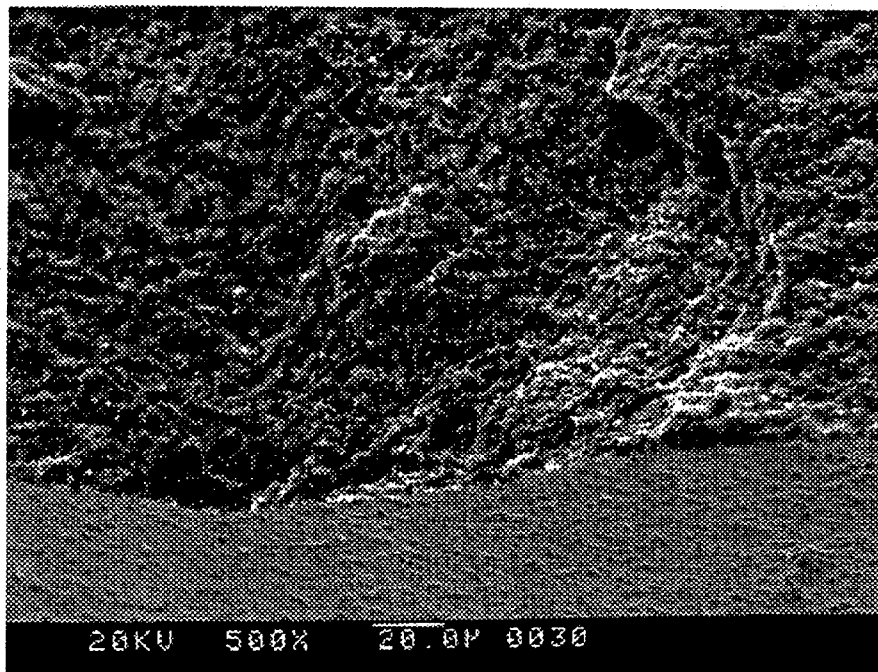
| Room Temperature Fast Fracture Data |                         |                  |
|-------------------------------------|-------------------------|------------------|
| Specimen #                          | Failure Stress<br>(MPa) | Failure Location |
| 9 #1                                | 710.25                  | gauge, non-join  |
| 9 #2                                | 660.50                  | gauge, non-join  |
| 10 #1                               | 470.99                  | gauge, non-join  |
| 10 #2                               | 491.06                  | clevis pin hole  |
| 13 #1                               | 662.53                  | gauge, non-join  |
| 17 #1                               | 491.14                  | gauge, non-join  |
| 17 #2                               | 592.39                  | gauge, non-join  |
| 19 #1                               | 359.76                  | clevis pin hole  |

Six of eight specimens tested failed from surface origins within the gauge section away from the join interfaces (Figure 21). The remaining two tensile specimens failed at the clevis-pin hole and were not considered in the strength distribution. The mean tensile strength of the six valid tests was 598 MPa. Weibull analysis of this limited data set suggests a characteristic strength of 636 MPa and a Weibull modulus ( $m$ ) of 8.2 (Figure 22).

Fractography suggests that each of the five spin specimens failed from damage induced by machining in the regions of high curvature near the shaft, but away from the join. An example of surface damage is provided in the SEM micrograph in Figure 23. The failure speeds of the spin tests ranged from 17,000 to 42,530 rpm as is discussed below:



A) 100X



B) 500X

Figure 21: Failure Origin of a Silicon Nitride Round Gauge Tensile Specimen#17-1

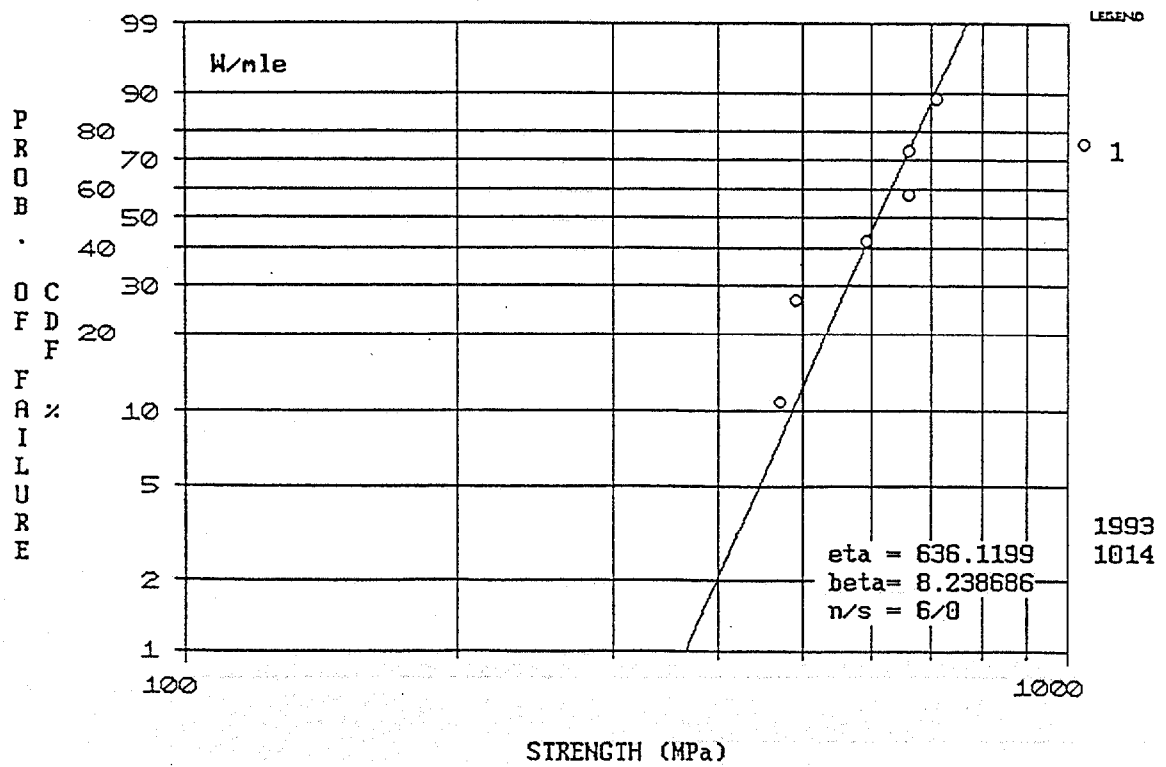
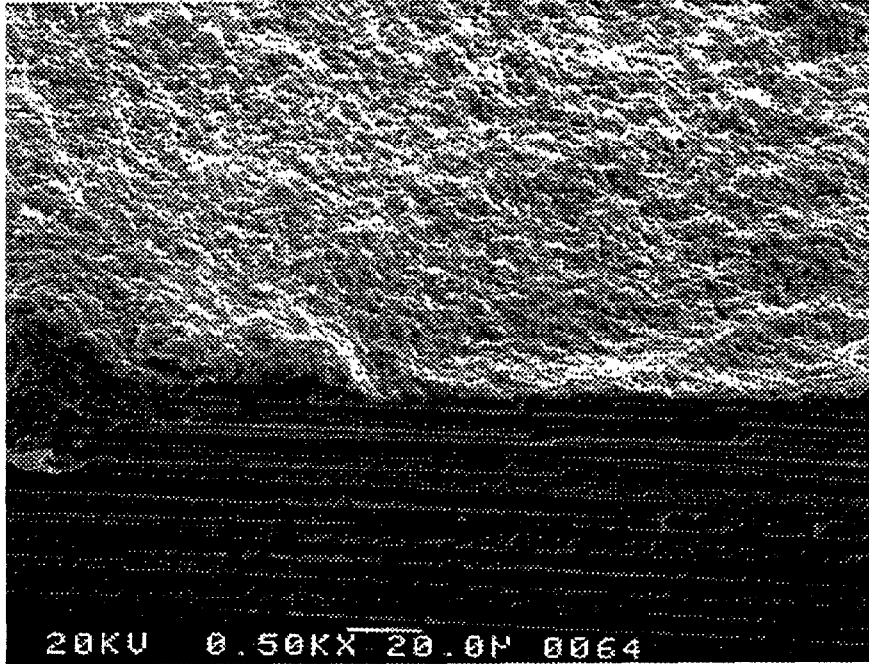
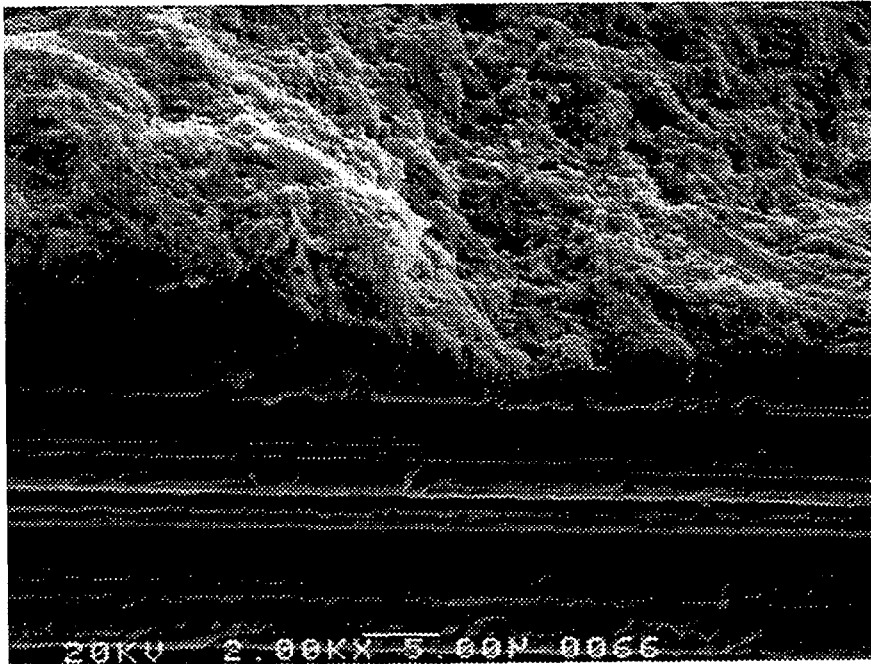


Figure 22: Weibull Probability Plot of the Round Gauge Tensile Specimens



A) 500X



B) 2000X

Figure 23: Failure Origin of a Silicon Nitride Spin Test Specimen #11



8.3.2 Spin Test (Task 1.4B)**Table 10: Silicon Nitride Spin Test Results**

| Specimen Number | Ang. Velocity at Failure (rpm) | Max Stress at Failure (MPa) | Surface Defect Size, 2a (microns) |                           |
|-----------------|--------------------------------|-----------------------------|-----------------------------------|---------------------------|
|                 |                                |                             | Fracture Mechanics (Equation 2)   | Fractographic Measurement |
| 3               | 17000                          | 88.0                        | 3941                              | -                         |
| 18              | 32030                          | 312.3                       | 313                               | 246 - 280                 |
| 11              | 36820                          | 412.7                       | 179                               | 176 - 210                 |
| 14              | 37980                          | 439.1                       | 158                               | 158 - 192                 |
| 8               | 42530                          | 550.6                       | 101                               | 88 - 122                  |

8.3.3 Modeling

The spin test specimen was analyzed using a 3D finite element model in ANSYS<sup>6</sup>. Due to symmetry only one quarter of the specimen needed to be modeled. The model consists of 8368, eight node, brick elements concentrated at the root of the blade, as well as 2444, four node, surface elements (to capture surface stress levels), for a total of 10812 elements. The loading was specified to be a constant angular velocity applied to the entire model along the axis of the rod. Contour plots of the maximum principal stress ( $\sigma_1$ ) for an angular velocity of 50,000 rpm are shown in Figure 24 overlaying the finite element grid. A principal stress value of 761 MPa develops through the thickness of the blade root a short distance (0.5 - 1.0 mm.) from the join. The join experiences stresses in the 350 to 400 MPa range at this velocity. These results may be scaled by the square of the angular velocity.

Failure origins of the spin specimens were traced to the model-predicted region of highest stress. Fractography showed that all of the test specimens failed due to surface flaws. Based on this, a reliability analysis assuming surface flaws as the critical flaw population was conducted using the CARES<sup>7</sup> reliability analysis post-processor. The Weibull parameters used in this analysis were from data on approximately 150 flexure bars which suggest a Weibull modulus ( $m$ ) of 16.4 and characteristic strength of 913 MPa. The predicted probability of failure of the spin test specimen is plotted in Figure 25 as a function of angular velocity. Plotted as circles on the graph are the actual data points from our tests. The predicted failure loads overestimate the actuals by 3,000 to 24,000 rpm.

This discrepancy is likely attributable to the difference in the machined surface quality between the spin test specimens and the flexure bars. As a result, there were larger surface defects in the spin test specimens causing them to fail at a lower load. Similar results having overestimated reliability predictions have been reported<sup>8</sup> for spin failure tests of NT154 axisymmetric, monolithic spin specimens. The discrepancy between test data and predictions were attributed to the different machining procedures used for the specimens which provided the strength database and the spin specimens.

The surface defect size can be attained in two ways. The first way

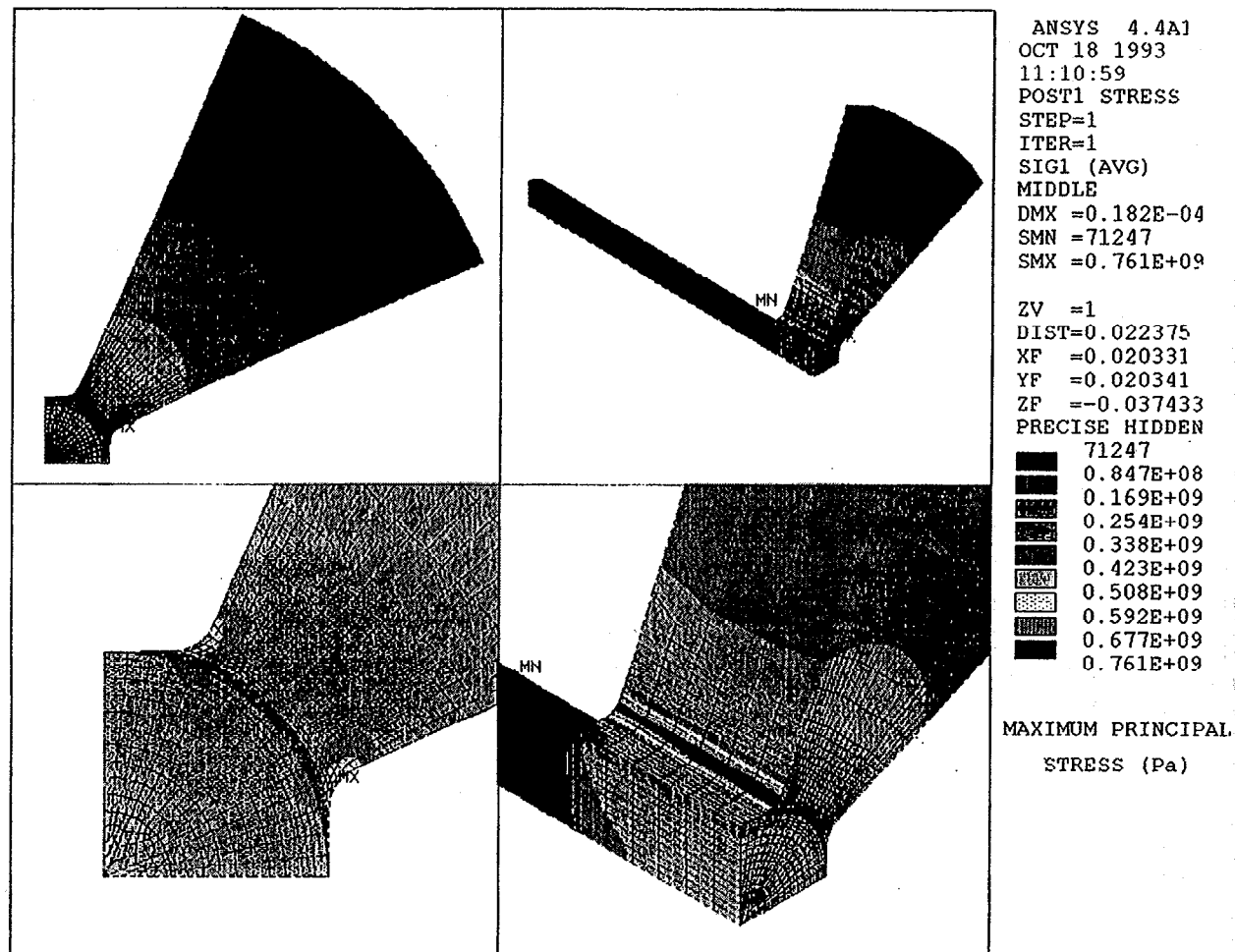


Figure 24: Maximum Principal Stress in the Spin Test Finite Element Model for an Angular Velocity of 50,000 rpm

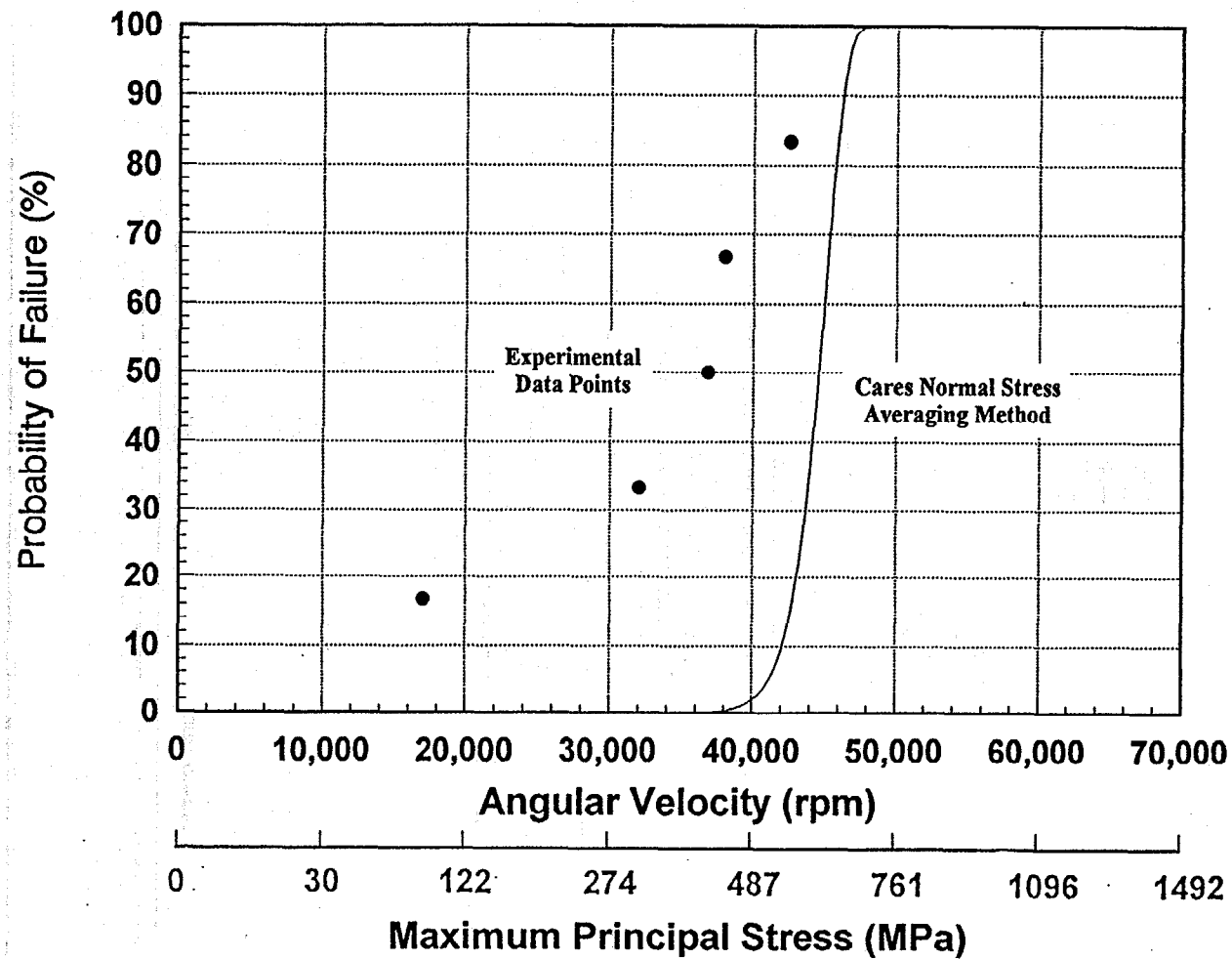


Figure 25: Probability of Failure for Joined Silicon Nitride Spin Test as a Function of Angular Velocity

was to measure the defect from fractographs. A second way was to determine the failure stress of the spin test specimens from the finite element model based on the angular velocity at failure. Using fracture mechanics, this stress can be used with the toughness of the material ( $K_{IC}=5.5 \text{ MPa}\cdot\text{m}^{1/2}$ ) to determine the flaw size. If a semi-circular surface flaw of radius,  $a$ , is assumed, the fracture mechanics relationship<sup>9</sup> that can be solved for the size parameter  $a$  is:

$$\sigma_{\text{failure}} = 0.71 \frac{K_{IC}}{\sqrt{a}} \quad (3)$$

The surface length of the defect is  $2a$  in this model.

Fractographs of four of the spin specimens are given in Figure 26 and 27. The arrows are pointing to the apparent mirror boundaries. The surface defect ( $2a$ ) is also noted.

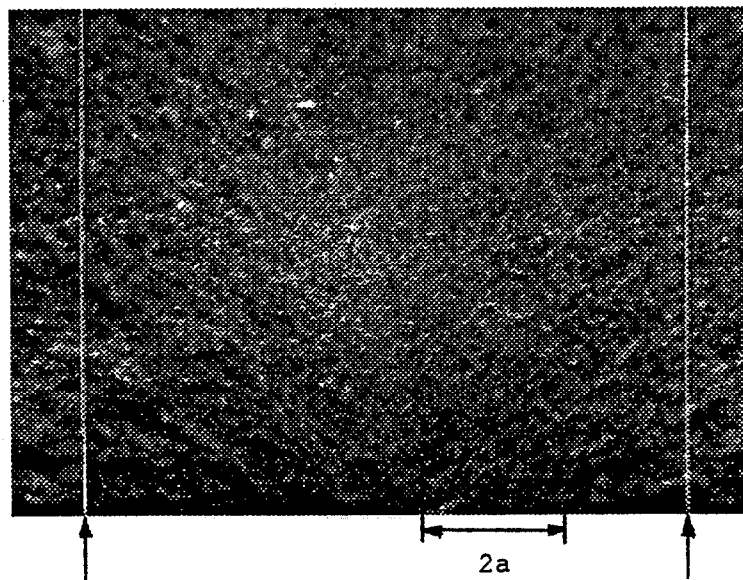
Table 10 compares the inferred fracture mechanics defect size to the measured fractographic defect measurements. Since there is an error associated with the measurement of a defect size, a range of values has been given for the fractographic measurement. The surface defect sizes ( $2a$ ) calculated from Equation 3 fall either in the range or extremely close to the measured values, except for specimen 3 which failed at an extremely low load as compared with the other specimens. It is not known why it failed at such a low load. The surface defect size needed for failure at this load is in the 3-4 mm range which suggests a major defect was present in this specimen. The agreement for the other four specimens lends credence to the view that machining damage was the failure origin in these cases. The size of the defects (diameter,  $2a = 101\text{--}313 \text{ }\mu\text{m}$ ) exceed that expected from precision grinding, such as is routinely employed for MOR bars. Hence it is concluded that the lower than predicted failure velocities was attributed to the specific grinding procedure used to prepare the bladed spin specimen.

#### 8.4 SILICON CARBIDE - PLANAR BUTT JOIN DEVELOPMENT (TASK 2.1A)

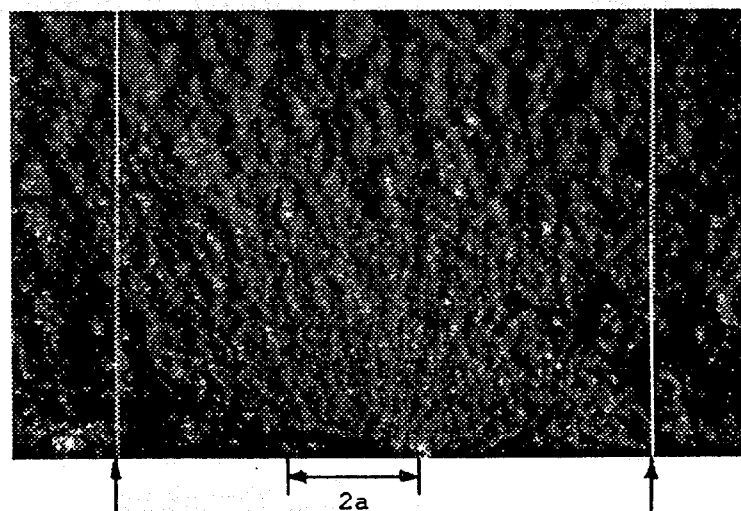
##### 8.4.1 Initial Join Development Trial

Attempts were made to join parent materials of siliconized NT230 to siliconized NT230 and pre-sintered un-siliconized NT230 to pre-sintered un-siliconized NT230. The parent materials were billets of 38 x 51 x 51 mm dimensions with the join plane of 38 x 51 mm dimension. The faces to be joined were ground flat prior to joining. Join interlayers were applied as aqueous dispersions, or slips, of silicon carbide, and other additives, and used to join NT230 silicon carbide billets. Microfocus x-radiography was used to ensure only billets without gross structural defects were to be used for the contract. After joining with slip the aggregate bodies were pre-sintered and siliconized.

Initial screening tests used the same slip interlayer, designated A, for making one join from siliconized NT230 parent materials and one join of unsiliconized NT230 parent materials. There was a silicon enrichment at the join interface with both joining approaches that resulted in a join of much lower strength than the parent materials. Joins made from the initial unsiliconized materials exhibited a join interlayer with such pronounced silicon enrichment and strength degradation that the join interlayer was incapable of withstanding stress

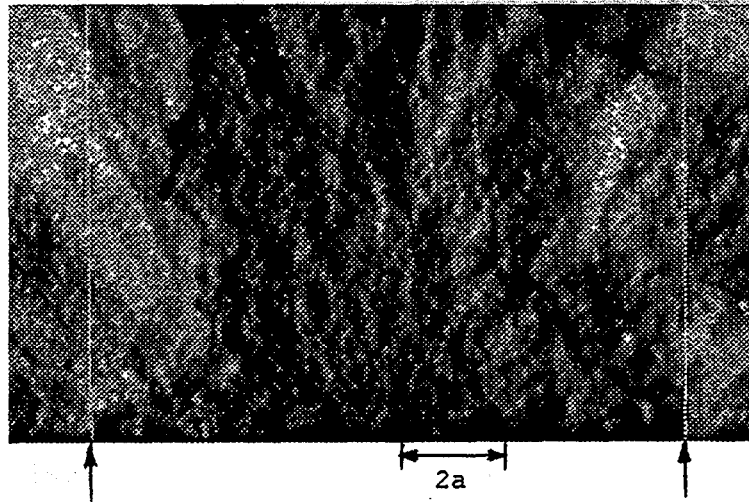


A) Specimen 18,  
Blade 4

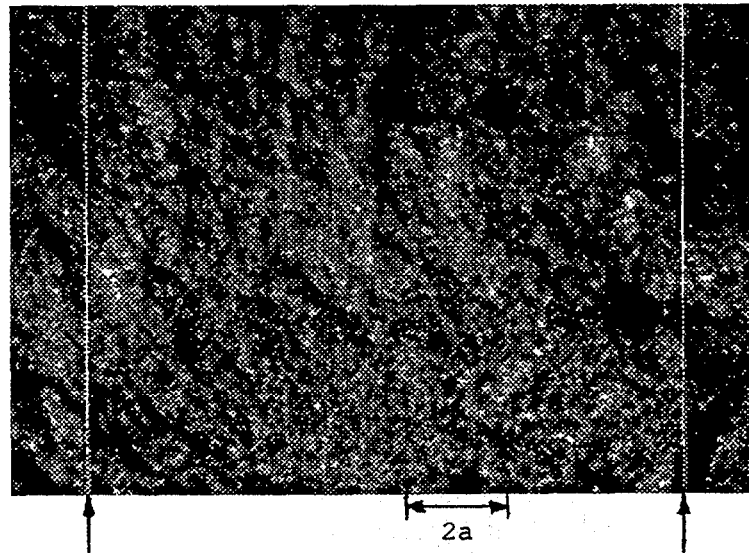


B) Specimen 11,  
Blade 2

Figure 26: Fractographs of Silicon Nitride Spin Test Specimens



A) Specimen 14,  
Blade 1



B) Specimen 8,  
Blade 2

Figure 27: Fractographs of Silicon Nitride Spin Test Specimens

of grinding causing fracture of the join interlayer. Macrostructure of the join interlayer was comprised of silicon carbide honeycomb cells predominantly filled with silicon (Figure 28). Microstructure inside of cells incompletely filled with silicon exhibited a poorly bonded silicon carbide network at the join interlayer (Figure 29).

#### Mechanical Evaluation

Mean flexure strength of the joins was 222 MPa with a standard deviation of 41 MPa as compared to a mean flexure strength of the unjoined control body of 232.9 MPa. All failures originated within the join interlayer at sites of porosity and/or silicon enrichment (Figure 30). The strength of 232.9 MPa is low for a typical NT230 body and due to inherent thickness limitations of the siliconization process. Typical average flexure strength for NT230 is 410 MPa.

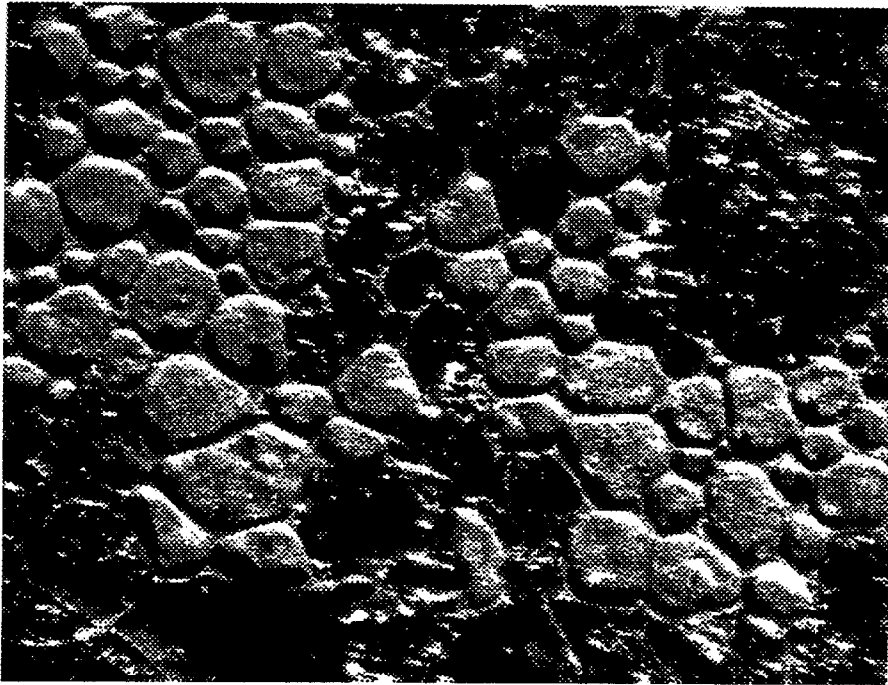
#### 8.4.2 Final Join Development Trial

Additional silicon carbide joins were made to minimize the excessive silicon enrichment and porosity at the join interlayer. Six interlayer types, designated A through F, were used for joining both siliconized and unsiliconized parent materials. Interlayer A was a replication of the earlier work which resulted in silicon enrichment and porosity of the join interlayer. Interlayers B through F were new compositions. Attempts were made to sinter and siliconize twelve joins, six with siliconized parent materials and six with unsiliconized parent materials. One join made from the siliconized parent materials and five joins of the unsiliconized parent materials separated during presinter, siliconization or grinding of the mechanical test specimens. Flexure specimens were machined from the remainder of the joins to evaluate strength.

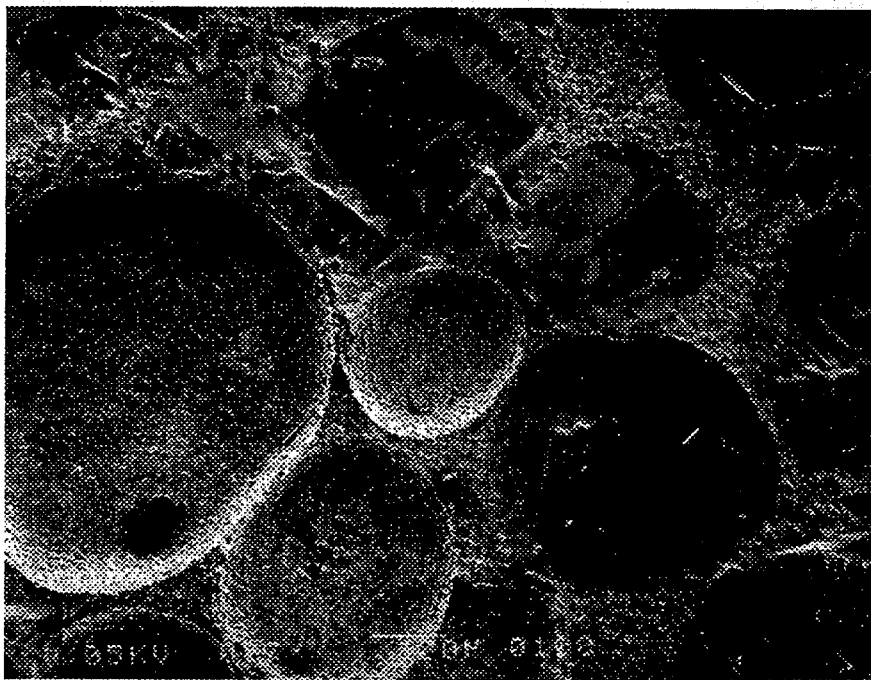
#### Mechanical Evaluation

Room temperature strengths of the joins were not improved with the different join interlayer treatments (Table 11). Failure originated predominantly within the join interlayer at regions of porosity and/or silicon enrichment. The mean join strengths ranged between 101 and 222 MPa as compared to 233 MPa for the mean strength of the unjoined NT230 silicon carbide parent material of similar cross sectional thickness. The NT230 parent material of 38 mm cross-sectional thickness demonstrated significantly lower strength than typical for NT230 of thinner cross-section (410 MPa for 10 mm thick cross-section). Characterization determined the cause of strength dependence upon cross-sectional thickness was due to inhomogeneous silicon infiltration across the join cross-section during the manufacture of the parent material.

Polished sections of the joined interlayers are exhibited in Figures 31 to 36. Joins are identified for ease of discussion by the type of parent material (siliconized=S or unsiliconized=U) and join interlayer (A through F). For example, a join S-D was made with the initially siliconized parent materials and joined with interlayer D. The appearance of the joins vary widely, with S-B exhibiting the most



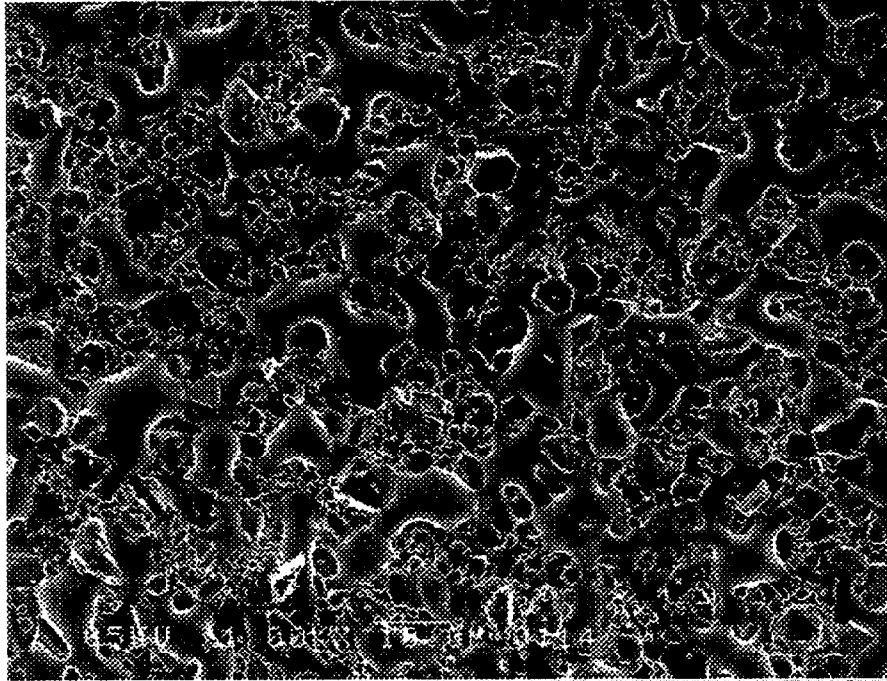
A) 12X



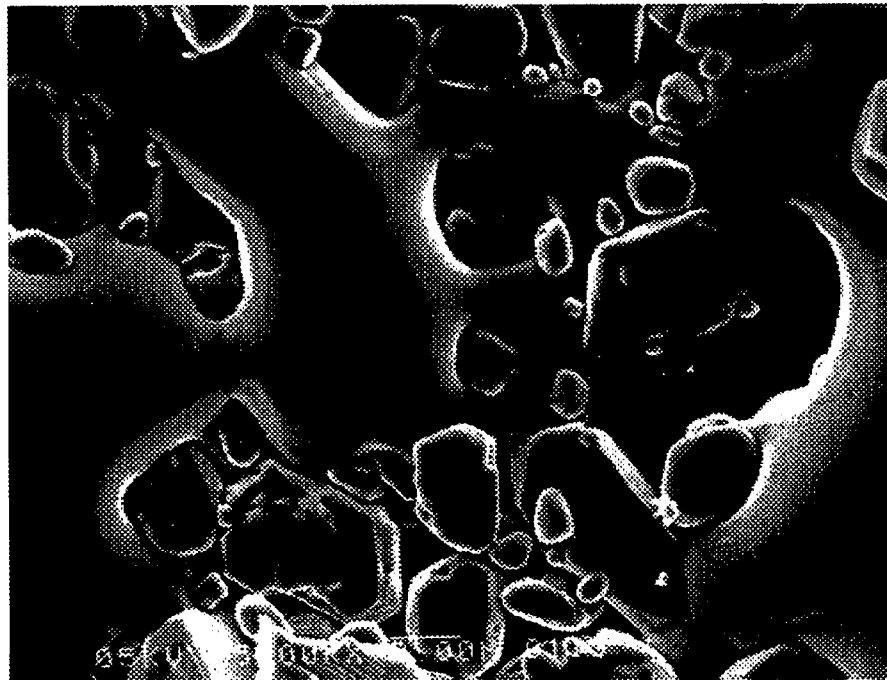
B) 77X

**Figure 28: Macrostructure of Join Interlayer for Join Made With Initial Unsiliconized Silicon Carbide Parent Material**



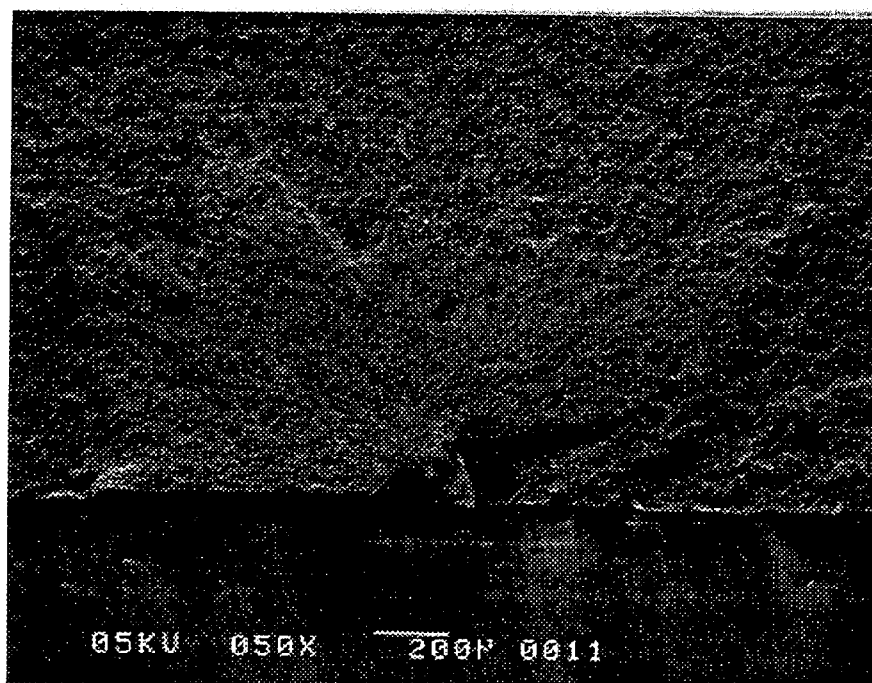


A) 1,000X

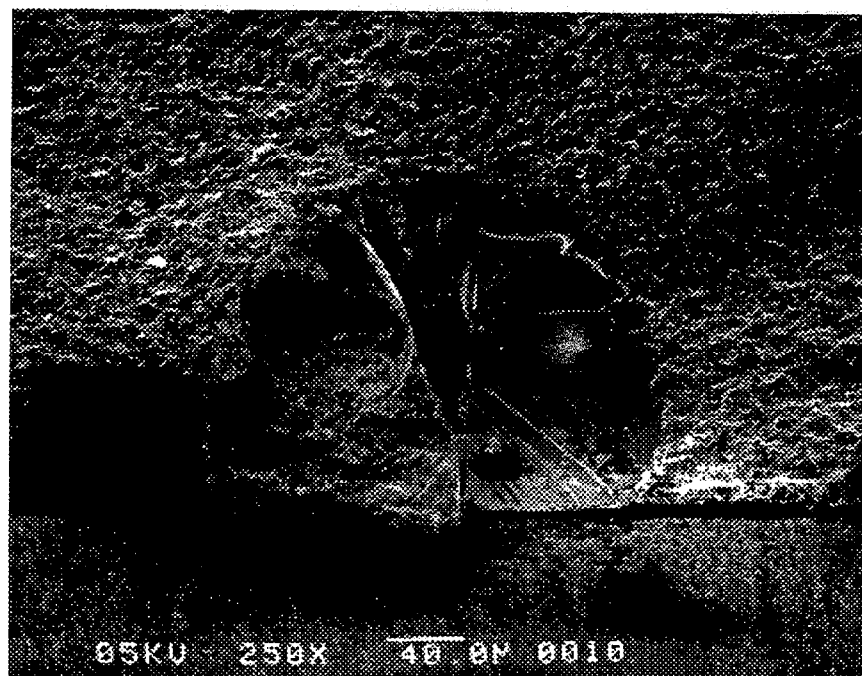


B) 5,000X

**Figure 29: Microstructure of Join Interlayer for Join Made With Initial Unsiliconized Silicon Carbide Parent Material**



A) 50X



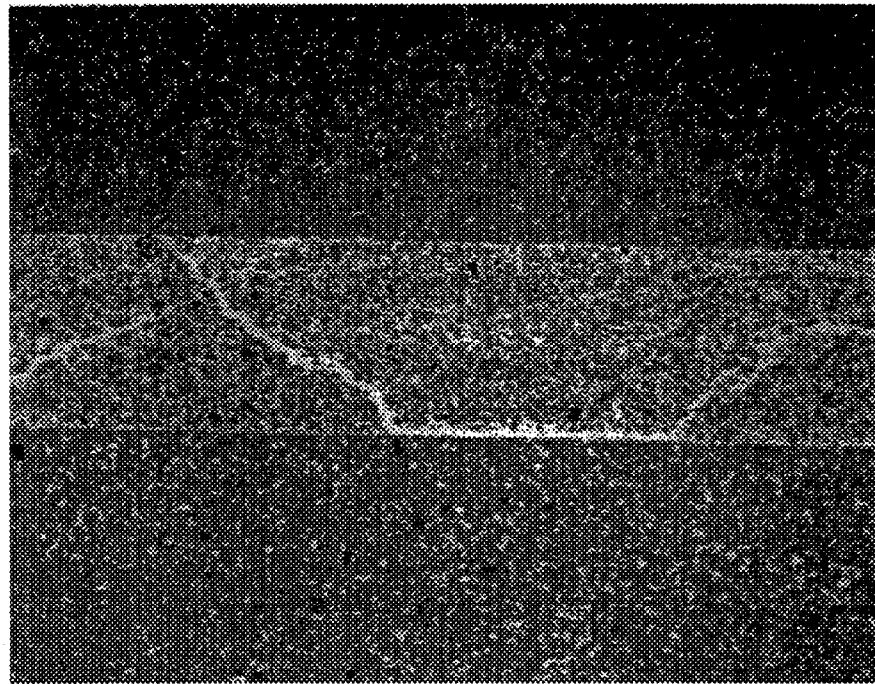
B) 250X

Figure 30: Fracture Origin Within Join Interlayer for Join Made With Initial Siliconized Silicon Carbide

Parent

Join

Parent

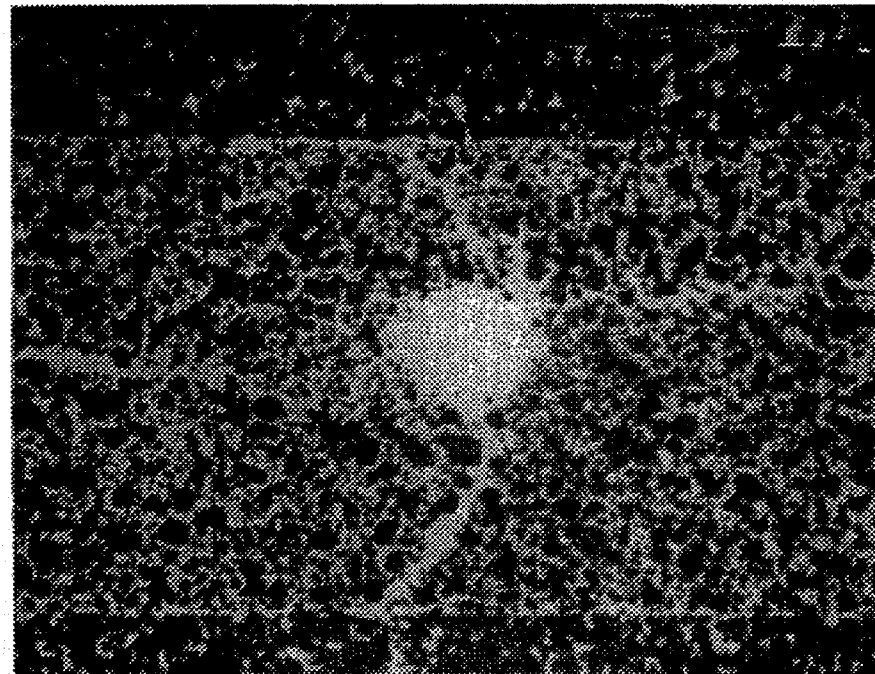


A) 200X

Parent

Join

Parent



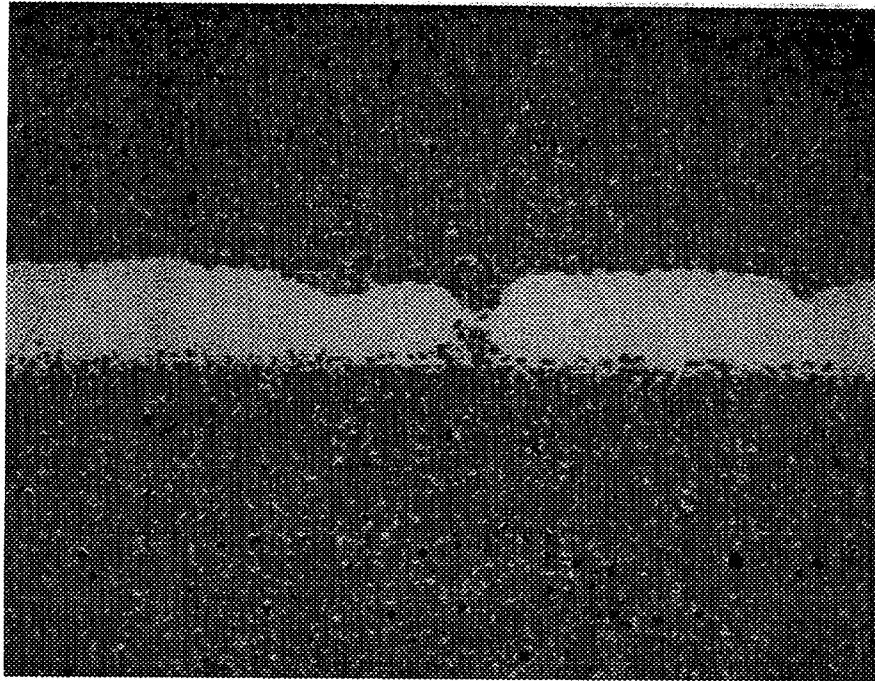
B) 500X

**Figure 31: Optical Micrograph of Join Interlayer B Made With Initially Siliconized Parent Material**

Parent

Join

Parent

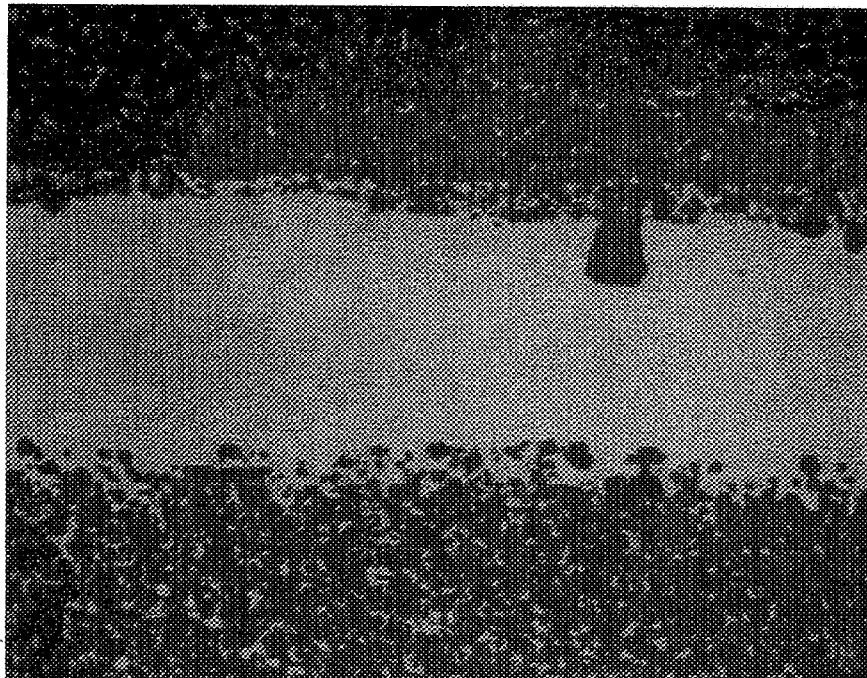


A) 200X

Parent

Join

Parent



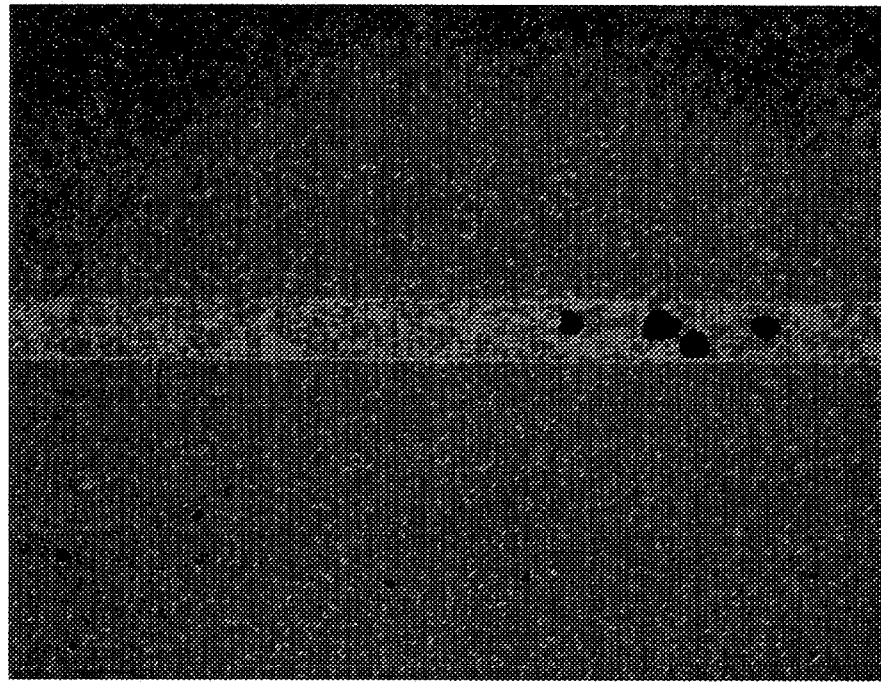
B) 500X

**Figure 32: Optical Micrograph of Join Interlayer C Made With Initially Siliconized Parent Material**

Parent

Join

Parent

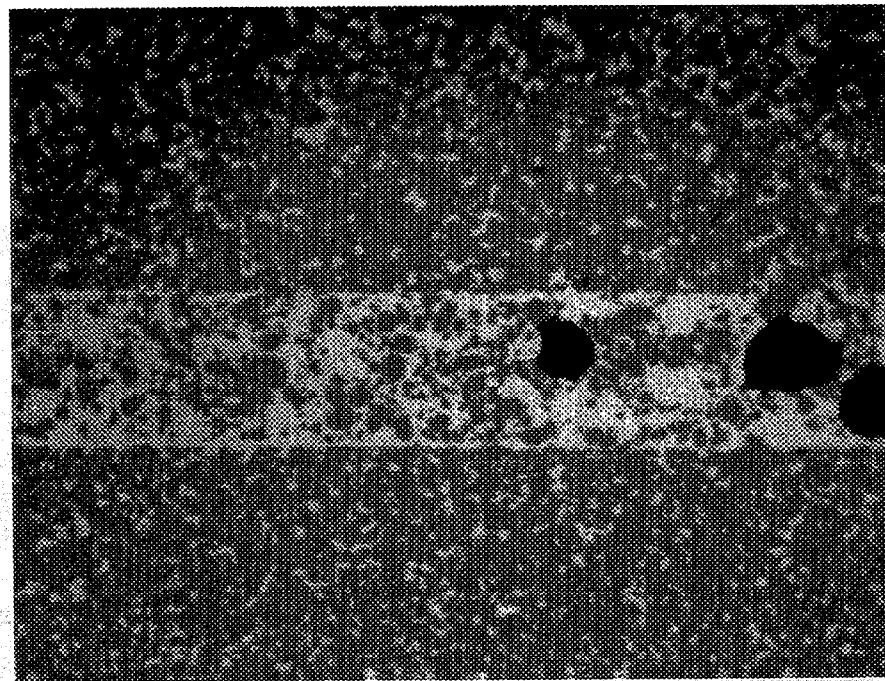


A) 200X

Parent

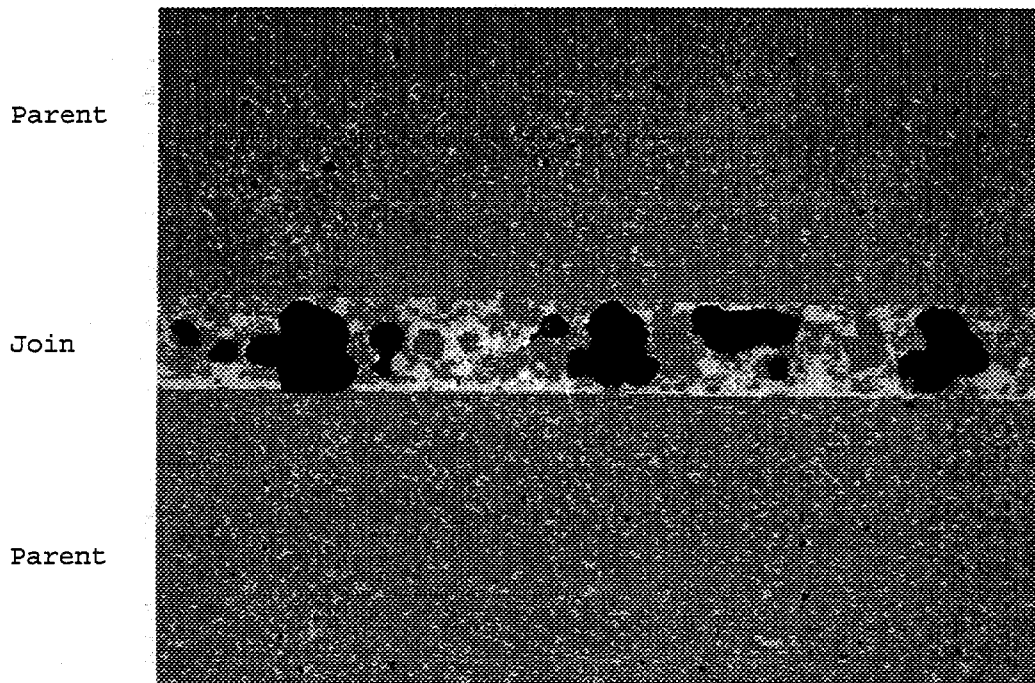
Join

Parent

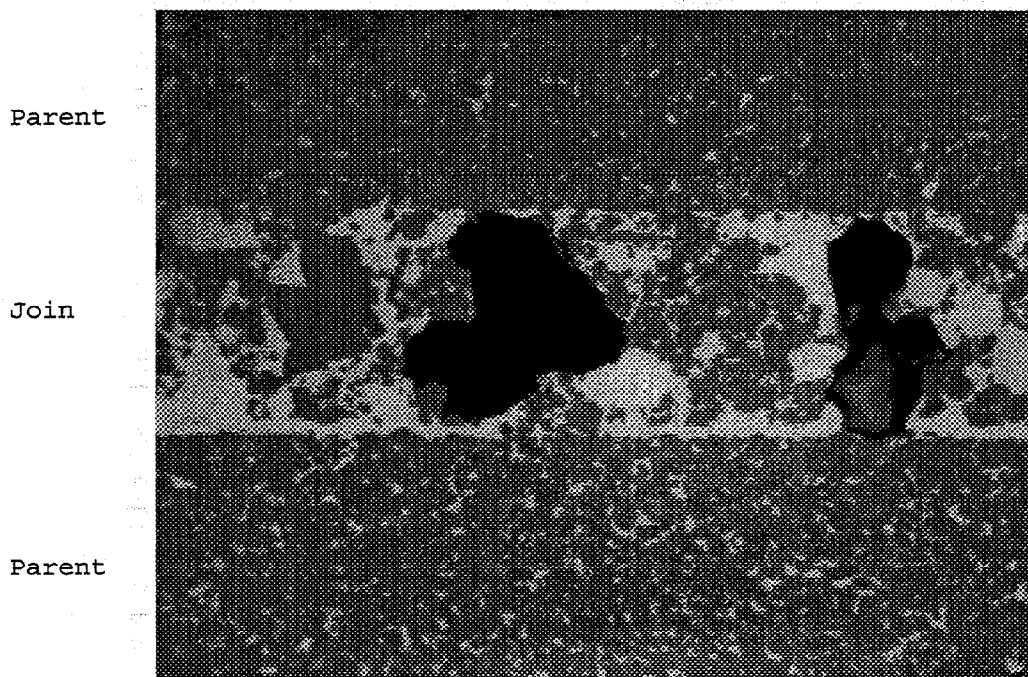


B) 500X

**Figure 33: Optical Micrograph of Join Interlayer D Made With Initially Siliconized Parent Material**



A) 200X



B) 500X

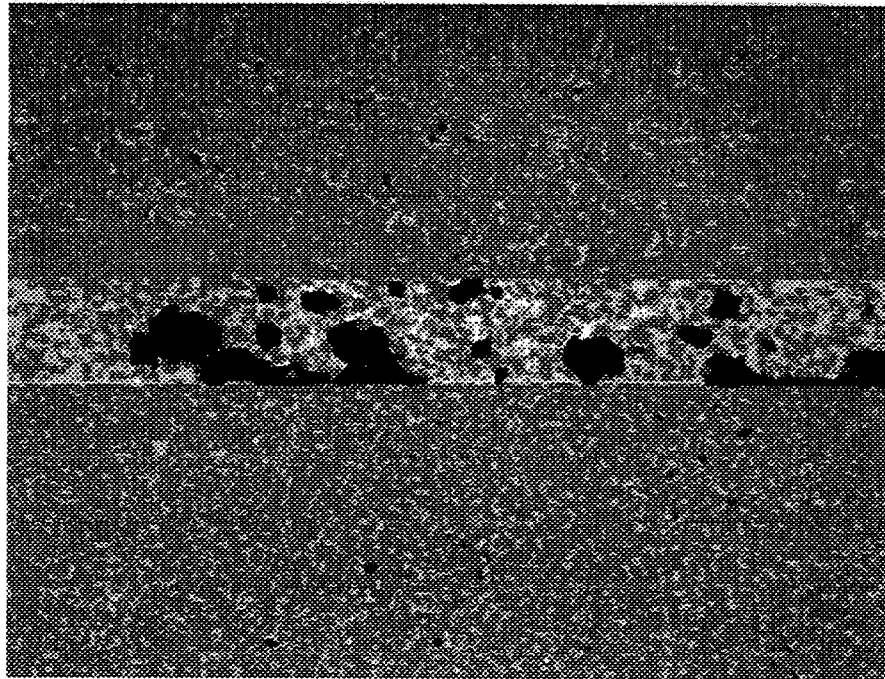
**Figure 34: Optical Micrograph of Join Interlayer E Made With Initially Siliconized Parent Material**



Parent

Join

Parent

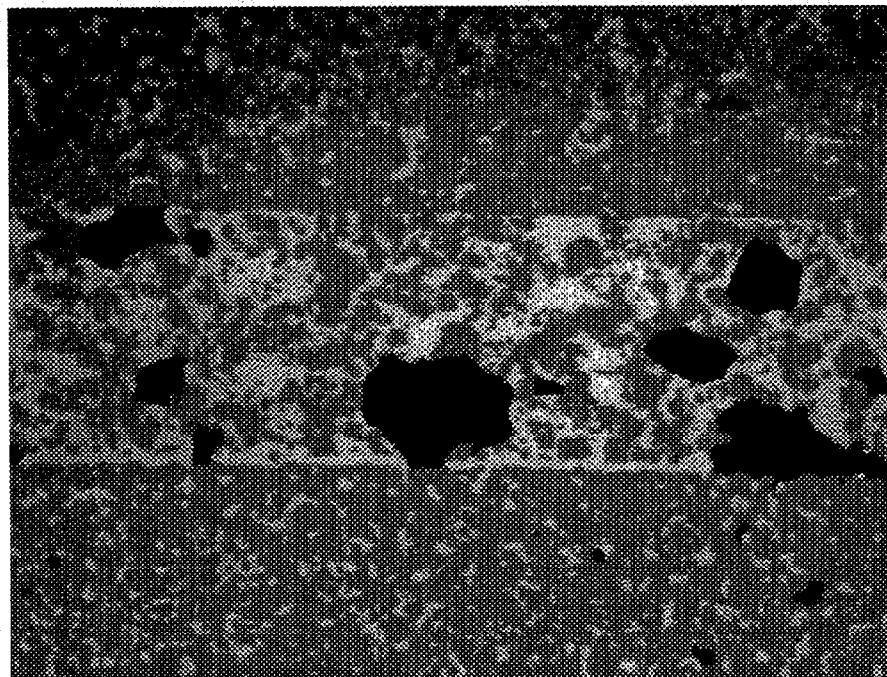


A) 200X

Parent

Join

Parent



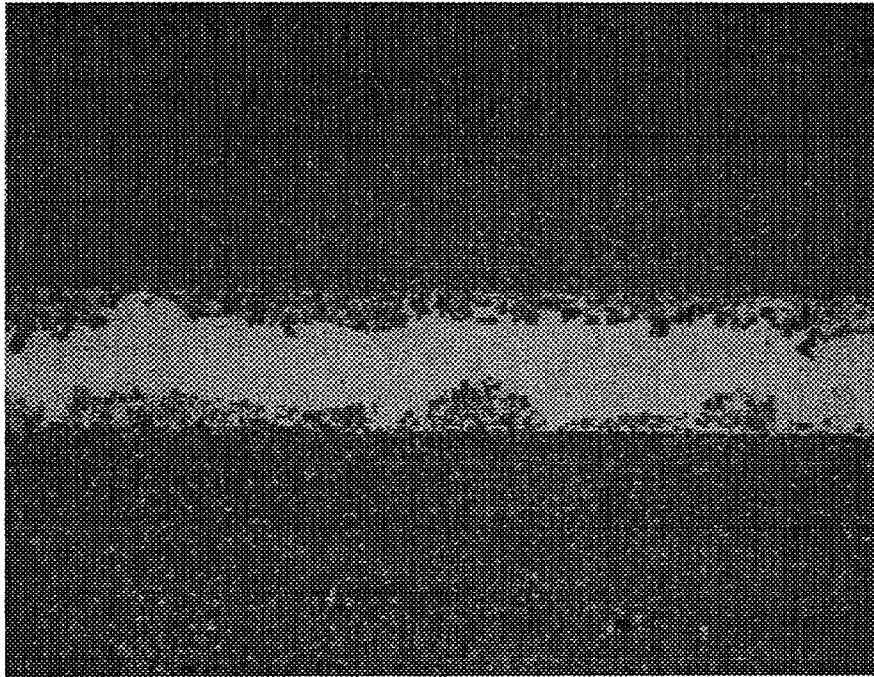
B) 500X

**Figure 35: Optical Micrograph of Join Interlayer F Made With Initially Siliconized Parent Material**

Parent

Join

Parent

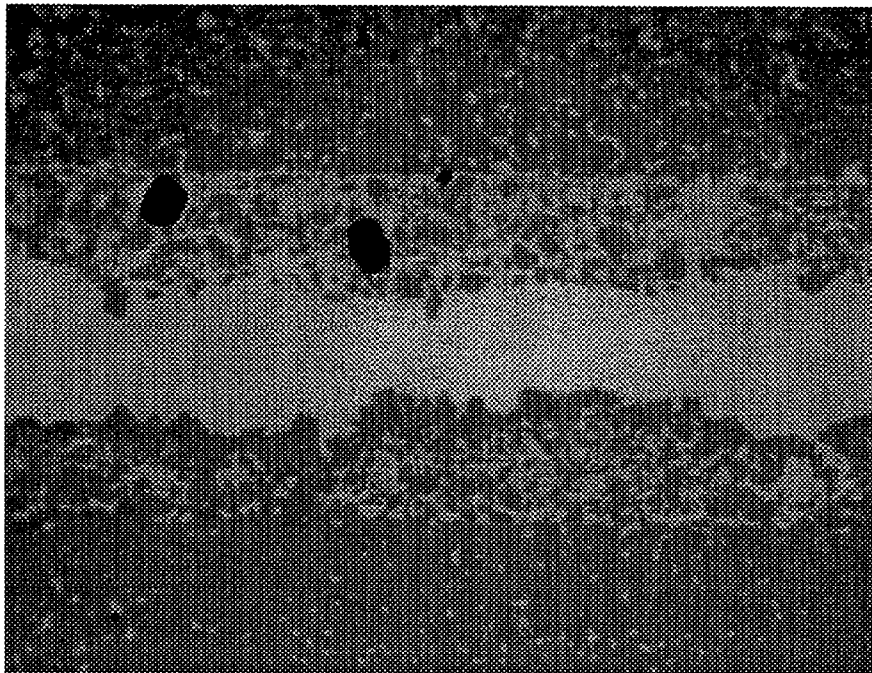


A) 200X

Parent

Join

Parent



B) 500X

**Figure 36: Optical Micrograph of Join Interlayer D Made With Initially Unsiliconized Parent Material**



Table 11: Silicon Carbide Join Summary - Flexure Strength at 22°C

| Billet                             | Interlayer | Flexure Strength (MPa) | Std. Dev. (MPa) | Number Tested | Number of Failed Joins |
|------------------------------------|------------|------------------------|-----------------|---------------|------------------------|
| Siliconized                        | A          | 221.8                  | 40.5            | 10            | 10                     |
| Siliconized                        | B          | 101.11                 | 39.6            | 14            | 14                     |
| Siliconized                        | C          | 141.76                 | 49.7            | 14            | 12                     |
| Siliconized                        | D          | 171.06                 | 39.2            | 14            | 14                     |
| Siliconized                        | E          | 122.87                 | 33.7            | 15            | 15                     |
| Siliconized                        | F          | 127.02                 | 41.0            | 15            | 15                     |
| Unsiliconized                      | D          | 179.53                 | 51.2            | 15            | 12                     |
| Unjoined Control<br>38mm Thickness |            | 232.9                  | 70.5            | 27            |                        |

uniform microstructure and the lowest silicon content (Figure 31). The join S-C and U-D demonstrated extreme silicon enrichment (lighter phase) in the center of the join interlayer with segregation of the silicon carbide (darker phase) at the edges of the interlayer adjacent to the parent materials (Figures 32 and 36). Although the joins S-B, S-D and S-F exhibit a more homogeneous distribution of silicon carbide and silicon, all of the joins lack a contiguous network of silicon carbide that extends into the parent material. All of the join methods resulted in join interlayers that were discrete relative to the parent materials and of higher silicon concentration. The distinct interface between the join interlayer and parent material consisted largely of silicon within the join and silicon carbide within the parent material with an absence of interpenetration across the interface. In addition, voids within the join interlayer are strength limiting and undesirable (Figures 33, 34 and 35).

Additional silicon carbide joining development is required to improve silicon carbide join quality.

## 9 SILICON NITRIDE TENSILE CREEP EVALUATION (TASK 1.1)

## 9.1 TENSILE CREEP RESULTS

The objective of this task was to evaluate the creep characteristics of parent (unjoined) and joined silicon nitride material when isothermally loaded in uniaxial tension at temperatures in the 1275-1425°C range. A summary of the results of the tests for the creep of both joined and parent material (control) specimens is given in Table 12. The table gives the stress, temperature and test time (to failure or suspension) for each specimen tested. The minimum creep rate and total creep strain reported in the table are for the entire gauge section of the specimen (D1,4). If the specimen did not exhibit a secondary creep regime, a minimum creep rate was not calculated and "primary" is entered in its place. Specimen 17-9 was ramped from a stress of 120 MPa to 150 MPa after 100 hours. The specimen had not reached the secondary region at 120 MPa and failed only five hours after the ramp. Consequently, no minimum creep rate was obtained for that specimen at either load.

The end result of each test is listed in the status column of Table 12. For the most part, the test was either suspended or the specimen failed. There were a few instances where the specimen was retested under different conditions which is noted in the status column. The comment for specimen 2-2, Failed (Torque), represents a premature failure of the specimen due to an accidental applied torque. Only one of the specimens, 47-5, had a failure at the pin hole, which is mentioned in the table. These two specimens are not included as failed specimens in later models. The three main locations of failure for the specimens tested were: (1) at the join, (2) at the transition region stress concentration (described in section 7.1.1) and (3) in the gauge section away from the join.

The classical characterization of creep deformation involves three regimes identified as primary, secondary and tertiary creep. Primary creep occurs at the beginning of the high temperature loading where strain rate rapidly decreases to a near constant value which is maintained during the secondary creep regime. The tertiary creep regime is identified by an inflection point in the creep curve where the strain rate increases above the secondary creep level. The strain rate continuously increases during this regime which is terminated by rupture.<sup>10</sup>

The creep test curves display a significant primary creep regime. However, none of the creep data, for tests as long as 1,692 hours, exhibit tertiary behavior when using the classical creep interpretation. An approximation to the steady state creep rate was established for those specimens which clearly deformed beyond the primary creep regime. The procedure taken here was to identify the nearly linear portion of the creep versus time curve, for the entire gauge section (D1,4), just prior to failure or test termination. This quasi-linear region was fit with a straight line and the slope of that line was used as the minimum or quasi-steady state creep rate.

Strain variations were observed along the gauge length within a given specimen. The strain variation within specimens was greatest between segments D1,2 and D3,4 which contained only the parent material without the join interlayer. The percent difference of strain at test termination between opposing halves of the parent material typically ranged between 5% to 57%. Specimen to specimen variability was also observed in tests conducted under identical conditions.

The data acquisition method was reviewed to ensure apparent strain variation was not an artifact induced by systematic error. No detectable temperature gradient was measured in the furnace hot zone at the creep gauge section when monitored with thermocouples. The high and low strain measurements for creep specimens were randomly oriented at the upper and

Table 12: Silicon Nitride Creep Test Summary

| Specimen Number | Specimen Type | Stress (MPa) | Temp (C) | Minimum Creep Rate (1/hours) | Test Time (hours) | Total Creep | Status               | Failure Location |
|-----------------|---------------|--------------|----------|------------------------------|-------------------|-------------|----------------------|------------------|
| 30-3            | Joined        | 100          | 1395     | Primary                      | 7                 | 0.0029      | Failed               | Join             |
| 19-2            | Joined        | 100          | 1422     | 1.775E-05                    | 476               | 0.0124      | Suspended            |                  |
| 19-4            | Joined        | 100          | 1422     | 1.829E-05                    | 444               | 0.0137      | Suspended            |                  |
| 46-2            | Control       | 100          | 1425     | 2.555E-05                    | 486               | 0.0173      | Failed               | Transition       |
| 20-9            | Joined        | 120          | 1327     | Primary                      | 448               | 0.0014      | Retested as 20-9a    |                  |
| 30-5            | Joined        | 120          | 1350     | 3.045E-06                    | 425               | 0.0033      | Retested as 30-5a    |                  |
| 17-9            | Joined        | 120,150      | 1388     | Primary                      | 105               | 0.0038      | Failed               | Gauge            |
| 19-7            | Joined        | 120          | 1392     | 8.263E-06                    | 669               | 0.0080      | Suspended            |                  |
| 17-8            | Joined        | 120          | 1395     | 1.132E-05                    | 601               | 0.0113      | Failed               | Transition       |
| 19-1            | Joined        | 120          | 1395     | 8.897E-06                    | 475               | 0.0075      | Suspended            |                  |
| 46-1            | Control       | 120          | 1397     | 1.097E-05                    | 504               | 0.0076      | Suspended            |                  |
| 20-2            | Joined        | 120          | 1418     | 2.187E-05                    | 448               | 0.0119      | Suspended            |                  |
| 47-2            | Control       | 120          | 1425     | Primary                      | 139               | 0.0103      | Suspended            |                  |
| 47-3            | Control       | 120          | 1427     | 2.615E-05                    | 407               | 0.0151      | Failed               | Transition       |
| 20-1            | Joined        | 120          | 1427     | 2.434E-05                    | 202               | 0.0076      | Failed               | Join             |
| 20-3            | Joined        | 120          | 1427     | 2.012E-05                    | 384               | 0.0112      | Failed               | Transition       |
| 30-4            | Joined        | 140          | 1422     | Primary                      | 3                 | 0.0032      | Failed               | Join             |
| 20-9a           | Joined        | 140          | 1300     | 6.603E-07                    | 680               | 0.0004      | Continuation of 20-9 |                  |
| 28C             | Joined        | 141          | 1370     | 1.236E-05                    | 170               | 0.0055      | Suspended            |                  |
| 36B             | Joined        | 145          | 1370     | 1.797E-05                    | 134               | 0.0046      | Suspended            |                  |
| 22E             | Joined        | 146          | 1370     | 1.931E-05                    | 144               | 0.0034      | Suspended            |                  |
| 47-5            | Control       | 150          | 1325     | 3.036E-06                    | 311               | 0.0021      | Failed at pin hole   |                  |
| 1-1             | Joined        | 150          | 1350     | 1.403E-05                    | 206               | 0.0044      | Failed               | Transition       |
| 17-1            | Joined        | 150          | 1370     | 4.030E-05                    | 93                | 0.0043      | Failed               | Join             |
| 17-4            | Joined        | 150          | 1370     | Primary                      | 24                | 0.0039      | Failed               | Gauge            |
| 22B             | Joined        | 150          | 1370     | 2.097E-05                    | 149               | 0.0047      | Suspended            |                  |
| 47-1            | Control       | 150          | 1388     | 5.442E-05                    | 72                | 0.0048      | Suspended            |                  |
| 46-3            | Control       | 150          | 1392     | 4.364E-05                    | 141               | 0.0102      | Failed               | Gauge            |
| 1-5             | Joined        | 175          | 1300     | 2.889E-06                    | 363               | 0.0018      | Suspended            |                  |
| 20-7            | Joined        | 175          | 1318     | 2.967E-06                    | 819               | 0.0060      | Suspended            |                  |
| 30-2            | Joined        | 175          | 1322     | Primary                      | 130               | 0.0036      | Failed               | Transition       |
| 20-8            | Joined        | 175          | 1327     | 1.272E-06                    | 1100              | 0.0032      | Suspended            |                  |
| 30-6            | Joined        | 175          | 1350     | 1.769E-05                    | 223               | 0.0059      | Failed               | Transition       |
| 30-5a           | Joined        | 175          | 1350     | 3.620E-06                    | 687               | 0.0056      | Continuation of 30-5 |                  |
| 33E             | Joined        | 190          | 1300     | 7.856E-06                    | 126               | 0.0025      | Suspended            |                  |
| 2-1             | Joined        | 200          | 1300     | 5.090E-06                    | 350               | 0.0032      | Retested as 2-1a     |                  |
| 2-2             | Joined        | 200          | 1300     | 4.151E-06                    | 110               | 0.0018      | Failed (Torque)      |                  |
| 2-3             | Joined        | 200          | 1300     | 3.906E-06                    | 753               | 0.0048      | Suspended            |                  |
| 2-1a            | Joined        | 200          | 1325     | 1.444E-05                    | 50                | 0.0011      | 2-1 Continued        | Transition       |
| 17-5            | Joined        | 200          | 1325     | 1.195E-05                    | 233               | 0.0046      | Failed               | Transition       |
| 1-2             | Joined        | 200          | 1350     | 1.357E-04                    | 8                 | 0.0017      | Failed               | Transition       |
| 1-3             | Joined        | 200          | 1350     | 6.902E-05                    | 26                | 0.0030      | Failed               | Transition       |
| 34B             | Joined        | 210          | 1300     | 1.026E-05                    | 159               | 0.0034      | Failed               | Gauge            |
| 19-9            | Joined        | 225          | 1268     | 1.650E-06                    | 506               | 0.0027      | Failed               | Transition       |
| 19-8            | Joined        | 225          | 1277     | 1.091E-06                    | 1692              | 0.0029      | Suspended            |                  |
| 17-6            | Joined        | 225          | 1318     | 4.927E-05                    | 54                | 0.0093      | Failed               | Transition       |
| 20-5            | Joined        | 225          | 1318     | 4.105E-05                    | 42                | 0.0019      | Suspended            |                  |
| 47-4            | Control       | 225          | 1322     | 3.205E-05                    | 70                | 0.0039      | Failed               | Gauge            |
| 30-1            | Joined        | 225          | 1352     | Primary                      | < 1               | 0.0008      | Failed               | Gauge            |
| 20-4            | Joined        | 250          | 1272     | Primary                      | 8                 | 0.0004      | Failed               | Transition       |
| 20-6            | Joined        | 250          | 1272     | 2.253E-06                    | 936               | 0.0043      | Suspended            |                  |
| 19-6            | Joined        | 250          | 1275     | 2.689E-06                    | 890               | 0.0049      | Failed               | Join             |
| 2-5             | Joined        | 250          | 1285     | 4.866E-06                    | 447               | 0.0040      | Failed               | Gauge            |
| 2-4             | Joined        | 250          | 1300     | 6.428E-05                    | 18                | 0.0018      | Failed               | Gauge            |

lower ends of the creep specimen. The strain of the center segment (D2,3) and the overall gauge length (D1, 4) represented the creep of the join interlayer and the entire aggregate joined body, respectively, and correlated well with the weighted average of the measured creep segments (Figure 37) for all specimens. These findings confirm the measured strain variation to be an actual behavior difference and not an artifact from data acquisition.

Results indicate that creep strain variability also exists within the NCX-5101 unjoined (control) specimens (Figure 38). This suggests that creep strain variability is inherent in the silicon nitride. There was no apparent evidence that the joining process contributed to the creep strain variability observed in the joined specimens.

Fourteen of the 27 specimens which ruptured did so at the transition stress concentrator. Only five of the 23 joined creep specimens that failed did so at the join (Table 12). Several failed specimens were sectioned and analyzed with SEM. Analysis of micrographs showed the primary creep mechanism to be cavitation at two grain junctions (Figure 39).

## 9.2 MODELING OF CREEP

### 9.2.1 Steady State Creep Rate Model

Successful mechanical design methodology can be expected to include prediction of creep deformation which accumulates over the lifetime of high performance ceramic heat engine components. Designs which fully utilize the potential of high temperature ceramics will involve critical structural locations of components experiencing fully developed secondary creep over the majority of the component's life. This requires an analytical approach to generalize the experimental findings on the stress and temperature dependence of the steady state creep rate.

The literature documents an extensive history of representing the stress dependence of the strain rate by a power law form both for metals<sup>11</sup> and ceramics<sup>12</sup>. This relationship is referred to as Norton's law, following the original publication by F.H. Norton<sup>13</sup> on the creep of steel. The temperature dependence of strain rate has been typically represented by an Arrhenius form to yield the following expression for the steady state strain rate  $\dot{\epsilon}_s$ :

$$\dot{\epsilon}_s = A\sigma^n e^{-Q/RT} \quad (4)$$

Here A and n are material constants,  $\sigma$  is the applied stress, Q is the apparent activation energy for creep, R is the universal gas constant, and T is the absolute temperature. In order to fit the data shown in Table 12 to Equation 4 first consider the natural logarithm of Equation 4:

$$\ln \dot{\epsilon}_s = \ln A + n \ln \sigma - \frac{Q}{RT} \quad (5)$$

The values of Q, n, and A can be determined from plotting  $\ln(\dot{\epsilon}_s)$  against various parameters. The value of Q was determined from plotting  $\ln(\dot{\epsilon}_s)$  versus  $1/T$  at constant stress (Figure 40). The value of Q is the negative of the slope of such a curve multiplied by the universal gas constant (R). In Figure 40 we see that the calculated value of the apparent activation energy, Q, varies with the value of the applied stress. There is an approximately linear increase in Q with stress. This trend has also been observed for the creep of sintered silicon

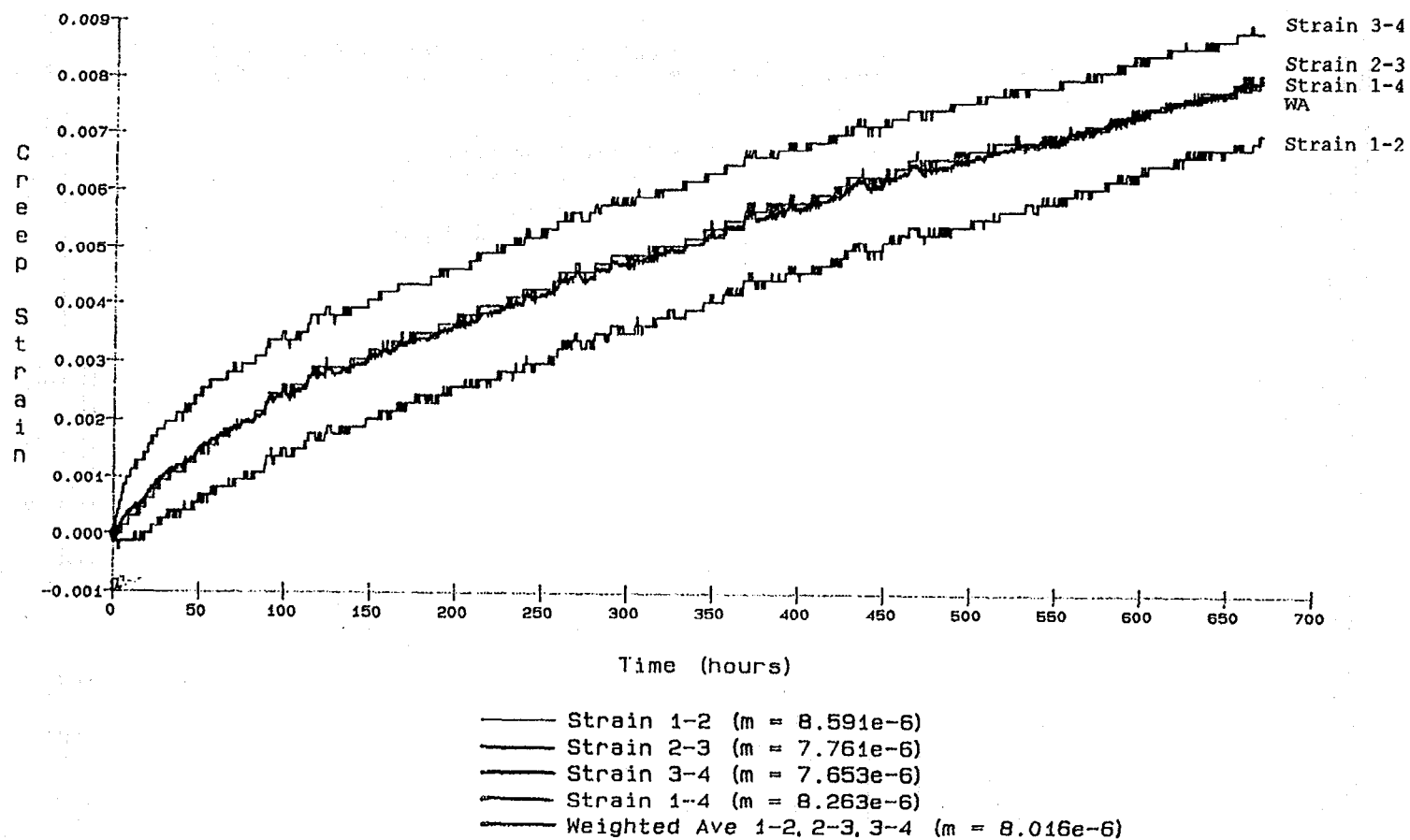


Figure 37: Creep Strain as a Function of Time for Silicon Nitride Butt Join #19-7 at 1392°C and 120 MPa. Test Suspended After 669 Hours.

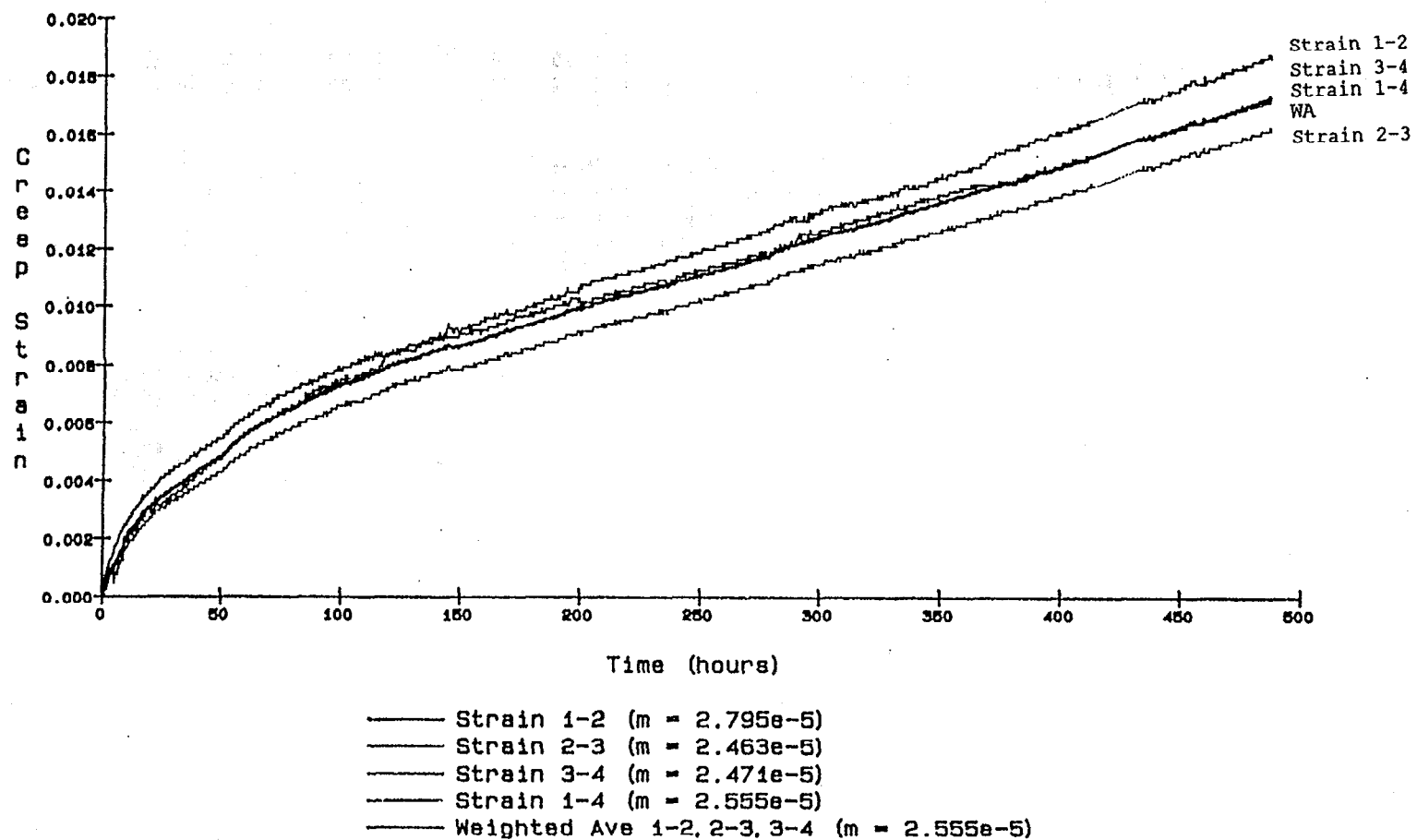
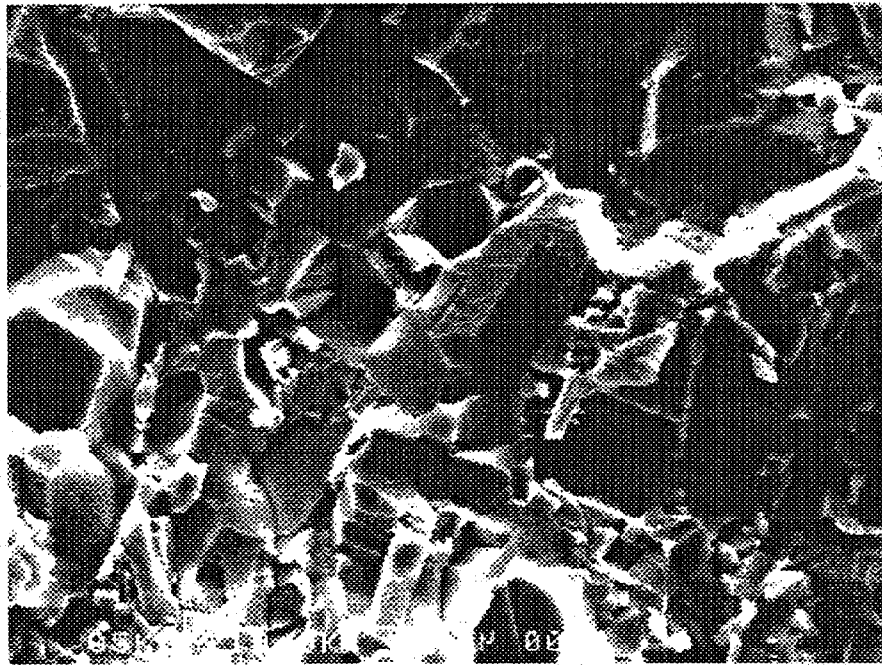


Figure 38: Creep Strain as a Function of Time for Silicon Nitride Unjoined Control #46-2 at 1425°C and 100 MPa. Specimen Failed at 486 Hours.



A) 10,000X



B) 20,000X

**Figure 39: NCX-5101 Silicon Nitride Joined Tensile Specimen After Creep Testing Exhibiting Cavitation**

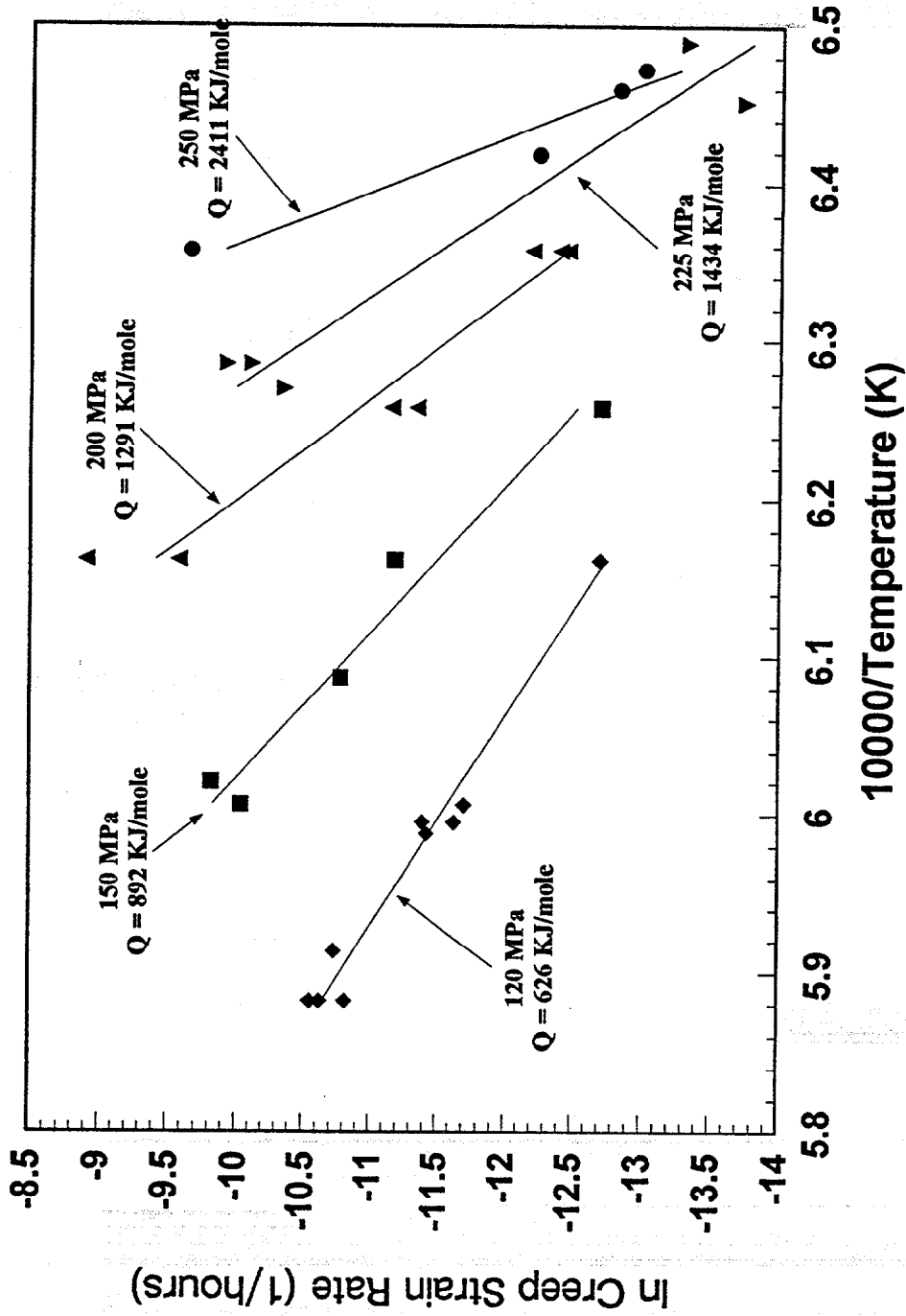


Figure 40: Determination of the Activation Energy (Q) as a Function of Stress



nitride<sup>12</sup>. The range of measured values in  $Q$  going from 626 KJ/mole to 1434 KJ/mole is consistent with other values from the literature<sup>14, 15</sup>. The value for  $Q=2411$  KJ/mole shown for 250 MPa is not considered to be real since it is strongly influenced by a data point which appears to be an outlier. This phenomenon of increasing  $Q$  with stress needs further investigation. There is evidence from the literature of the creep of metals for  $Q$  to decrease with stress but not to increase. There has been data generated on NCX-5101 class materials that demonstrates that grain boundary devitrification occurs with thermal aging<sup>16</sup>. It is possible that this phenomenon which translates into improved creep resistance is promoted by stress thus explaining the observed increasing  $Q$  with stress. Additional evaluation of this phenomenon was beyond the scope of this study.

The value of  $n$  was determined from the slope of a  $\ln(\dot{\epsilon}_s)$  versus  $\ln(\sigma)$  plot at constant temperature (Figure 41). The values of  $n$  showed some variation but were centered around a value of 7 for all of the temperatures except for the results at 1420°C. This possibly suggests a change of mechanism at this temperature.

In order to apply Equation 4 in a finite element analysis to model creep deformation in notched creep specimens which were tested, unique representative values of  $A$ ,  $Q$  and  $n$  were sought. An iterative procedure was used, starting with the average value  $n=7.52$  obtained by excluding the 1420°C data in Figure 41. Rearranging Equation 5 as:

$$\ln(\dot{\epsilon}_s \sigma^{-n}) = \ln A - \frac{Q}{RT} \quad (6)$$

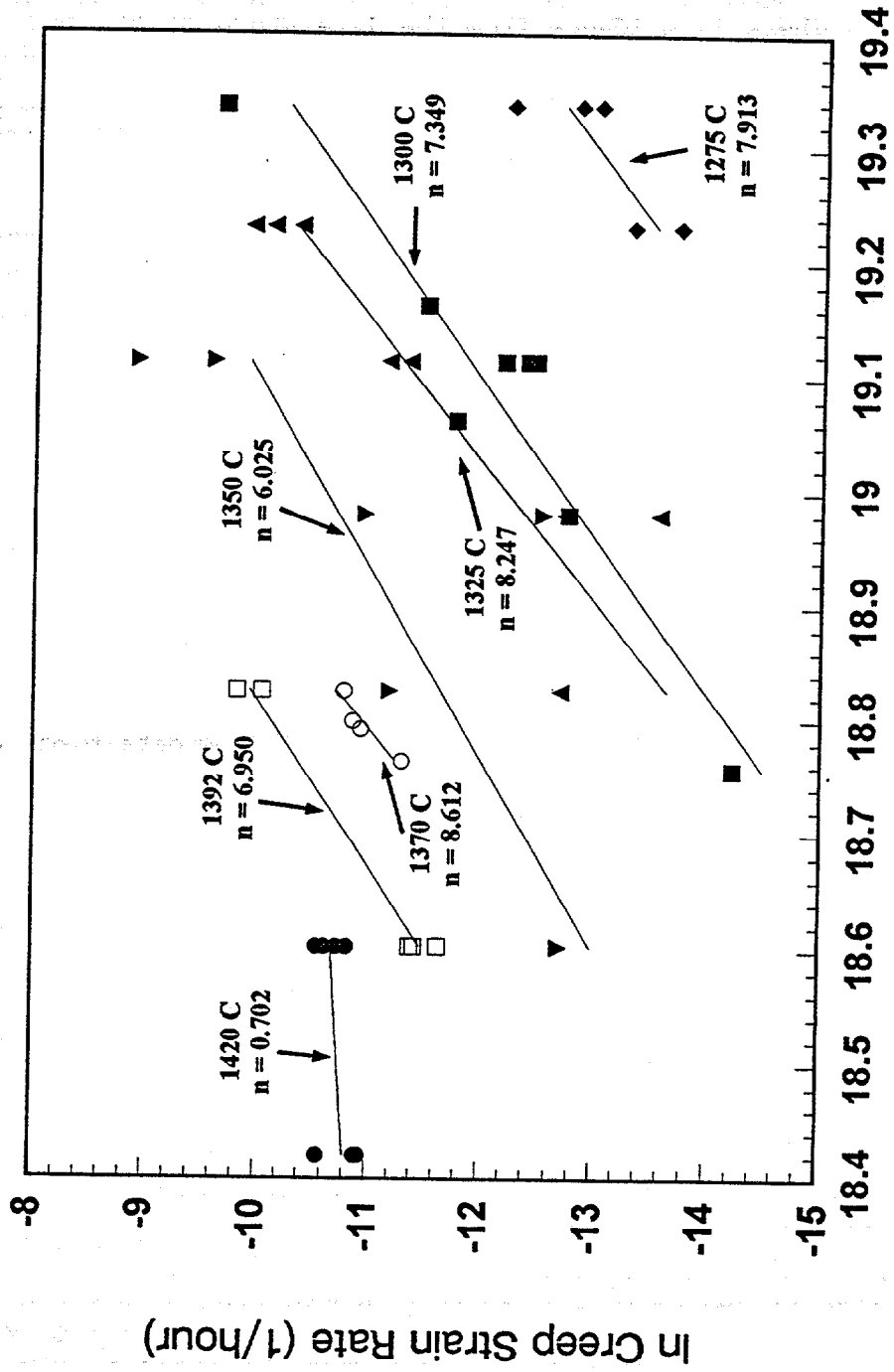
provides a way to obtain values of  $A$  and  $Q$  which correspond to the average value of  $n$ . The value of  $-Q/R$  is the slope of the line fit to  $\ln(\dot{\epsilon}_s \sigma^{-n})$  versus  $1/\text{Temperature}$  and  $\ln A$  is the intercept of this line. Likewise, an improved estimate for  $n$  can be deduced from data plotted to the form:

$$\ln(\dot{\epsilon}_s e^{Q/RT}) = \ln A + n \ln \sigma \quad (7)$$

This value for  $n$  can then be used to determine a new value of  $Q$  using the procedure corresponding to Equation 6. This procedure can then be repeated as many times as necessary to give converged values for  $n$ ,  $Q$  (and  $A$ ). In practice it took only one iteration to converge to the values of  $n=7.53$ ,  $Q=1138$  KJ/mole, and  $A=8.28 \times 10^{-31}$  Pa<sup>-7.53</sup>/hour from Figures 42 and 43. These values were calculated excluding data at 1420°C which gave a low  $n$  value, excluding 250 MPa data which gave a high  $Q$  value and excluding 175 MPa data because of the excessively high scatter in that data. These are the values for the material parameters that were used to characterize the range of creep experiments. A calculation for these material parameters was also done based on all the data. The average value of  $n=7.52$  was again used to start the iterative procedure. After 15 iterations, values of  $Q=1158$  KJ/mole and  $n=7.20$  were obtained, which are very similar to the previous results.

In order to evaluate how well the first set of constants represents the database as a whole, a three dimensional plot is given in Figure 44. In this plot a surface is drawn which represents the creep strain rate given by Equation 4 using the constants determined above. In addition to this surface given by the model, the individual data points are also plotted. There is a 68% average difference between the model predictions and the experimental points. This fit is good considering that only three material constants are used to correlate dozens of experiments.

## NCX-5100

Figure 41: Determination of the Stress Exponent ( $n$ ) as a Function of Temperature

# NCX-5100

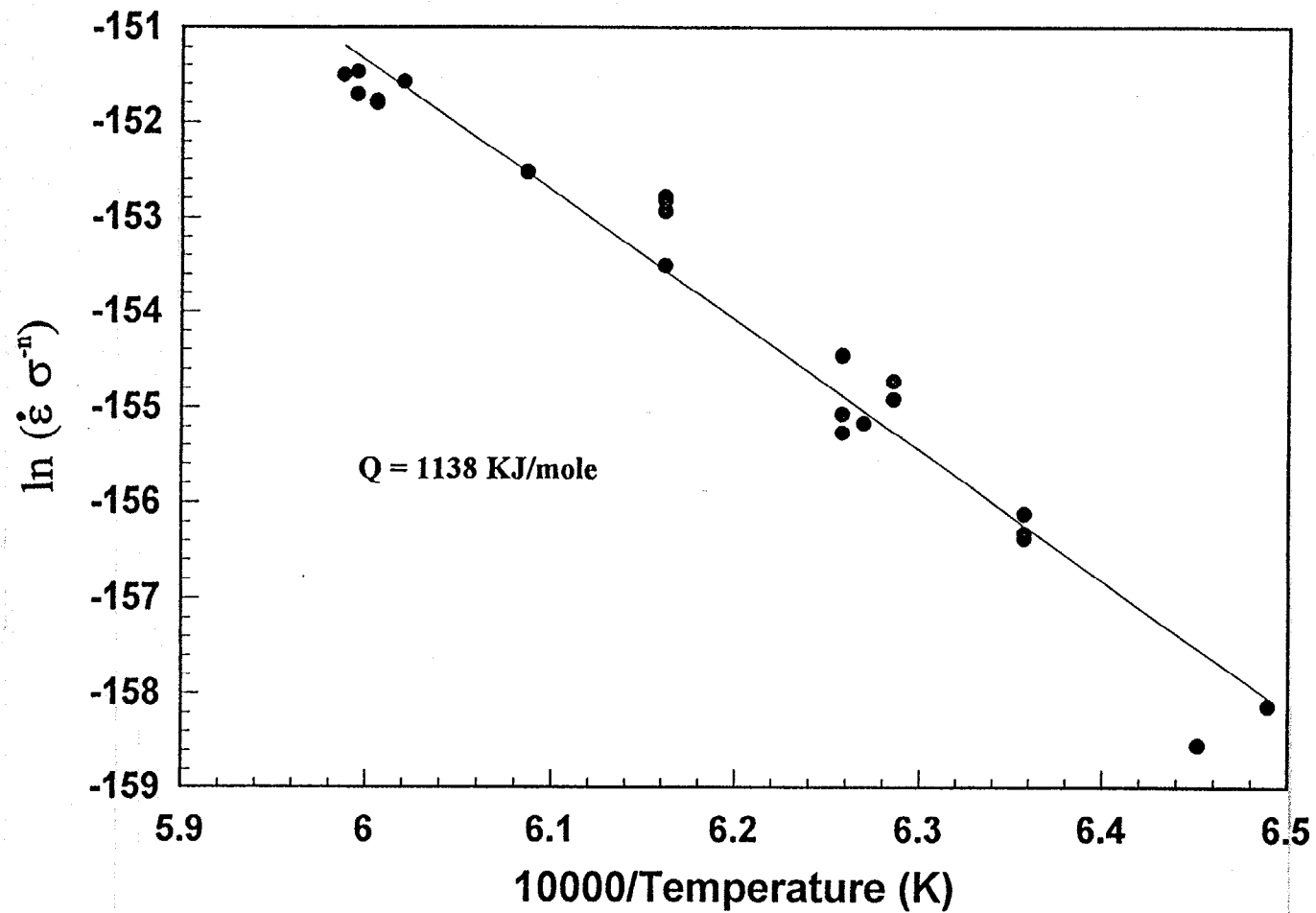


Figure 42: Determination of a Single Activation Energy (Q)

# NCX-5100

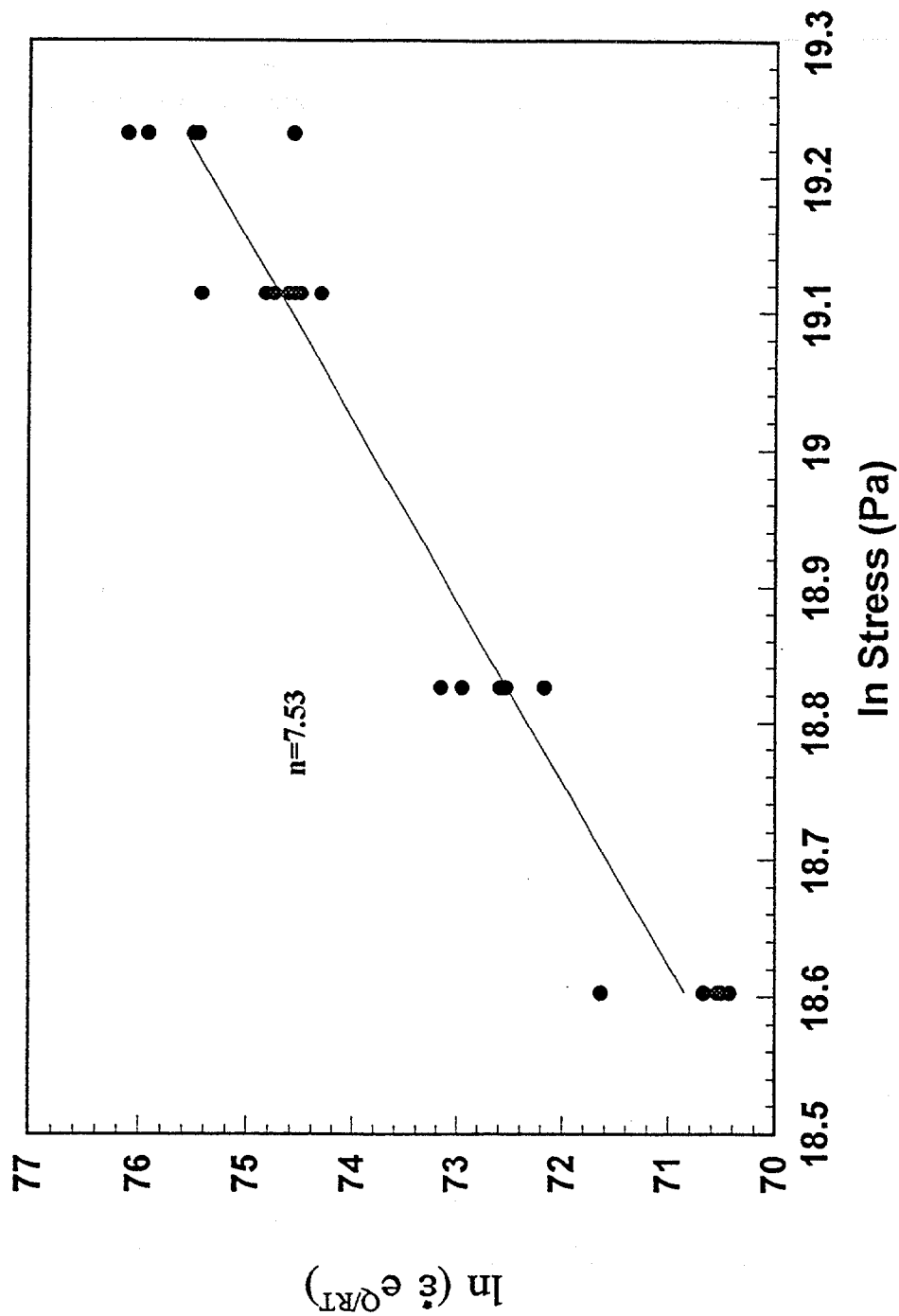


Figure 43: Determination of a Single Stress Exponent (n)

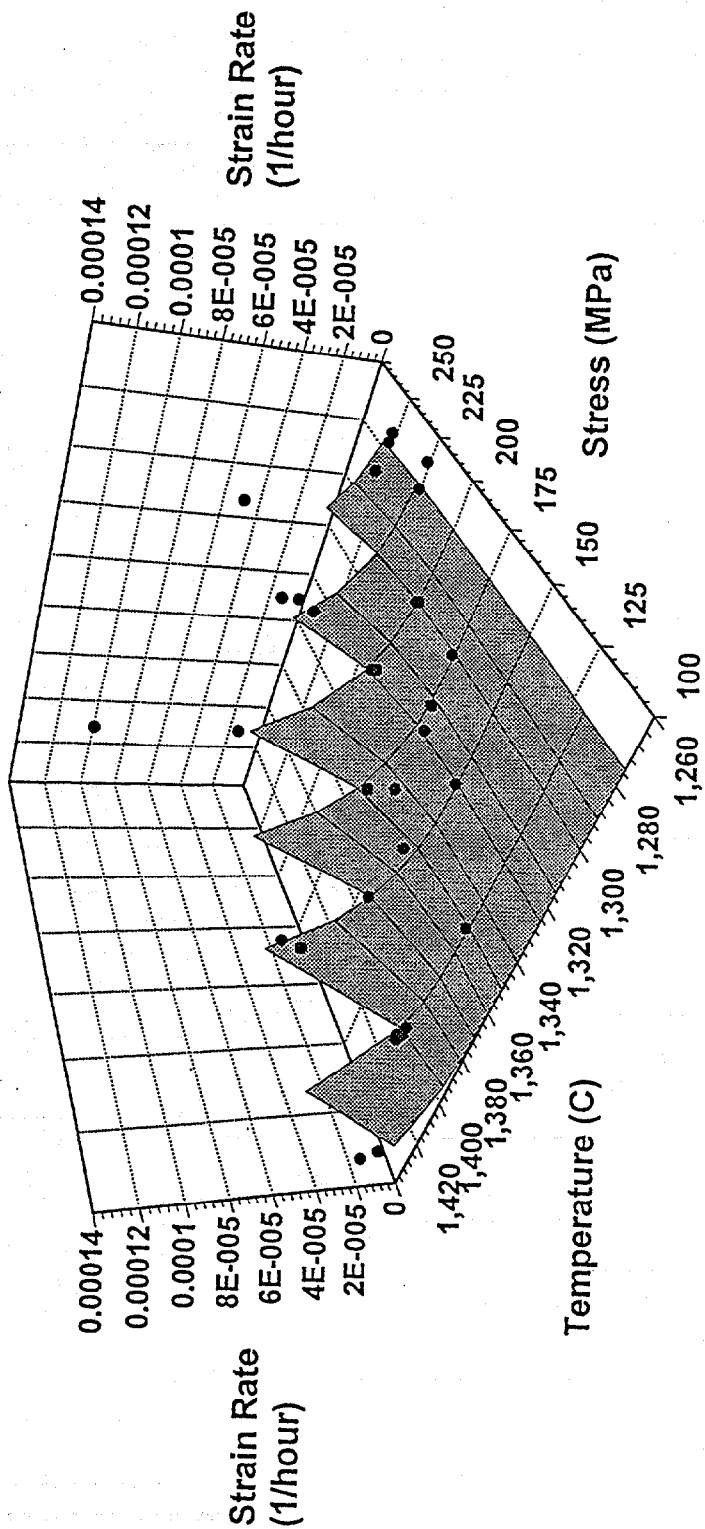


Figure 44: Creep Strain Rate Prediction Versus Experimental Results

### 9.2.2 Failure Modeling

The time to failure for each of the specimens which ruptured is given in Table 12. Twenty-nine of the 51 specimens were tested until failure. Of the 29, seven failed in the primary regime, two were premature failures (pin hole failure and accidental applied torque to specimen), and one (2-1) was tested at two different stresses. This leaves 19 valid data points for failure modeling. The time to failure of these specimens is plotted in Figure 45 versus minimum creep rate. The trend of the data suggests agreement with the Monkman-Grant<sup>17</sup> relationship:

$$\dot{\epsilon}_s^\beta t_f = C \quad (8)$$

where  $t_f$  is the time to failure and the Monkman-Grant parameters  $\beta$  and  $C$  are 1.43 and  $2.95 \times 10^{-5} \text{ hr}^{-0.43}$  when the 19 data points are included in a linear regression. It is important to note that 11 of the 19 ruptured specimens included in Figure 45 failed at the section where the transition region blends into the straight gauge length. This section is beyond the range of the creep measurement flags so that the  $\dot{\epsilon}_s$  values for these specimens, although accurate for the gauge section, are not consistent with the rupture time data.

Data for the eight gauge/join failures are plotted separately in Figure 46 and provide values of 1.17 for  $\beta$  and  $4.11 \times 10^{-4} \text{ hr}^{-0.17}$  for  $C$ . The Monkman-Grant approach is motivated by the theory that rupture occurs at a critical value of accumulated creep strain (ie.  $\beta=1$ ). On this basis, the  $\beta$  value of 1.17 is considered more accurate than the  $\beta$  value of 1.43 calculated previously for all ruptured specimens used in Figure 45.

### 9.2.3 Prediction of Creep Failure of Notched Tensile Specimens

The development of material models are useful only insofar as the model can be used to predict the performance of structural components. The finite element method is the most popular and, arguably, the most flexible numerical method for application of advanced material laws to actual components. An investigation to use these models in the prediction of the response of complex members has been pursued in conjunction with the development of material models to describe the joins and parent material.

The results being reported here involve incorporating the Norton's law modeling into a finite element code and demonstrating how it can be used to predict the mechanical response of a structure.

The commercially available finite element code ANSYS<sup>6</sup> has been used in this work. Since the strain rates evolve with time and temperature the solution must be tracked in an incremental manner. The one-dimensional Norton's law can be generalized to represent multiaxial deformation as follows:

$$\dot{\epsilon}_{ij}^{cr} = A \sigma_e^n e^{-Q/RT} \frac{3}{2} \frac{\sigma'_{ij}}{\sigma_e}, \quad (9)$$

where  $\sigma'_{ij}$  is the stress deviator tensor, and  $\sigma_e$  is the equivalent stress ( $\sigma_e = (3/2 \sigma'_{ij} \cdot \sigma'_{ij})^{1/2}$ ). The total strain rate is given as the sum of the elastic strain rate and the creep strain rate as given above.

Several criteria were used to select a component to apply the finite element method. The component was required to have: (1) a nonuniform stress and strain distribution, primarily tensile loading

## NCX-5100

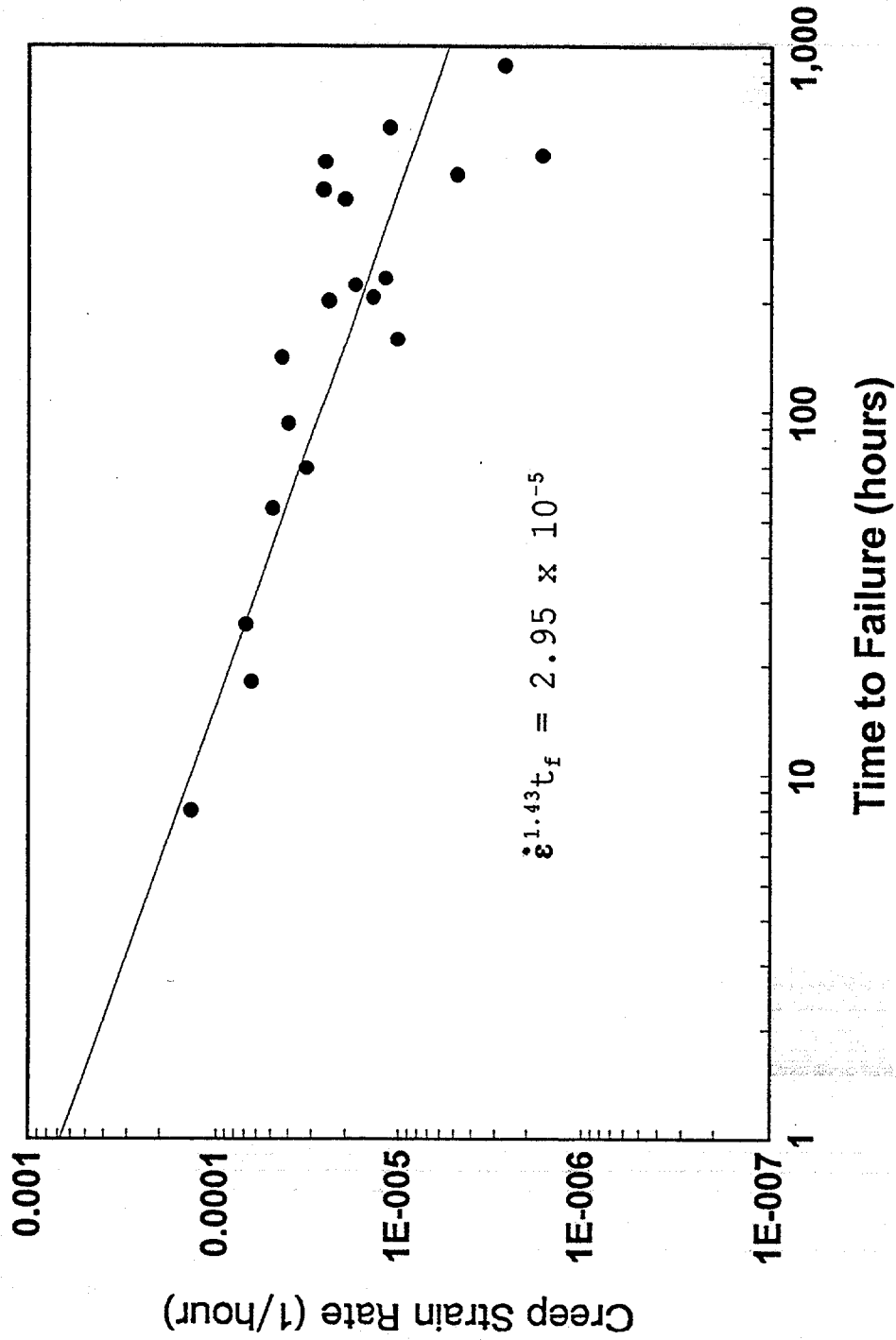


Figure 45: Monkman-Grant Relationship for All Failures

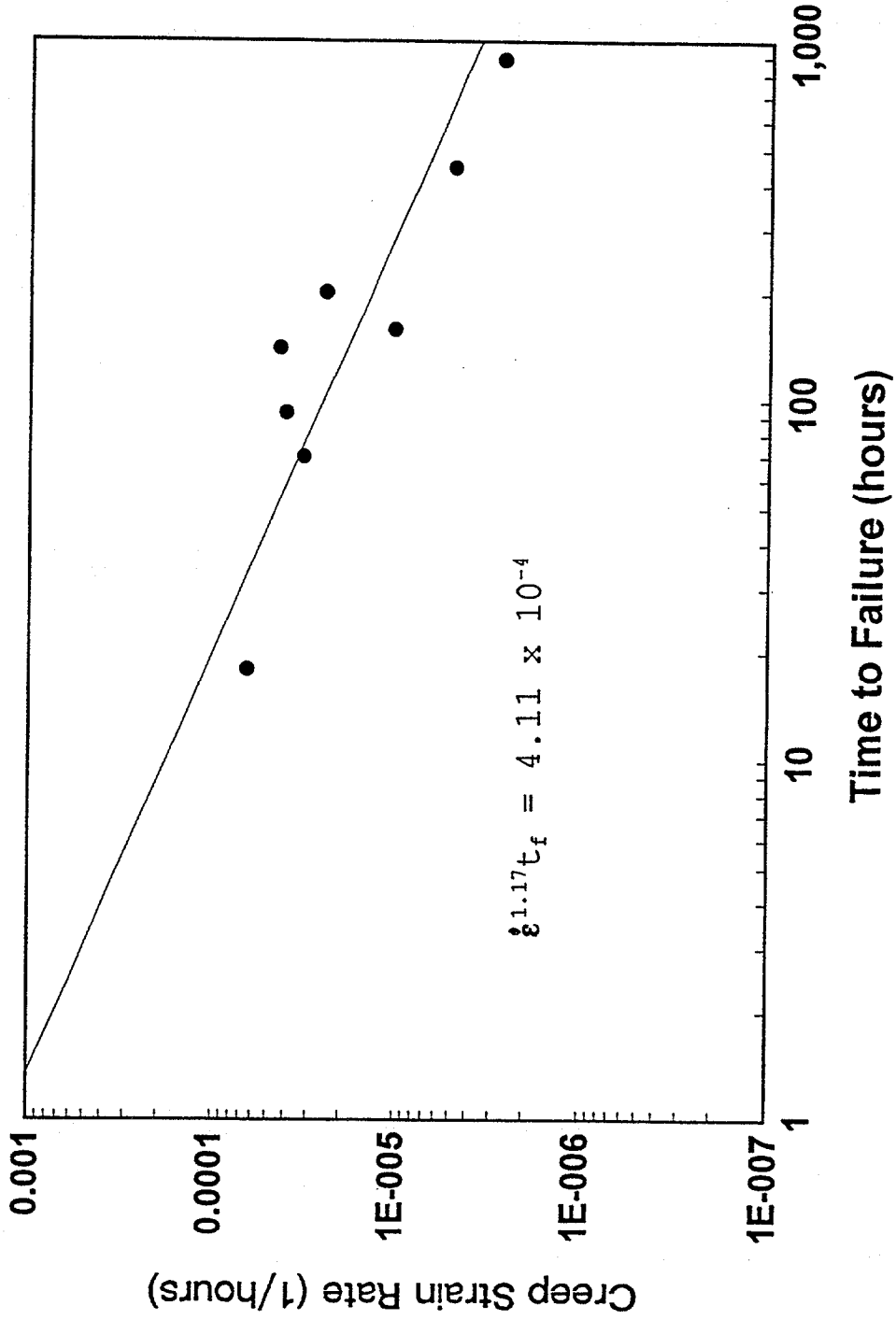


Figure 46: Monkman-Grant Relationship for Join or Gauge Failures



since the material constants were determined from tensile loading; (2) a fairly simple geometry; and (3) amenability to being tested experimentally. Guided by the above considerations, a notched, cylindrical tensile member was selected (Figure 47). The specimen has a semicircular notch at the center of the gauge section. The finite element mesh used in the analysis is represented in Figure 48. The figure shows one-half of an azimuthal section with the center line and notch apparent. An expanded view of the notch root mesh is given in the bottom view of the figure. The geometry was meshed with several different refinements to ensure that sufficient elements were used. The mesh shown in Figure 48 has 848, eight node, axisymmetric elements. A mesh convergence study using a mesh having 3984 elements verifies the results obtained with the coarser mesh. The model is loaded by applying a far field tensile stress to the top of the specimen and setting the temperature to 1370°C everywhere in the mesh. The far field stress corresponds to the loads from the experiments. This simulation was conducted assuming isothermal conditions, but that is not a necessary requirement. The load was applied, then the specimen was allowed to creep for up to 150 hours in 600 equal time increments to capture the nonlinear creep behavior. This was a much finer time division than required by the convergence criterion specified in ANSYS.

#### Experimental and Model Results

Three dogbone specimens with notched cylindrical gauge sections (Figure 47) were tested in creep at three different stress levels as described in Table 13. The specimen length is 3.5". The minimum and maximum diameters are 0.100" and 0.125" respectively. The experiments were carried out according to the procedures described in the Tensile Creep Test Methodology of section 7.1 in this report.

**Table 13: Silicon Nitride Notched Tensile Creep Summary**

| Specimen Number | Test Temperature (C) | Reduced Section Average Stress (MPa) | Failure Time (Hours) |
|-----------------|----------------------|--------------------------------------|----------------------|
| 1               | 1370                 | 120                                  | 44                   |
| 2               | 1370                 | 135                                  | 39                   |
| 3               | 1370                 | 150                                  | 3.5                  |

The results for an analysis which applies a far field tensile load such that the average stress across the notched section is 120 MPa (specimen #1), are presented for two different times. Immediately upon loading, the elastic solution gives the maximum stress in the root of the notch as 260 MPa. In Figure 49 the vertical normal stress,  $\sigma_y$ , is plotted at 10 hours and 100 hours of deformation. Note that at short times the vertical normal stress has its maximum at the notch root as would be expected from linear elastic analysis. As the creep deformation continues the creep strain builds up at the notch root and redistributes the stress more evenly across the section. It is shown that the stress is more uniform as the creep strain increases. The accumulated creep strain at 100 hours has its maximum at the notch root, as shown in Figure 50.

The failure was predicted for these experiments by obtaining the maximum vertical normal stress at the notch root during deformation as

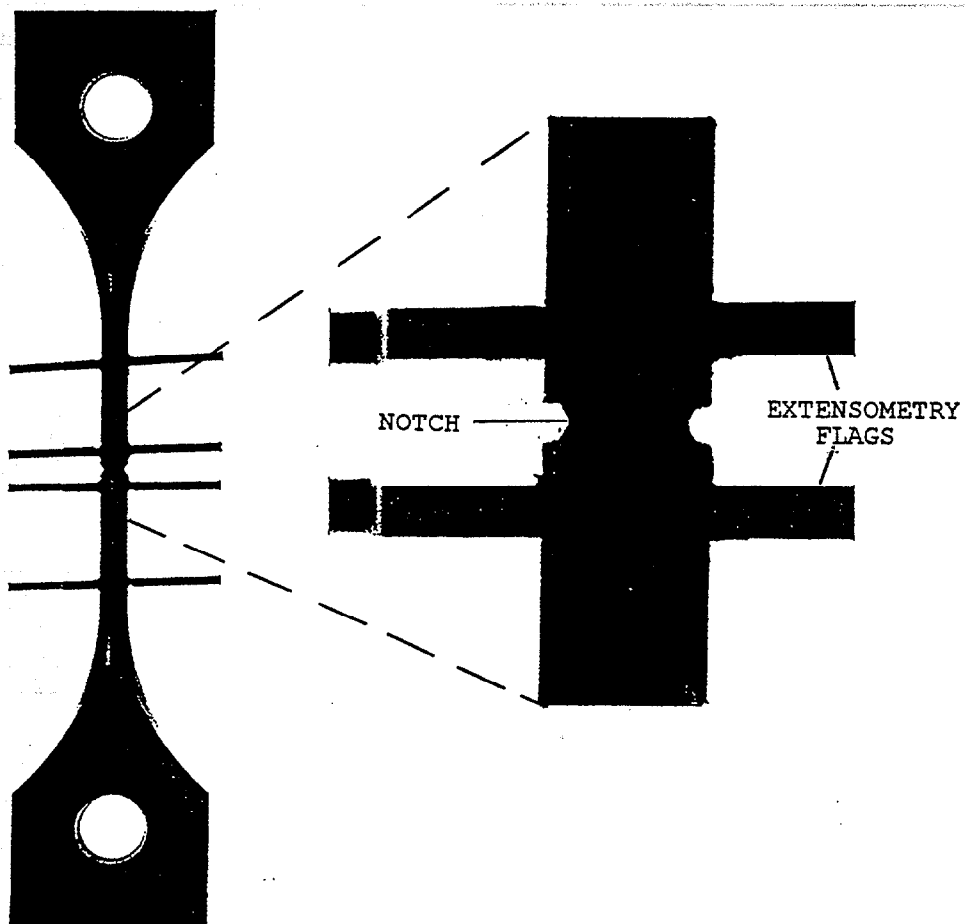


**Figure 47: Pinloaded, Notched Cylindrical Gauge Section Tensile Creep Specimen With Extensometry Flags**

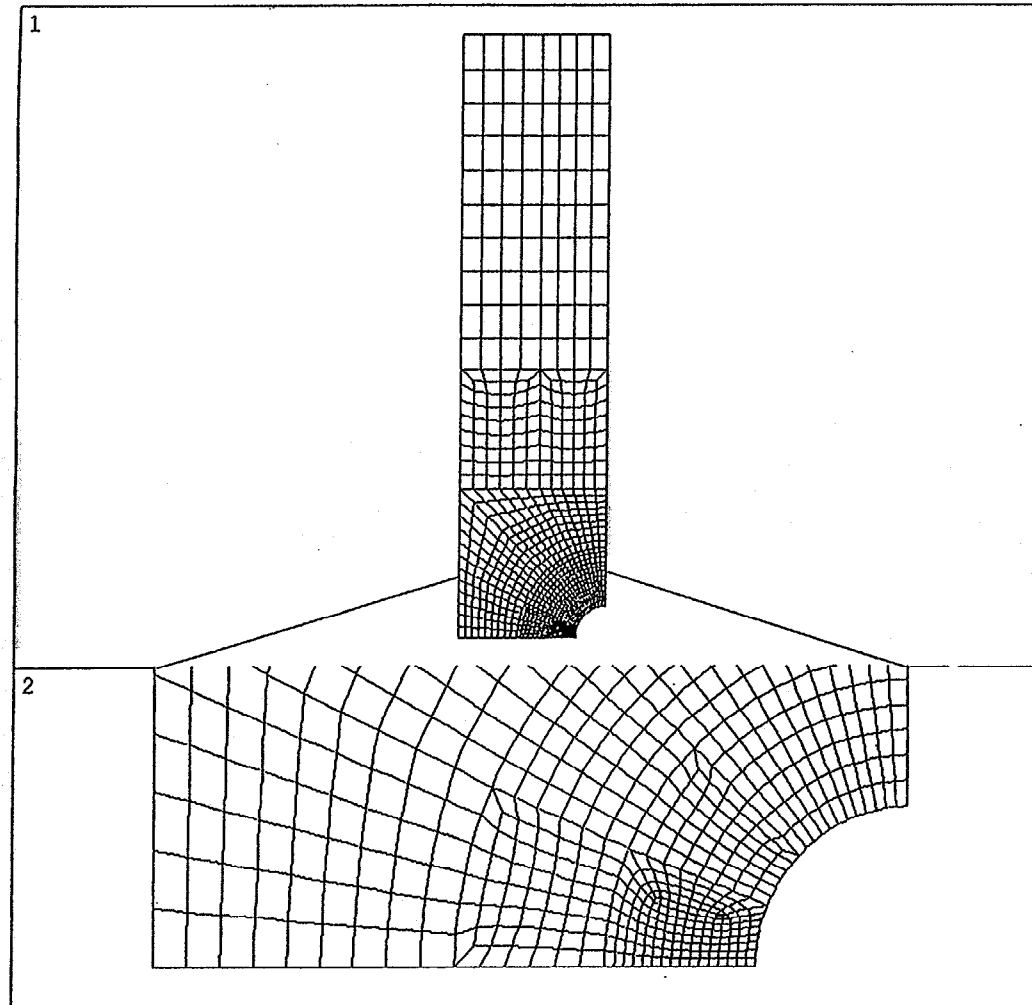
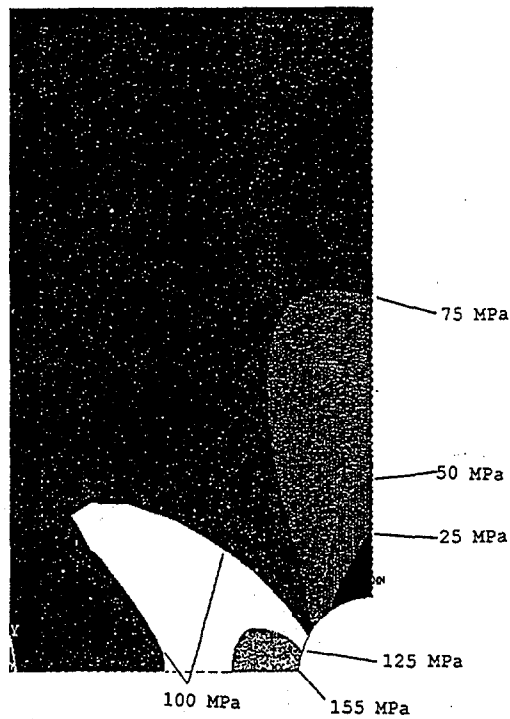
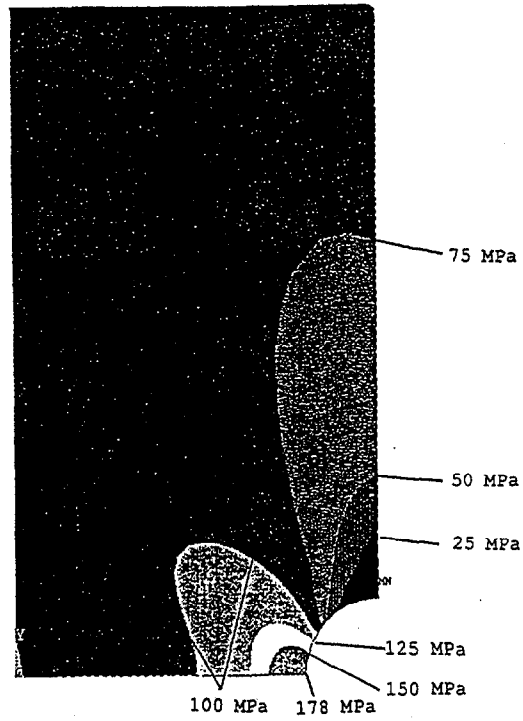
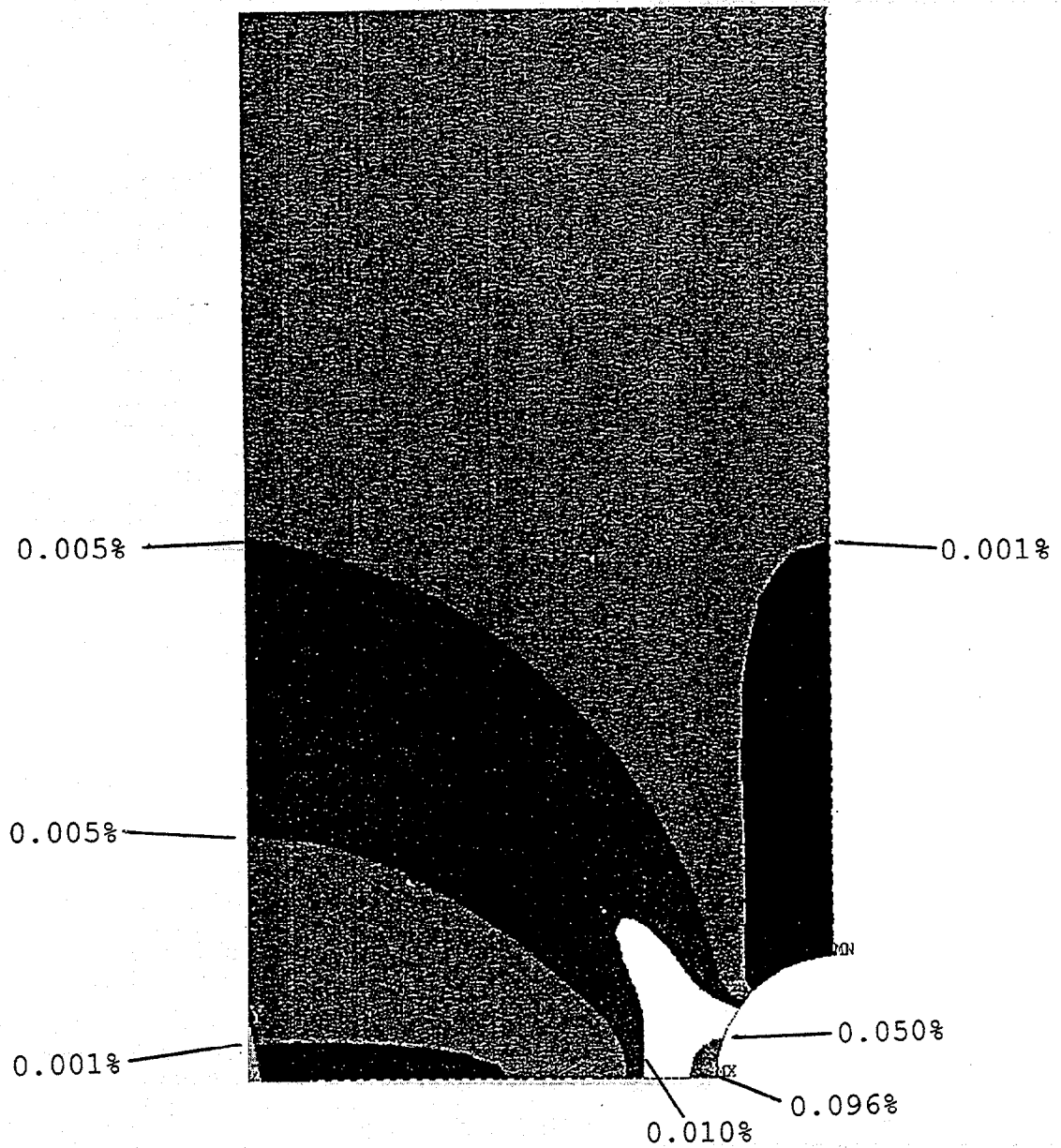


Figure 48: Notched Cylindrical Tensile Creep Specimen Finite Element Mesh



**Figure 49:** Distribution of Stress Component  $\sigma_{yy}$  Under 120 MPa Reduced Section Applied Stress at 1370°C



**Figure 50:** Distribution of Creep Strain  $\epsilon_{yy}$  in Notched Specimen After 100 Hours Under 120 MPa Reduced Section Applied Stress at 1370°C

a function of time from the finite element analysis. The corresponding creep strain rate (from Norton's equation) was then used to investigate whether the Monkman-Grant relationship, obtained from conventional creep measurement of silicon nitride butt joints (Section 9.1, was satisfied. The time variation of the notch root creep strain rate is plotted along with the Monkman-Grant curve, determined earlier in Section 9.2.2 based on gauge/join failures in the flat creep tensile specimens, in Figure 51 for the three specimens tested. Failure times for each of the three specimens are marked on their respective deformation paths. Notice that the failures of the notched tensile bars are predicted reasonably well using the Monkman-Grant relationship and are within the scatter of the original data points (Figure 46).

Considering the fact that Norton's law and thus the constitutive equation used in this analysis neglects primary creep, the agreement of the predictions with the test results are very good.

#### 9.2.4 Internal Variable Model

Having the minimum creep rate characterized is not sufficient as input for predicting the creep of structural components. The entire creep curve should be represented. The following approach was evaluated as an effective way to extend the minimum creep rate model (Equation 4) to the primary regime as well.

If we start with the assumption that the effect of stress and temperature on the minimum creep rate is representative of their effects on the entire creep curve then we can use an internal variable model which involves the dimensionless variable,  $s$ , and a material parameter,  $h$ . The change in structure will be represented by  $s$ , while  $h$ , is a measure of how quickly the material hardens. During creep,  $s$  evolves from its initial to final values. Here we will assume that we can normalize  $s$  such that its final value is unity. As  $s$  goes from  $s_0$  to 1 the creep rate will continuously decrease from its initial value until it reaches the temperature and stress dependent minimum value. This can be represented by the equations below.

$$\dot{\epsilon}_{cr} = \frac{A_s}{s} \sigma^{n_s} e^{-Q_s/RT} \quad (10)$$

$$\dot{s} = h(1-s) \dot{\epsilon}_{cr}. \quad (11)$$

Equations 10 and 11 represent a system of two, coupled first order differential equations that can be solved for  $\epsilon(t)$  to compare with experiments. The approach of using internal state variables is also being considered by Ding et. al.<sup>14</sup> for  $\text{Si}_3\text{N}_4$  and has been used extensively in metals<sup>18</sup> to capture nonlinear material behavior.

In order to evaluate this new model, the creep tests were used of nine NCX-5101 joins that were tested until failure. The minimum creep rate parameters  $A_s$ ,  $n_s$  and  $Q_s$  were determined from a least squares fit of the experimentally measured minimum creep rates. Using these values, the creep curves that were used in determining the parameters were simulated using Equations 10 and 11. The results are shown in Figure 52. The solid curves represent the experimental data and the dashed curves are the model predictions.

The results in Figure 52 show good agreement with the experiment. The shape and total strain are predicted reasonably well. In testing it

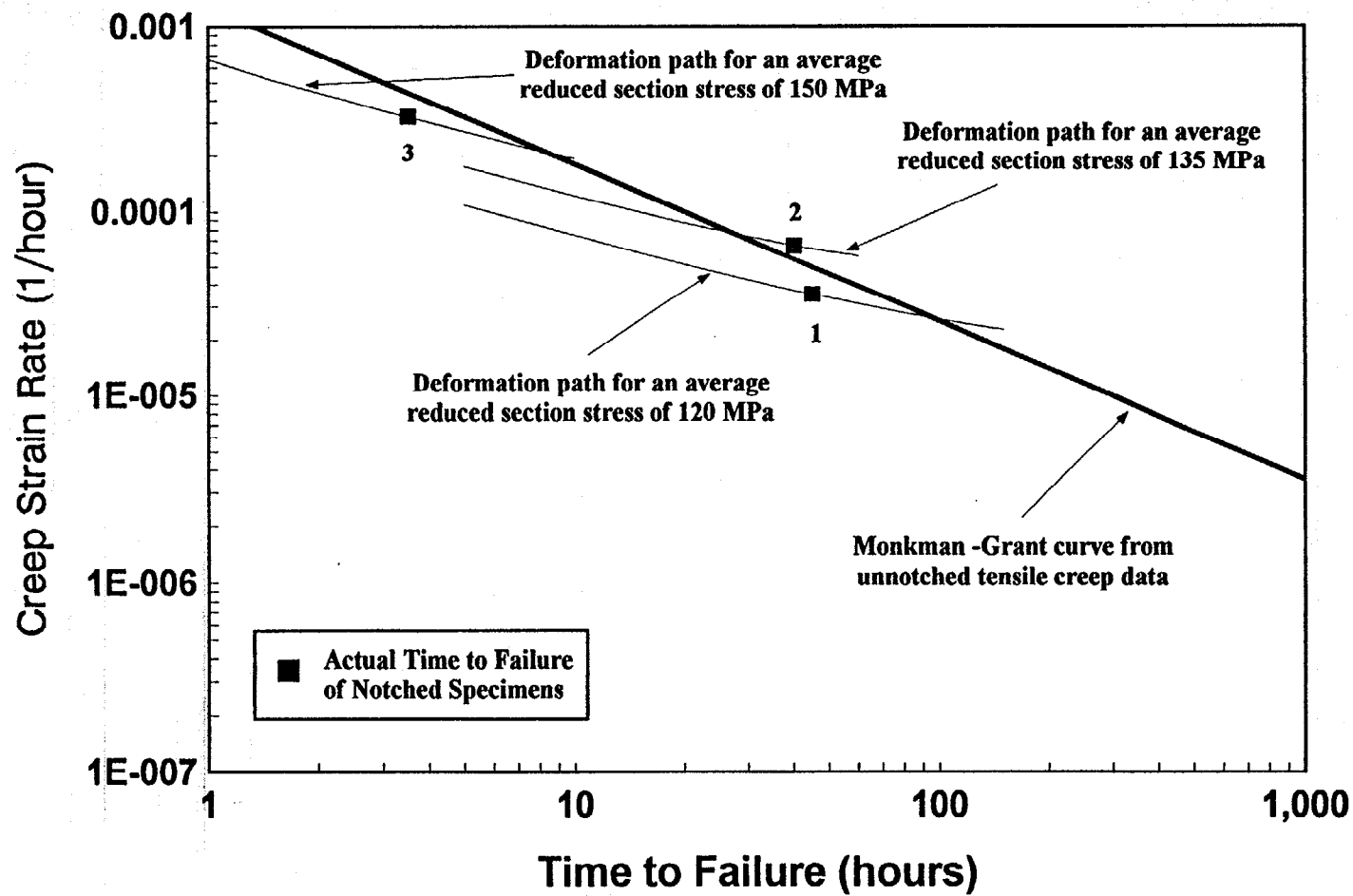


Figure 51: Failure Prediction of Cylindrical Gauge Notched Specimen Using the Monkman-Grant Relationship

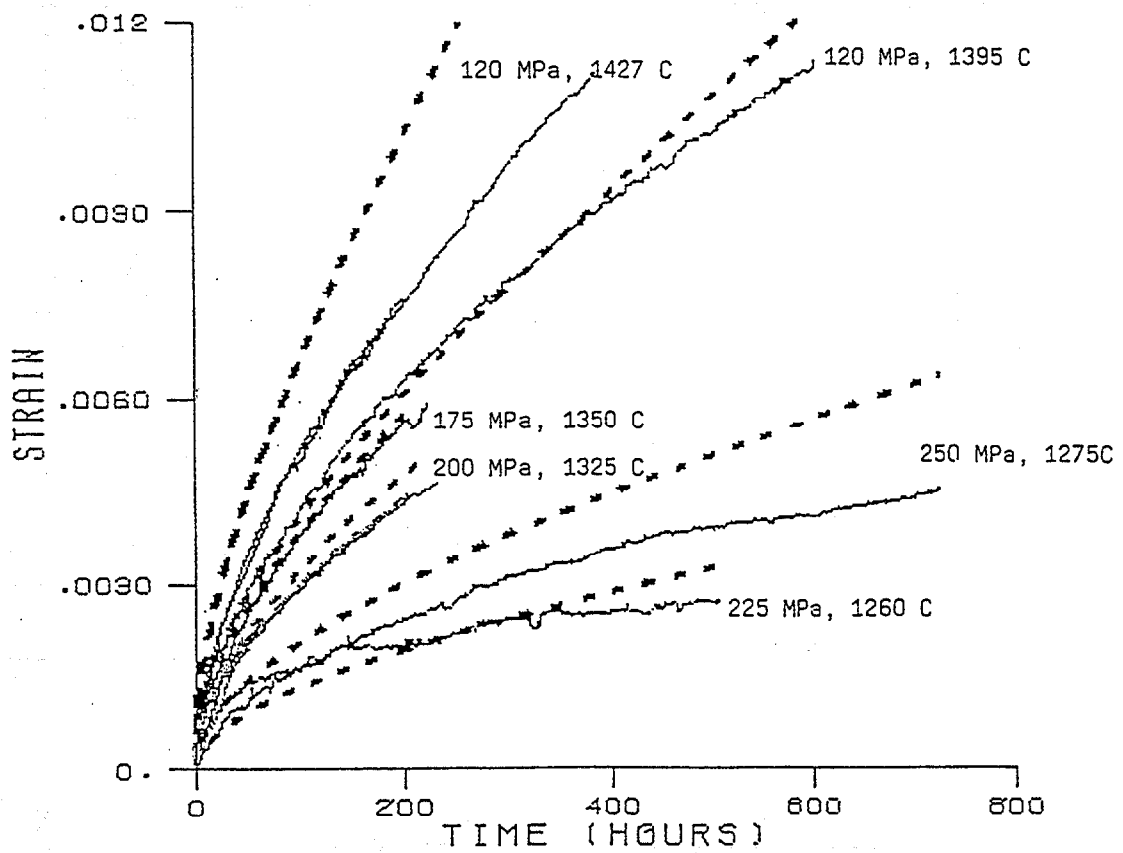


Figure 52: Comparison of Internal Variable Creep Model With Experiment for NCX-5101 Joined Specimens. Solid Curve is Experiment, Dashed Curve is Model.



was noticed that there is significant scatter in the measured creep response curves even for identical testing conditions. The model would not be able to capture this kind of experimental variability.

#### 9.2.5 Theta Projection Method

The approach of using Norton's equation to model the quasi-steady state creep has received the most attention in the literature but is by no means the only creep model available. An attempt has been made by Evans and Wilshire<sup>19, 20</sup> to develop equations which adequately describe the shape of typical creep curves and also quantify how such curves depend upon stress and temperature. The time dependent creep strain can be described as a function of various shape terms,  $\theta_i$ , which reproduce the creep curve at a specific stress and temperature:

$$\epsilon_{cr} = \epsilon_{cr}(t, \theta_1, \theta_2, \dots, \theta_n) \quad (12)$$

Different forms of Equation 12 have been used in the literature. The form which is used here can be understood as the sum of two terms. One term represents the decaying primary component and the other the accelerating tertiary component of creep strain, as follows:

$$\epsilon_{cr} = \theta_1(1 - e^{-\theta_2 t}) + \theta_3(e^{\theta_4 t} - 1) \quad (13)$$

Here  $\theta_1$  and  $\theta_3$  are strain like components representing the magnitude of primary and tertiary creep. The  $\theta_2$  and  $\theta_4$  are parameters describing the rate of the controlling processes. The form of Equation 13 describes the shape of a creep curve for ductile metals quite well, but might not be expected to work as well for ceramics that lack a pronounced tertiary region. One goal here is to investigate that correspondence. Maximum likelihood fits were used to calculate the  $\theta_i$ 's for each experimental creep curve which had the units of hours for time. Interpolation between testing conditions is provided by representing the dependence of each  $\theta_i$  on temperature and stress analytically:

$$\theta_i = \theta_i(T, \sigma) \quad (14)$$

The curve fit that was used is a simple exponential factor expansion in stress and temperature:

$$\ln \theta_i = A_i + B_i \sigma + C_i T + D_i \sigma T \quad (15)$$

for each  $\theta_i$ ,  $i=1, \dots, 4$ . This curve fit reduces the experimental data base to a total of 16 constants. Evans et. al.<sup>22</sup> applied this "theta projection" method to different pressureless sintered silicon nitride ceramics produced using MgO, CeO<sub>2</sub>, Y<sub>2</sub>O<sub>3</sub> additives. The method showed reasonable temperature interpolation capabilities for design calculations involving continuously varying stress and temperature conditions.

The  $\theta_i$ 's have been determined for each specimen using Equation 13. These values are used to determine the constants of Equation 15 and are listed in Table 14. Units of MPa for stress and degrees Kelvin for temperature were used when calculating these coefficients.

Table 14: Theta Projection Coefficients

|    | A       | B      | C          | D          |
|----|---------|--------|------------|------------|
| 01 | -20.406 | 0.102  | 9.523E-03  | -6.733E-05 |
| 02 | 43.095  | -0.468 | -3.034E-02 | 3.017E-04  |
| 03 | -14.222 | 0.156  | 9.776E-03  | -9.893E-05 |
| 04 | -10.022 | -0.340 | -4.534E-03 | 2.319E-04  |

A comparison of the fit with an experimental creep curve at 1395°C and 120 MPa is shown in Figure 53. The primary creep portion of the experimental curve is matched very well by the model. However, the model can be seen to diverge from the experimental curve to represent a tertiary component which is anticipated in the second term of equation 13. The divergence occurs at the inflection point corresponding to the minimum strain rate given by:

$$\frac{d\epsilon}{dt} = \theta_1 \theta_2 e^{-\theta_2 t_m} + \theta_3 \theta_4 e^{\theta_4 t_m} \quad (16)$$

where  $t_m$  is the time when the minimum creep rate occurs:

$$t_m = \frac{1}{\theta_2 + \theta_4} \ln \frac{\theta_1 \theta_2^2}{\theta_3 \theta_4^2} \quad (17)$$

This inflection point occurs at 367 hours for the conditions of 1395°C at 120 MPa depicted in Figure 54.

In view of the fact that tertiary creep was not observed in this test program, the four parameter form of equation 13 is not useful in representing response beyond the primary creep region. While it adequately models the primary creep region, our main interest has been in characterizing the secondary creep region. This is the focus of the Norton law modeling discussed in section 9.2.1. In that approach, the emphasis is on developing a mechanistic understanding of the creep process specifically during the secondary creep regime where most engineering components operate for the majority of their design life.

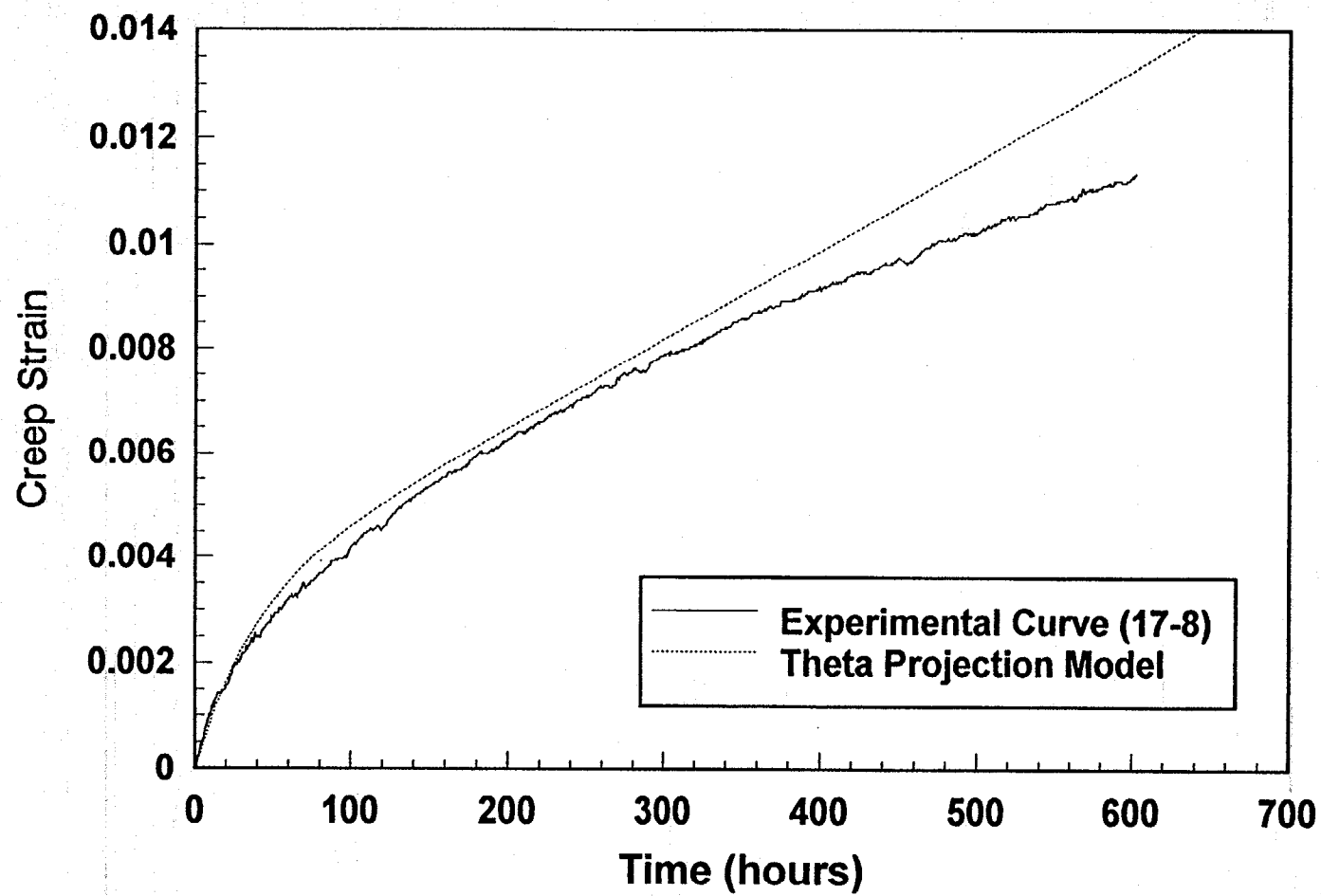


Figure 53: Theta Projection Versus Experimental Creep Curves at 1395°C and 120 MPa

## 10 CONCLUSIONS

The following conclusions may be drawn from the work performed under the Joining, Phase II contract.

Heat engine quality silicon nitride curved joins have been developed with similar properties to the planar butt joins developed under Joining, Phase I.

Green strength of the joining method was improved to minimize the handling rejections experienced before to hot isostatic pressing. Curved silicon nitride joins demonstrated a 5.5-fold improvement of pre-sintered green strength compared with methods used for Phase I of the contract.

Curved silicon nitride joins of 1.27 cm<sup>2</sup> area were developed with consistent, homogeneous properties across the join interlayer. There was no statistical difference between the 22°C and 1370°C flexure strength populations as a function of location within curved silicon nitride joins. The combined average 22°C flexure strength for curved silicon nitride joins was 886.3 MPa with a weibull modulus of 16.4 as determined by 156 flexure specimens from five curved join disks. The combined average 1370°C flexure strength for curved silicon nitride joins was 516 MPa with a weibull modulus of 16.0 as determined by 59 flexure specimens from five curved join disks. Only 1.2% of the 22°C flexure failures and 5.1% of the 1370°C flexure failures originated within the join interlayer. The excellent join integrity, characterized by the high strength of the join interlayer, prevented failure within the interlayer during shear tests of densified joins.

The demonstration of curved join quality similar to planar butt joins allowed application of the joining technique to more complex shapes, such as a simple rotor geometry. Shaft to disk joins made by the procedure developed for curved joins were ground to obtain spin test specimens.

Tensile strength of curved silicon nitride joins averaged 636 MPa with an estimated Weibull modulus of 8.2 with no failure originating from the join interlayer. The spin test specimens failed at angular velocities ranging between 17,000 and 42,530 revolutions per minute corresponding to a maximum principal stress from finite element analysis between 88.0 and 550.6 MPa. The angular velocity and stress at failure were less than predicted by the models developed within this contract due to failure origination at grinding damage. The size of surface flaws, determined by fractography, were consistent with the flaw size calculated from the Griffith relationship for brittle failure of solids. This result emphasizes the need for development of improved machining techniques for complex shaped structural ceramic components.

Tensile creep tests of the silicon nitride planar butt joins demonstrated behavior that was similar to the parent unjoined material. Creep was evaluated between temperature of 1250°C to 1420°C and stress between 100 and 250 MPa. Creep curves displayed a well defined primary creep regime with a gradual transition into secondary creep. None of the creep tests exhibited tertiary creep even though the duration of some tests were up to 1,692 hours. The largest variation of creep strain at test termination was observed within specimens as opposed to among specimens. The percent difference of total strain at test termination between opposing halves of the parent material typically ranged from 5% to 57%. This was attributed to inherent variable behavior of the ceramic parent material. Five of the 29 failures during tensile creep tests, originated within the join interlayer. Failed specimens exhibited cavitation at bi-grain junctions and wedge cracking at triple grain junctions. The creep data was incorporated into three models to develop a predictive tool that could be utilized for specimens of different geometry.

The widely accepted Norton's (or Arrhenius) equation approach was

initially considered to model creep behavior. Values of activation energy ( $Q$ ), stress exponent ( $n$ ) and material constant ( $A$ ) were determined for the creep experiments. An iterative procedure was used to determine a single estimate of these parameters for the entire creep matrix from which a good correlation of predicted and actual creep strain rate was obtained.

The above model used the minimum creep rate for a given experiment since this represented the creep rate at failure or test suspension within the secondary creep regime. Although this simplified the first attempt to model creep behavior, a more thorough treatment was later used where the entire creep curve, including the primary creep regime, was input in the model. The resultant internal variable model expressed the creep behavior by a system of two, coupled first order differential equations. Validation of the approach was obtained through comparison with the actual creep behavior of nine specimens that were tested to failure.

A less widely accepted, but interesting alternative to the Arrhenius equation approach, was considered to model the creep behavior. The theta projection method described time dependent creep strain with a series of shape terms to reproduce the creep strain curve at a specific stress and temperature. One term of the equation represented the decaying primary component and another an accelerating tertiary component of creep strain. The theta projection method deviated from classical creep modeling by defining the secondary creep regime mathematically as the resultant contribution of the tertiary and primary creep. Alternatively, the theta projection method provided a way not only to represent the experimental creep curves, but to interpolate to other testing conditions as well. However, the method did not satisfactorily fit all of the experimental data. The highly variable behavior within the primary creep regime experienced from specimen to specimen strongly contributed to an unacceptable error for predicted creep strain values. Additionally, the dependence of the theta projection model upon tertiary creep, which was not observed, invalidated use of this approach.

Creep failure modeling was facilitated by a correlation of creep strain rate with time to failure which allowed application of a Monkman-Grant relationship. It was unnecessary to plot separate curves for each temperature since a good correlation of all the experimental data was obtained with a single curve.

The development of material models, above, was useful only if the model could predict the performance of structural components. The refined models developed above were used to predict the behavior of a notched tensile specimen that served to simulate behavior of an actual component. Reasonable prediction of the time of failure for three specimens tested under different loads was an encouraging demonstration of the value of the use of ANSYS finite element code in conjunction with the Norton's law model.

NT230 silicon carbide joining of planar butt joints resulted with join quality affected by pronounced silicon enrichment and porosity. Additional trials used a total of six interlayer types consisting of various mixtures of silicon carbide and other additives applied to both siliconized and unsiliconized parent materials. Quality of the silicon carbide joins evaluated by room temperature flexure strength tests of specimens ground from the joined bodies showed all flexure specimens failed at the join interlayer. Join strength was lower than the strength of unjoined NT230 of similar cross sectional thickness, with average strengths of 152 MPa and 233 MPa respectively. Although, the joins were structurally sound and exhibited a improved, more homogeneous distribution of silicon carbide and silicon, all of the joins lacked a contiguous network of silicon carbide that extended into the parent material. All of the join methods resulted in join interlayers that were discrete relative to the parent materials and of higher silicon concentration. The distinct interface between the join interlayer and

parent material consisted primarily of silicon within the join and silicon carbide within the parent material with an absence of interpenetration across the interface. In addition, voids within the join interlayer were strength limiting.

The silicon carbide join quality was deemed unsatisfactory for more demanding structural applications and, therefore, the decision was made not to proceed to more complex, curved geometries. The silicon carbide joining methods covered within this contract, although not entirely successful, have emphasized the need to focus future efforts upon ways to obtain a homogeneous, well sintered parent/join interface prior to siliconization. Improved definition of the silicon carbide joining problem obtained by efforts during this contract have provided avenues for future work that should successfully obtain heat engine quality joins.

## 11 ACKNOWLEDGEMENTS

The authors gratefully acknowledge the support of the Ceramic Technology Project, DOE Office of Transportation Technologies. We give special thanks for the guidance given by Mike Santella, Program Manager of Joining, at ORNL.

The authors wish to acknowledge the contributions of the following individuals for their steadfast support during this effort: D. Collette, R. D. Creehan, G. E. Lambert, M. J. Mangaudis, R. T. Rawson, T. M. Trostel, F. J. Wu, L. A. Broderick.

Special recognition is given to L. D. Ton for the manufacture of all joins, coordination of: furnacing, grinding and countless other tasks within the project.

Thanks to D. M. Tracey and R. H. Licht for editorial assistance.

The patience and perseverance of J. G. Gillam with secretarial efforts was invaluable.

The contribution of Norton Advanced Ceramics Division to the manufacture of parent materials is greatly appreciated.

## 12 REFERENCES

1. M. R. Foley, G. A. Rossi, G. J. Sundberg, J. A. Wade, F. J. Wu, *Analytical and Experimental Evaluation of Joining Silicon Carbide to Silicon Carbide and Silicon Nitride For Advanced Heat Engine Applications, Final Report, Subcontract 86X-SB045C*, Norton Company, September 30, 1991, 44.
2. M. G. Jenkins, M. K. Ferber, et. al., *Study and Analysis of the Stress State in a Ceramic, Button-Head, Tensile Specimen*, ORNL TM-11767, September 1991.
3. Z-Mike Division of LaserMike Inc. (Formerly a Division of Zygo Corp.), Middlefield, CT, 06455-0448.
4. RS/1 is a trademark of BBN Software Products, 10 Fawcett Street, Cambridge, MA 02138.
5. T. R. Wilshaw, "Measurement of Tensile Strength of Ceramics," *Journal of The American Ceramic Society*, February 1968, page 111.
6. Swanson Analysis Systems, Inc., ANSYS Rev. 4.4 and 5.0 Engineering Analysis System.
7. L. M. Powers, A. Starlinger, and J. P. Gyekenyesi, "Ceramic Component Reliability With the Restructured NASA/Cares Computer Program," NASA Technical Memorandum 105856, 1992.
8. J. S. Cuccio, "Life Prediction Methods for Ceramic Components of Advanced Vehicular Heat Engines," presented at ATDCCM, Dearborn, MI, October 18-21, 1993.
9. D. M. Tracey, "3D Elastic Singularity Element for Evaluation of K Along an Arbitrary Crack Front," *Int'l J. Fracture*, 9, pp.340-343, 1973.
10. H. E. Evans, "Mechanisms of Creep Failure" Elsevier Applied Science Publishers LTD., NY, 1984.
11. F. A. McClintock and A. S. Argon, *Mechanical Behavior of Materials*, Addison-Wesley Publishing Comp., Inc. (1966).
12. D. Chakraborty and A. K. Mukhopadhyay, "Creep of Sintered Silicon Nitride," *Ceramics International* 15 (1989), 237-245.
13. F. H. Norton, "The Creep of Steel at High Temperatures," McGraw-Hill, (1929).
14. J. L. Ding, K. C. Liu, and C. R. Brinkman, "Development of a Constitutive Model for Creep and Life Prediction of Advanced Silicon Nitride Ceramics," *Proceedings of the Annual Automotive Technology Development Contractors' Meeting*, Dearborn, Michigan, Nov. 2-4, 1992, SAE, 583-592.
15. S. M. Wiederhorn, R. Krause and D. C. Cranmer, "Tensile Creep Testing of Structural Ceramics," *Proceedings of the Annual Automotive Technology Development Contractors' Meeting*, Dearborn, Michigan, Oct. 28-31, 1991, SAE, 273-280.
16. Internal Saint-Gobain communication with R. L. Yeckley, 1993.



17. F. C. Monkman and N. J. Grant, "An empirical Relationship Between Rupture Life and Minimum Creep Rate in Creep-Rupture Tests," *Proc. Soc. Test. Mater.* **56**, pp. 593-620 (1956).
18. S. B. Brown, K. H. Kim, and L. Anand, *An Internal Variable Constitutive Model for Hot Working of Metals*, *International Journal of Plasticity*, **Vol. 5**, pp. 95-13 (1985).
19. R. W. Evans, and B. Wilshire, *Creep of Metals and Alloys*, *The Institute of Metals*, London, 1985.
20. B. Wilshire and R. W. Evans, *Creep Behavior of Crystalline Solids*, *Progress in Creep and Fracture*, **Vol. 3**, Pineridge Press, Swansea, U.K., 1985.
21. R. W. Evans, T. Murakami, and B. Wilshire, "The Generation of Long-Term Creep Data for Silicon Nitride Ceramics," *British Ceramics Proceedings*, **No. 39**, December 1987.



## INTERNAL DISTRIBUTION

Central Research Library (2)  
Document Reference Section  
Laboratory Records Department (2)  
Laboratory Records, ORNL RC  
ORNL Patent Section  
M&C Records Office (3)  
L. F. Allard, Jr.  
L. D. Armstrong  
D. L. Balltrip  
R. L. Beatty  
P. F. Becher  
T. M. Besmann  
P. J. Blau  
E. E. Bloom  
K. W. Boling  
R. A. Bradley  
C. R. Brinkman  
V. R. Bullington  
R. S. Carlsmith  
P. T. Carlson  
G. M. Caton  
S. J. Chang  
D. D. Conger  
R. H. Cooper, Jr.  
S. A. David  
J. H. DeVan  
J. L. Ding  
M. K. Ferber  
W. Fulkerson  
R. L. Graves  
D. L. Greene  
H. W. Hayden, Jr.  
E. E. Hoffman  
C. R. Hubbard

M. A. Janney  
D. R. Johnson (5)  
F. W. Jones  
R. R. Judkins  
M. A. Karnitz  
B. L. Keyes  
H. D. Kimrey, Jr.  
T. G. Kollie  
K. C. Liu  
E. L. Long, Jr.  
W. D. Manly  
R. W. McClung  
D. J. McGuire  
J. R. Merriman  
T. A. Nolan  
A. E. Pasto  
M. H. Rawlins  
J. L. Rich  
C. R. Richmond  
J. M. Robbins  
G. V. Rogers, Jr.  
M. L. Santella  
A. C. Schaffhauser  
S. Scott  
E. J. Soderstrom  
D. P. Stinton  
R. W. Swindeman  
M. C. Tate  
V. J. Tennery  
T. N. Tiegs  
J. R. Weir, Jr.  
B. H. West  
S. G. Winslow  
J. M. Wyrick  
C. S. Yust

## EXTERNAL DISTRIBUTION

Pioneering Research Info. Ctr.  
E.I. Dupont de Nemours & Co. Inc.  
Experimental Station  
P.O. Box 80302  
Wilmington DE 19880-0302

Jeffrey Abboud  
U.S. Advanced Ceramics Assoc.  
1600 Wilson Blvd., Suite 1008  
Arlington VA 22209

James H. Adair  
University of Florida  
Materials Science & Engineering  
317 MAE Bldg.  
Gainesville FL 32611-2066

Donald F. Adams  
University of Wyoming  
Mechanical Engineering Department  
P.O. Box 3295  
Laramie WY 82071

Jalees Ahmad  
AdTech Systems Research Inc.  
Solid Mechanics  
1342 N. Fairfield Road  
Dayton OH 45432-2698

Yoshio Akimune  
NISSAN Motor Co., Ltd.  
Materials Research Laboratory  
1 Natsushima-Cho  
Yokosuka 237  
JAPAN

Mufit Akinc  
Iowa State University  
322 Spedding Hall  
Ames IA 50011

Ilhan A. Aksay  
Princeton University  
A313 Engineering Quadrangle  
Princeton NJ 08544-5263

Richard L. Allor  
Ford Motor Company  
Materials Systems Reliability  
P.O. Box 2053, Room S-2031  
Dearborn MI 48121-2053

Joseph E. Amaral  
Instron Corporation  
Corporate Engineering Office  
100 Royale Street  
Canton MA 02021

Edward M. Anderson  
Aluminum Company of America  
N. American Industrial Chemical  
P.O. Box 300  
Bauxite AR 72011

Norman C. Anderson  
Ceradyne, Inc.  
Ceramic-to-Metal Division  
3169 Redhill Avenue  
Costa Mesa CA 92626

Don Anson  
BCL  
Thermal Power Systems  
505 King Avenue  
Columbus OH 43201-2693

Thomas Arbanas  
G.B.C. Materials Corporation  
580 Monastery Drive  
Latrobe PA 15650-2698

Frank Armatis  
3M Company  
Building 60-1N-01  
St. Paul MN 55144-1000

Everett B. Arnold  
Detroit Diesel Corporation  
Mechanical Systems Technology  
13400 Outer Drive West  
Detroit MI 48239-4001

Bertil Aronsson  
Sandvik AB  
S-12680  
Stockholm Lerkrogsvagen 19  
SWEDEN

Dennis Assanis  
University of Illinois  
Dept. of Mechanical Engineering  
1206 W. Green Street  
Urbana IL 61801

V. S. Avva  
North Carolina A&T State Univ.  
Dept. of Mechanical Engineering  
Greensboro NC 27411

Patrick Badgley  
Sky Technologies, Inc.  
2815 Franklin Drive  
Columbus IN 47201

Sunggi Baik  
Pohang Institute of Sci. & Tech.  
P.O. Box 125  
Pohang 790-600  
KOREA

John M. Bailey  
Consultant  
Caterpillar, Inc.  
P.O. Box 1875  
Peoria IL 61656-1875

Bob Baker  
Ceradyne, Inc.  
3169 Redhill Avenue  
Costa Mesa CA 92626

Frank Baker  
Aluminum Company of America  
Alcoa Technical Center  
Alcoa Center PA 15069

Clifford P. Ballard  
AlliedSignal Aerospace Company  
Ceramics Program  
P.O. Box 1021  
Morristown NJ 07962-1021

B. P. Bandyopadhyay  
ELID Team  
Wako Campus  
2-1 Hirosawa Wako-shi  
Saitama 351-01  
JAPAN

P. M. Barnard  
Ruston Gas Turbines Limited  
P.O. Box 1  
Lincoln LN2 5DJ  
ENGLAND

Harold N. Barr  
Hittman Corporation  
9190 Red Branch Road  
Columbia MD 21045

Renald D. Bartoe  
Vesuvius McDanel  
510 Ninth Avenue  
Box 560  
Beaver Falls PA 15010-0560

David L. Baty  
Babcock & Wilcox - LRC  
P.O. Box 11165  
Lynchburg VA 24506-1165

Donald F. Baxter, Jr.  
ASM International  
Advanced Materials & Processes  
Materials Park OH 44073-0002

M. Brad Beardsley  
Caterpillar Inc.  
Technical Center Bldg. E  
P.O. Box 1875  
Peoria IL 61656-1875

John C. Bell  
Shell Research Limited  
Thornton Research Centre  
P.O. Box 1  
Chester CH1 3SH  
ENGLAND

M. Bentele  
Xamag, Inc.  
259 Melville Avenue  
Fairfield CT 06430

Larry D. Bentsen  
BFGoodrich Company  
R&D Center  
9921 Brecksville Road  
Brecksville OH 44141

Louis Beregszazi  
Defiance Precision Products  
P.O. Drawer 428  
Defiance OH 43512

Tom Bernecki  
Northwestern University  
1801 Maple Avenue  
Evanston IL 60201-3135

Charles F. Bersch  
Institute for Defense Analyses  
1801 N. Beauregard Street  
Alexandria VA 22311

Ram Bhatt  
NASA Lewis Research Center  
21000 Brookpark Road  
Cleveland OH 44135

Deane I. Biehler  
Caterpillar Inc.  
Engineering Research Materials  
P.O. Box 1875, Bldg. E  
Peoria IL 61656-1875

John W. Bjerklie  
Consolidated Natural Gas Service  
Co. Inc.  
Research Department  
Pittsburgh PA 15222-3199

William D. Bjorndahl  
TRW, Inc.  
One Space Park, MS:R6-2188  
Building 01, Room 2040  
Redondo Beach CA 90278

Keith A. Blakely  
Advanced Refractory Technologies,  
Inc.  
699 Hertel Avenue  
Buffalo NY 14207

Edward G. Blanchard  
Netzsch Inc.  
119 Pickering Way  
Exton PA 19341

Bruce Boardman  
Deere and Company Technical Ctr.  
3300 River Drive  
Moline IL 61265

Hoechst Celanese Corporation  
Short Hills NJ 07078

Russell Bockstedt  
Hoechst Celanese Corporation  
150 JFK Parkway  
Short Hills NJ 07078

M. Boehmer  
DLR German Aerospace Research  
Etab.  
Postfach 90 60 58  
D-5000 Koln 90  
GERMANY

Lawrence P. Boesch  
EER Systems Corp.  
1593 Spring Hill Road  
Vienna VA 22182-2239

Donald H. Boone  
Boone & Associates  
2412 Cascade Drive  
Walnut Creek CA 94598-4313

Tom Booth  
AlliedSignal, Inc.  
AiResearch Los Angeles Division  
2525 West 190th Street  
Torrance CA 90509-2960

Tibor Bornemisza  
Sundstrand Power Systems  
4400 Ruffin Road  
San Diego CA 92186-5757

J.A.M. Boulet  
University of Tennessee  
Engineering Science and Mechanics  
Knoxville TN 37996-2030

H. Kent Bowen  
Massachusetts Institute of  
Technology  
77 Massachusetts Ave., Rm E40-434  
Cambridge MA 02139

Leslie J. Bowen  
Materials Systems  
53 Hillcrest Road  
Concord MA 01742

Steven C. Boyce  
Air Force Office of Scientific  
Research  
AFOSR/NA Bldg. 410  
Bolling AFB DC 20332-6448

Gary L. Boyd  
Ceramic Engineering Consulting  
328 Sneath Way  
Alpine CA 91901

Steve Bradley  
UOP Research Center  
50 E. Algonquin Road  
Des Plaines IL 60017-6187

Michael C. Brands  
Cummins Engine Company, Inc.  
P.O. Box 3005, Mail Code 50179  
Columbus IN 47201

Raymond J. Bratton  
Westinghouse Science & Technology  
1310 Beulah Road  
Pittsburgh PA 15235

John J. Brennan  
United Technologies Corporation  
Silver Lane, MS:24  
East Hartford CT 06108

Terrence K. Brog  
Golden Technologies Company  
4545 McIntyre Street  
Golden CO 80403

Gunnar Broman  
317 Fairlane Drive  
Spartanburg SC 29302

Al Brown  
High-Tech Materials Alert  
P.O. Box 882  
Dayton NJ 08810

Jesse J. Brown  
VPI & SU  
Ctr. for Advanced Ceram Materials  
Blacksburg VA 24061-0256

Sherman D. Brown  
University of Illinois  
Materials Science and Engineering  
105 South Goodwin Avenue  
Urbana IL 61801

S. L. Bruner  
Ceramatec, Inc.  
2425 South 900 West  
Salt Lake City UT 84119

Walter Bryzik  
U.S. Army Tank Automotive Command  
R&D Center, Propulsion Systems  
Warren MI 48397-5000

S. J. Burden  
2572 Devonwood  
Troy MI 48098

Curt V. Burkland  
AMERCOM, Inc.  
8928 Fullbright Avenue  
Chatsworth CA 91311

Bill Bustamante  
AMERCOM, Inc.  
8928 Fullbright Avenue  
Chatsworth CA 91311

Oral Buyukozturk  
Massachusetts Institute of  
Technology  
77 Massachusetts Ave., Room 1-280  
Cambridge MA 02139

David A. Caillet  
Ethyl Corporation  
451 Florida Street  
Baton Rouge La 70801

Frederick J. Calnan  
Heany Industries, Inc.  
249 Briarwood Lane  
Scottsville NY 14546

Roger Cannon  
Rutgers University  
P.O. Box 909  
Piscataway NJ 08855-0909

Scott Cannon  
P.O. Box 567254  
Atlanta GA 30356

Harry W. Carpenter  
1844 Fuerte Street  
Fallbrook CA 92028

David Carruthers  
Kyocera Industrial Ceramics  
Company  
P.O. Box 2279  
Vancouver WA 98668-2279

Calvin H. Carter, Jr.  
Cree Research, Inc.  
2810 Meridian Parkway  
Durham NC 27713

J. David Casey  
35 Atlantis Street  
West Roxbury MA 02132

Jere G. Castor  
J. C. Enterprise  
5078 N. 83rd Street  
Scottsdale AZ 85250

James D. Cawley  
Case Western Reserve University  
Materials Science & Engineering  
Cleveland OH 44106

Thomas C. Chadwick  
Den-Mat Corporation  
P.O. Box 1729  
Santa Maria CA 93456

Ronald H. Chand  
Chand Kare Technical Ceramics  
2 Coppage Drive  
Worcester MA 01603-1252

Robert E. Chaney  
EG&G Idaho, Inc.  
Idaho National Engineering Lab  
P.O. Box 1625  
Idaho Falls ID 83415-3525

Frank C. Chang  
U.S. Army Materials Technology  
AMTL-EMM  
405 Arsenal Street  
Watertown MA 02172

Nam S. Chang  
Chrysler Corporation  
12000 Chrysler Drive  
Highland Park MI 48288-0001

William Chapman  
Williams International Corp.  
2280 W. Maple Road  
Walled Lake MI 48390-0200

Ching-Fong Chen  
LECO Corporation  
3000 Lakeview Avenue  
St. Joseph MI 49085

Frank Childs  
EG&G Idaho, Inc.  
Idaho National Engineering Lab  
P.O. Box 1625  
Idaho Falls ID 83415-3527

William J. Chmura  
Torrington Company  
59 Field Street  
Torrington CT 06790-4942

Tsu-Wei Chou  
University of Delaware  
201 Spencer Laboratory  
Newark DE 19716

R. J. Christopher  
Ricardo Consulting Engineers  
Bridge Works  
Shoreham-By-Sea W. Sussex BN435FG  
ENGLAND

Joel P. Clark  
Massachusetts Institute of  
Technology  
Room 8-409  
Cambridge MA 02139



Giorgio Clarotti  
Commission of the European Comm  
DGXII-C3, M075, 1-53;  
200 Rue de la Loi  
B-1049 Brussels  
BELGIUM

W. J. Clegg  
ICI Advanced Materials  
P.O. Box 11, The Heath  
Runcorn Cheshire WA7 4QE  
ENGLAND

Joseph Cleveland  
GTE Products Corporation  
Hawes Street  
Towanda PA 18848-0504

William S. Coblenz  
Adv. Research Projects Agency  
3701 N. Fairfax Drive  
Arlington VA 22203

Gloria M. Collins  
ASTM  
1916 Race Street  
Philadelphia PA 19103

William C. Connors  
Sundstrand Aviation Operations  
Materials Science & Engineering  
4747 Harrison Avenue  
Rockford IL 61125-7002

John A. Coppola  
Carborundum Company  
Niagara Falls R&D Center  
P.O. Box 832  
Niagara Falls NY 14302

Normand D. Corbin  
Norton Company  
SGNICC/NRDC  
Goddard Road  
Northboro MA 01532-1545

Douglas Corey  
AlliedSignal, Inc.  
2525 West 190th Street, MS:T52  
Torrance CA 90504-6099

Keith P. Costello  
Chand/Kare Technical Ceramics  
2 Coppage Drive  
Worcester MA 01603-1252

Ed L. Courtright  
Pacific Northwest Laboratory  
MS:K3-59  
Richland WA 99352

Anna Cox  
Mitchell Market Reports  
P.O. Box 23  
Monmouth Gwent NP5 4YG  
UNITED KINGDOM

J. Wesley Cox  
BIRL  
1801 Maple Avenue  
Evanston IL 60201-3135

Art Cozens  
Instron Corporation  
3414 Snowden Avenue  
Long Beach CA 90808

Mark Crawford  
New Technology Week  
4604 Monterey Drive  
Annandale VA 22003

Richard A. Cree  
Markets & Products, Inc.  
P.O. Box 14328  
Columbus OH 43214-0328

Les Crittenden  
Vesuvius McDanel  
Box 560  
Beaver Falls PA 15010

William J. Croft  
U.S. Army Materials Technology  
405 Arsenal Street  
Watertown MA 02172

M. J. Cronin  
Mechanical Technology, Inc.  
968 Albany-Shaker Road  
Latham NY 12110

Gary M. Crosbie  
Ford Motor Company  
20000 Rotunda Drive  
MD-2313, SRL Building  
Dearborn MI 48121-2053

Floyd W. Crouse, Jr.  
U.S. Department of Energy  
Morgantown Energy Technology Ctr  
P.O. Box 880  
Morgantown WV 26505

John Cuccio  
AlliedSignal Engines  
P.O. Box 52180, MS:1302-2Q  
Phoenix AZ 85072-2180

Raymond A. Cutler  
Ceramatec, Inc.  
2425 South 900 West  
Salt Lake City UT 84119

Stephen C. Danforth  
Rutgers University  
P.O. Box 909  
Piscataway NJ 08855-0909

Sankar Das Gupta  
Electrofuel Manufacturing Co.  
9 Hanna Avenue  
Toronto Ontario MGK-1W8  
CANADA

Frank Davis  
AlliedSignal Aerospace Company  
7550 Lucerne Drive, #203  
Middleburg Heights OH 44130

Robert F. Davis  
North Carolina State University  
Materials Engineering Department  
P.O. Box 7907  
Raleigh NC 27695

Thomas DeAngelis  
Carborundum Company  
Niagara Falls R&D Center  
P.O. Box 832  
Niagara Falls NY 14302

Michael DeLuca  
RSA Research Group  
1534 Claas Ave.  
Holbrook NY 11741

Gerald L. DePoorter  
Colorado School of Mines  
Metallurgical & Materials Engr  
Golden CO 80401

J. F. DeRidder  
Omni Electro Motive, Inc.  
12 Seely Hill Road  
Newfield NY 14867

Nick C. Dellow  
Materials Technology Publications  
40 Sotheron Road  
Watford Herts WD1 2QA  
UNITED KINGDOM

L. R. Dharani  
University of Missouri-Rolla  
224 M.E.  
Rolla MO 65401

Douglas A. Dickerson  
Union Carbide Specialty Powders  
1555 Main Street  
Indianapolis IN 46224

John Dodsworth  
Vesuvius Research & Development  
Technical Ceramics Group  
Box 560  
Beaver Falls PA 15010

B. Dogan  
Institut fur Werkstofforschung  
GKSS-Forschungszentrum Geesthacht  
Max-Planck-Strasse  
D-2054 Geesthacht  
GERMANY

Alan Dragoo  
U.S. Department of Energy  
ER-131, MS:F-240  
Washington DC 20817

Jean-Marie Drapier  
 FN Moteurs S.A.  
 Material and Processing  
 B-4041 Milmort (Herstal)  
 BELGIUM

Kenneth C. Dreitlein  
 United Technologies Research Ctr  
 Silver Lane  
 East Hartford CT 06108

Robin A.L. Drew  
 McGill University  
 3450 University Street  
 Montreal Quebec H3A 2A7  
 CANADA

Winston H. Duckworth  
 BCL  
 Columbus Division  
 505 King Avenue  
 Columbus OH 43201-2693

Bill Durako  
 Sundstrand Aviation Operations  
 P.O. Box 7002  
 Rockford IL 61125-7002

Ernest J. Duwell  
 3M Abrasive Systems Division  
 3M Center  
 St. Paul MN 55144-1000

Chuck J. Dziedzic  
 GTC Process Forming Systems  
 4545 McIntyre Street  
 Golden CO 80403

Robert J. Eagan  
 Sandia National Laboratories  
 Engineered Materials & Processes  
 P.O. Box 5800  
 Albuquerque NM 87185-5800

Jeffrey Eagleson  
 Lanxide Corporation  
 1001 Connecticut Avenue, N.W.  
 Washington DC 20036

Harry E. Eaton  
 United Technologies Corporation  
 Silver Lane  
 East Hartford CT 06108

Harvill C. Eaton  
 Louisiana State University  
 240 Thomas Boyd Hall  
 Baton Rouge LA 70803

Christopher A. Ebel  
 Carborundum Company  
 Technology Division  
 P.O. Box 832  
 Niagara Falls NY 14302-0832

J. J. Eberhardt  
 U.S. Department of Energy  
 Office of Transportation Mater's  
 CE-34, Forrestal Building  
 Washington DC 20585

Jim Edler  
 Eaton Corporation  
 26201 Northwestern Highway  
 P.O. Box 766  
 Southfield MI 48037

G. A. Eisman  
 Dow Chemical Company  
 Ceramics and Advanced Materials  
 52 Building  
 Midland MI 48667

William A. Ellingson  
 Argonne National Laboratory  
 Energy Technology Division  
 9700 S. Cass Avenue  
 Argonne IL 60439

Anita Kaye M. Ellis  
 Machined Ceramics  
 629 N. Graham Street  
 Bowling Green KY 42101

Glen B. Engle  
 Nuclear & Aerospace Materials  
 16716 Martincoit Road  
 Poway CA 92064

Jeff Epstein  
Ceramic Technologies, Inc.  
12739 Ashford Knoll  
Houston TX 77082

Kenneth A. Epstein  
Dow Chemical Company  
2030 Building  
Midland MI 48674

Art Erdemir  
Argonne National Laboratory  
9700 S. Cass Avenue  
Argonne IL 60439

E. M. Erwin  
Lubrizol Corporation  
1819 East 225th Street  
Euclid OH 44117

John N. Eustis  
U.S. Department of Energy  
Industrial Energy Efficiency Div  
CE-221, Forrestal Building  
Washington DC 20585

W. L. Everitt  
Kyocera International, Inc.  
8611 Balboa Avenue  
San Diego CA 92123

Gordon Q. Evison  
332 S. Michigan Avenue  
Suite 1730  
Chicago IL 60604

John W. Fairbanks  
U.S. Department of Energy  
Office of Propulsion Systems  
CE-322, Forrestal Building  
Washington DC 20585

Tim Fawcett  
Dow Chemical Company  
Advanced Ceramics Laboratory  
1776 Building  
Midland MI 48674

Robert W. Fawley  
Sundstrand Power Systems  
Div. of Sundstrand Corporation  
P.O. Box 85757  
San Diego CA 92186-5757

John J. Fedorchak  
GTE Products Corporation  
Hawes Street  
Towanda PA 18848-0504

Jeff T. Fenton  
Vista Chemical Company  
900 Threadneedle  
Houston TX 77079

Larry Ferrell  
Babcock & Wilcox  
Old Forest Road  
Lynchburg VA 24505

Raymond R. Fessler  
BIRL  
1801 Maple Avenue  
Evanston IL 60201

Ross F. Firestone  
Ross Firestone Company  
188 Mary Street  
Winnetka IL 60093-1520

Sharon L. Fletcher  
Arthur D. Little, Inc.  
15 Acorn Park  
Cambridge MA 02140-2390

Thomas F. Foltz  
Textron Specialty Materials  
2 Industrial Avenue  
Lowell MA 01851

Renee G. Ford  
Materials and Processing Report  
P.O. Box 72  
Harrison NY 10528

John Formica  
Supermaterials  
2020 Lakeside Avenue  
Cleveland OH 44114

Edwin Frame  
Southwest Research Institute  
P.O. Drawer 28510  
San Antonio TX 78284

Armanet Francois  
French Scientific Mission  
4101 Reservoir Road, N.W.  
Washington DC 20007-2176

R. G. Frank  
Technology Assessment Group  
10793 Bentley Pass Lane  
Loveland OH 45140

David J. Franus  
Forecast International  
22 Commerce Road  
Newtown CT 06470

Marc R. Freedman  
NASA Lewis Research Center  
21000 Brookpark Road, MS:49-3  
Cleveland OH 44135

Douglas Freitag  
Bayside Materials Technology  
17 Rocky Glen Court  
Brookeville MD 20833

Brian R.T. Frost  
Argonne National Laboratory  
9700 S. Cass Avenue, Bldg. 900  
Argonne IL 60439

Lawrence R. Frost  
Instron Corporation  
100 Royall Street  
Canton MA 02021

Xiren Fu  
Shanghai Institute of Ceramics  
1295 Ding-xi Road  
Shanghai 200050  
CHINA

J. P. Gallagher  
University of Dayton Research  
Institute  
300 College Park, JPC-250  
Dayton OH 45469-0120

Garry Garvey  
Golden Technologies Company Inc.  
4545 McIntyre Street  
Golden CO 80403

Richard Gates  
NIST  
Materials Bldg., A-256  
Gaithersburg MD 20899

L. J. Gauckler  
ETH-Zurich  
Sonneggstrasse 5  
CH-8092 Zurich 8092  
SWITZERLAND

George E. Gazza  
U.S. Army Materials Technology  
Ceramics Research Division  
405 Arsenal Street  
Watertown MA 02172-0001

D. Gerster  
CEA-DCOM  
33 Rue De La Federation  
Paris 75015  
FRANCE

John Ghinazzi  
Coors Technical Ceramics Company  
1100 Commerce Park Drive  
Oak Ridge TN 37830

Robert Giddings  
General Electric Company  
P.O. Box 8  
Schenectady NY 12301

A. M. Glaeser  
University of California  
Lawrence Berkeley Laboratory  
Hearst Mining Building  
Berkeley CA 94720

Joseph W. Glatz  
Naval Air Propulsion Center  
Systems Engineering Division  
510 Rocksville Road  
Holland PA 18966

W. M. Goldberger  
Superior Graphite Company  
R&D  
2175 E. Broad Street  
Columbus OH 43209

Allan E. Goldman  
U.S. Graphite, Inc.  
907 W. Outer Drive  
Oak Ridge TN 37830

Stephen T. Gonczy  
Allied Signal Research  
P.O. Box 5016  
Des Plaines IL 60017

Jeffrey M. Gonzales  
GTE Products Corporation  
Hawes Street  
Towanda PA 18848-0504

Robert J. Gottschall  
U.S. Department of Energy  
ER-131, MS:G-236  
Washington DC 20585

Earl Graham  
Cleveland State University  
Dept. of Chemical Engineering  
Euclid Avenue at East 24th Street  
Cleveland OH 44115

John W. Graham  
Astro Met, Inc.  
9974 Springfield Pike  
Cincinnati OH 45215

G. A. Graves  
U. of Dayton Research Institute  
300 College Park  
Dayton OH 45469-0001

Robert E. Green, Jr.  
Johns Hopkins University  
Materials Science and Engineering  
Baltimore MD 21218

Alex A. Greiner  
Plint & Partners  
Oaklands Park  
Wokingham Berkshire RG11 2FD  
UNITED KINGDOM

Lance Groseclose  
General Motors Corporation  
Allison Gas Turbine Division  
P.O. Box 420, MS:W-5  
Indianapolis IN 46206

Thomas J. Gross  
U.S. Department of Energy  
Transportation Technologies  
CE-30, Forrestal Building  
Washington DC 20585

Mark F. Gruninger  
Union Carbide Corporation  
Specialty Powder Business  
1555 Main Street  
Indianapolis IN 46224

Ernst Gugel  
Cremer Forschungsinstitut  
GmbH&Co.KG  
Oeslauer Strasse 35  
D-8633 Roedental 8633  
GERMANY

John P. Gyekenyesi  
NASA Lewis Research Center  
21000 Brookpark Road, MS:6-1  
Cleveland OH 44135

Nabil S. Hakim  
Detroit Diesel Corporation  
13400 Outer Drive West  
Detroit MI 48239

Philip J. Haley  
General Motors Corporation  
P.O. Box 420, MS:T12A  
Indianapolis IN 46236

Judith Hall  
Fiber Materials, Inc.  
Biddeford Industrial Park  
5 Morin Street  
Biddeford ME 04005

Y. Hamano  
Kyocera Industrial Ceramics Corp.  
5713 E. Fourth Plain Blvd.  
Vancouver WA 98661-6857

Y. Harada  
IIT Research Institute  
10 West 35th Street  
Chicago IL 60616

R. A. Harmon  
25 Schalren Drive  
Latham NY 12110

Norman H. Harris  
Hughes Aircraft Company  
P.O. Box 800520  
Saugus CA 91380-0520

Alan M. Hart  
Dow Chemical Company  
1776 Building  
Midland MI 48674

Pat E. Hart  
Battelle Pacific Northwest Labs  
Ceramics and Polymers Development  
P.O. Box 999  
Richland WA 99352

Michael H. Haselkorn  
Caterpillar Inc.  
Technical Center, Building E  
P.O. Box 1875  
Peoria IL 61656-1875

Debbie Haught  
U.S. Department of Energy  
Off. of Transportation Materials  
EE-34, Forrestal Bldg.  
Washington DC 20585

N. B. Havewala  
Corning Inc.  
SP-PR-11  
Corning NY 14831

John Haygarth  
Teledyne WAA Chang Albany  
P.O. Box 460  
Albany OR 97321

Norman L. Hecht  
U. of Dayton Research Institute  
300 College Park  
Dayton OH 45469-0172

Peter W. Heitman  
General Motors Corporation  
P.O. Box 420, MS:W-5  
Indianapolis IN 46206-0420

Robert W. Hendricks  
VPI & SU  
210 Holden Hall  
Blacksburg VA 24061-0237

Thomas L. Henson  
GTE Products Corporation  
Chemical & Metallurgical Division  
Hawes Street  
Towanda PA 18848

Thomas P. Herbell  
NASA Lewis Research Center  
21000 Brookpark Road, MS:49-3  
Cleveland OH 44135

Marlene Heroux  
Rolls-Royce, Inc.  
2849 Paces Ferry Road, Suite 450  
Atlanta GA 30339-3769

Robert L. Hershey  
Science Management Corporation  
1255 New Hampshire Ave., N.W.  
Suite 1033  
Washington DC 20036

Hendrik Heystek  
Bureau of Mines  
Tuscaloosa Research Center  
P.O. Box L  
University AL 35486

Robert V. Hillery  
GE Aircraft Engines  
One Neumann Way, M.D. H85  
Cincinnati OH 45215

Arthur Hindman  
Instron Corporation  
100 Royall Street  
Canton MA 02021

Hans Erich Hintermann  
CSEM  
Rue Breguet 2  
Neuchatel 2000  
SWITZERLAND

Shinichi Hirano  
Mazda R&D of North America, Inc.  
1203 Woodridge Avenue  
Ann Arbor MI 48105

Tommy Hiraoka  
NGK Locke, Inc.  
1000 Town Center  
Southfield MI 48075

Fu H. Ho  
General Atomics  
P.O. Box 85608  
San Diego CA 92186-9784

John M. Hobday  
U.S. Department of Energy  
Morgantown Energy Technology Ctr  
P.O. Box 880  
Morgantown WV 26507

Clarence Hoenig  
Lawrence Livermore National Lab  
P.O. Box 808, Mail Code L-369  
Livermore CA 94550

Thomas Hollstein  
Fraunhofer-Institut fur  
Werkstoffmechanik  
Wohlerstrasse 11  
79108 Freiburg  
GERMANY

Richard Holt  
National Research Council Canada  
Structures and Materials Lab  
Ottawa Ontario K1A 0R6  
CANADA

Woodie Howe  
Coors Technical Ceramics Company  
1100 Commerce Park Drive  
Oak Ridge TN 37830

Stephen M. Hsu  
NIST  
Gaithersburg MD 20899

Hann S. Huang  
Argonne National Laboratory  
9700 S. Cass Avenue  
Argonne IL 60439-4815

Gene Huber  
Precision Ferrites & Ceramics  
5576 Corporate Drive  
Cypress CA 90630

Harold A. Huckins  
Princeton Advanced Technology  
4 Bertram Place  
Hilton Head SC 29928

Fred R. Huettig  
Advanced Magnetics Inc.  
45 Corey Lane  
Mendham NJ 07945

Brian K. Humphrey  
Lubrizol Petroleum Chemicals Co.  
3000 Town Center, Suite 1340  
Southfield MI 48075-1201

Robert M. Humrick  
Dylon Ceramic Technologies  
3100 Edgehill Road  
Cleveland Heights OH 44118

Lorretta Inglehart  
National Science Foundation  
Division of Materials Research  
1800 "G" Street, N.W., Room 408  
Washington DC 20550

Michael S. Inoue  
Kyocera International, Inc.  
8611 Balboa Avenue  
San Diego CA 92123-1580



Joseph C. Jackson  
U.S. Advanced Ceramics Assoc.  
1600 Wilson Blvd., Suite 1008  
Arlington VA 22209

Osama Jadaan  
U. of Wisconsin-Platteville  
1 University Plaza  
Platteville WI 53818

Said Jahanmir  
NIST  
Materials Bldg., Room A-237  
Gaithersburg MD 20899

Curtis A. Johnson  
General Electric Company  
P.O. Box 8  
Schenectady NY 12301

Sylvia Johnson  
SRI International  
333 Ravenswood Avenue  
Menlo Park CA 94025

Thomas A. Johnson  
Lanxide Corporation  
P.O. Box 6077  
Newark DE 19714-6077

W. S. Johnson  
Indiana University  
One City Centre, Suite 200  
Bloomington IN 47405

Walter F. Jones  
AFOSR/NA  
110 Duncan Ave., Ste. B115  
Washington DC 20332-0001

Jill E. Jonkouski  
U.S. Department of Energy  
9800 S. Cass Avenue  
Argonne IL 60439-4899

L. A. Joo  
Great Lakes Research Corporation  
P.O. Box 1031  
Elizabethton TN 37643

A. David Joseph  
SPX Corporation  
700 Terrace Point  
Muskegon MI 49443

Adam Jostsons  
Australian Nuclear Science &  
Technology  
New Illawarra Road  
Lucas Heights New South Wales  
AUSTRALIA

Matthew K. Juneau  
Ethyl Corporation  
451 Florida Street  
Baton Rouge LA 70801

Tom Kalamasz  
Norton/TRW Ceramics  
7A-4 Raymond Avenue  
Salem NH 03079

Lyle R. Kallenbach  
Phillips Petroleum  
Mail Drop:123AL  
Bartlesville OK 74004

Nick Kamiya  
Kyocera Industrial Ceramics Corp.  
25 Northwest Point Blvd., #450  
Elk Grove Village IL 60007

Roy Kamo  
Adiabatics, Inc.  
3385 Commerce Park Drive  
Columbus IN 47201

Chih-Chun Kao  
Industrial Technology Research  
Institute  
195 Chung-Hsing Road, Sec. 4  
Chutung Hsinchu 31015 R.O.C.  
TAIWAN

Keith R. Karasek  
AlliedSignal Aerospace Company  
50 E. Algonquin Road  
Des Plaines IL 60017-5016

Martha R. Kass  
U.S. Department of Energy  
Oak Ridge Operations  
Building 4500N, MS:6269  
Oak Ridge TN 37831-6269

Robert E. Kassel  
Ceradyne, Inc.  
3169 Redhill Avenue  
Costa Mesa CA 92626

Allan Katz  
Wright Laboratory  
Metals and Ceramics Division  
Wright-Patterson AFB OH 45433

R. Nathan Katz  
Worcester Polytechnic Institute  
100 Institute Road  
Worcester MA 01609

Tony Kaushal  
Detroit Diesel Corporation  
13400 Outer Drive, West  
Detroit MI 48239-4001

Ted Kawaguchi  
Tokai Carbon America, Inc.  
375 Park Avenue, Suite 3802  
New York NY 10152

Noritsugu Kawashima  
TOSHIBA Corporation  
4-1 Ukishima-Cho  
Kawasaki-Ku Kawasaki 210  
JAPAN

Lisa Kempfer  
Penton Publishing  
1100 Superior Avenue  
Cleveland OH 44114-2543

Frederick L. Kennard, III  
AC Rochester  
1300 N. Dort Highway  
Flint MI 48556

David O. Kennedy  
Lester B. Knight Cast Metals Inc.  
549 W. Randolph Street  
Chicago IL 60661

George Keros  
Photon Physics  
3175 Penobscot Building  
Detroit MI 48226

Thomas Ketcham  
Corning, Inc.  
SP-DV-1-9  
Corning NY 14831

Pramod K. Khandelwal  
General Motors Corporation  
Allison Gas Turbine Division  
P.O. Box 420, MS:W05  
Indianapolis IN 46206

Jim R. Kidwell  
AlliedSignal Engines  
P.O. Box 52180  
Phoenix AZ 85072-2180

Shin Kim  
The E-Land Group  
19-8 ChangJeon-dong  
Mapo-gu, Seoul 121-190  
KOREA

W. C. King  
Mack Truck, Z-41  
1999 Pennsylvania Avenue  
Hagerstown MD 21740

Carol Kirkpatrick  
MSE, Inc.  
P.O. Box 3767  
Butte MT 59702

Tony Kim  
Caterpillar Inc.  
Defense Products Department, JB7  
Peoria IL 61629

James D. Kiser  
NASA Lewis Research Center  
21000 Brookpark Road, MS:49-3  
Cleveland OH 44135

Max Klein  
900 24th Street, N.W., Unit G  
Washington DC 20037

Richard N. Kleiner  
Golden Technologies Company  
4545 McIntyre Street  
Golden CO 80403

Stanley J. Klima  
NASA Lewis Research Center  
21000 Brookpark Road, MS:6-1  
Cleveland OH 44135

Albert S. Kobayashi  
University of Washington  
Mechanical Engineering Department  
Mail Stop:FU10  
Seattle WA 98195

Shigeki Kobayashi  
Toyota Central Research Labs  
Nagakute Aichi 480-11  
JAPAN

Richard A. Kole  
Z-Tech Corporation  
8 Dow Road  
Bow NH 03304

Joseph A. Kovach  
Eaton Corporation  
32500 Chardon Road  
Willoughby Hills OH 44094

Kenneth A. Kovaly  
Technical Insights Inc.  
P.O. Box 1304  
Fort Lee NJ 07024-9967

Ralph G. Kraft  
Spraying Systems Company  
North Avenue at Schmale Road  
Wheaton IL 60189-7900

Arthur Kranish  
Trends Publishing Inc.  
1079 National Press Building  
Washington DC 20045

A. S. Krieger  
Radiation Science, Inc.  
P.O. Box 293  
Belmont MA 02178

Pieter Krijgsman  
Ceramic Design International  
Holding B.V.  
P.O. Box 68  
Hattem 8050-AB  
THE NETHERLANDS

Waltraud M. Kriven  
University of Illinois  
105 S. Goodwin Avenue  
Urbana IL 61801

Edward J. Kubel, Jr.  
ASM International  
Advanced Materials & Processes  
Materials Park OH 44073

Dave Kupperman  
Argonne National Laboratory  
9700 S. Cass Avenue  
Argonne IL 60439

Oh-Hun Kwon  
North Company  
SGNICC/NRDC  
Goddard Road  
Northboro MA 01532-1545

W. J. Lackey  
GTRI  
Materials Science and Tech. Lab  
Atlanta GA 30332

Jai Lala  
Tenmat Ltd.  
40 Somers Road  
Rugby Warwickshire CV22 7DH  
ENGLAND

Hari S. Lamba  
General Motors Corporation  
9301 West 55th Street  
LaGrange IL 60525

Richard L. Landingham  
Lawrence Livermore National Lab  
P.O. Box 808, L-369  
Livermore CA 94550

James Lankford  
Southwest Research Institute  
6220 Culebra Road  
San Antonio TX 78228-0510

Stanley B. Lasday  
Business News Publishing Co.  
1910 Cochran Road, Suite 630  
Pittsburgh PA 15220

S. K. Lau  
Carborundum Company  
Technology Division  
P.O. Box 832, B-100  
Niagara Falls NY 14302

J. Lawrence Lauderdale  
Babcock & Wilcox  
1850 "K" Street, Suite 950  
Washington DC 20006

Jean F. LeCostaouec  
Textron Specialty Materials  
2 Industrial Avenue  
Lowell MA 01851

Benson P. Lee  
Technology Management, Inc.  
4440 Warrensville Rd., Suite A  
Cleveland OH 44128

Burtrand I. Lee  
Clemson University  
Olin Hall  
Clemson SC 29634-0907

June-Gunn Lee  
KIST  
P.O. Box 131, Cheong-Ryang  
Seoul 130-650  
KOREA

Ran-Rong Lee  
Ceramics Process Systems  
Corporation  
155 Fortune Boulevard  
Mildford MA 01757

Stan Levine  
NASA Lewis Research Center  
21000 Brookpark Road, MS:49-3  
Cleveland OH 44135

David Lewis, III  
Naval Research Laboratory  
Code 6370  
Washington DC 20375-5343

Ai-Kang Li  
Materials Research Labs., ITRI  
195-5 Chung-Hsing Road, Sec. 4  
Chutung Hsinchu 31015 R.O.C.  
TAIWAN

Winston W. Liang  
Hong Kong Industrial Technology  
Centre  
78 Tat Chee Avenue  
4/F, HKPC Building -- Kowloon  
HONG KONG

Robert Licht  
Norton Company  
SGNICC/NRDC  
Goddard Road  
Northboro MA 01532-1545

E. Lilley  
Norton Company  
SGNICC/NRDC  
Goddard Road  
Northboro MA 01532-1545

Chih-Kuang Lin  
National Central University  
Dept. of Mechanical Engineering  
Chung-Li 32054  
TAIWAN

Laura J. Lindberg  
AlliedSignal Aerospace Company  
Garrett Fluid Systems Division  
P.O. Box 22200  
Tempe AZ 85284-2200

Hans A. Lindner  
 Cremer Forschungsinstitut  
 GmbH&Co.KG  
 Oeslauer Strasse 35  
 D-8633 Rodental 8866  
 GERMANY

Ronald E. Loehman  
 Sandia National Laboratories  
 Chemistry & Ceramics Dept. 1840  
 P.O. Box 5800  
 Albuquerque NM 87185

Jeffrey C. Logas  
 Winona State University  
 115 Pasteur Hall  
 Winona MN 55987

Bill Long  
 Babcock & Wilcox  
 P.O. Box 11165  
 Lynchburg VA 24506

L. A. Lott  
 EG&G Idaho, Inc.  
 Idaho National Engineering Lab  
 P.O. Box 1625  
 Idaho Falls ID 83415-2209

Raouf O. Loutfy  
 MER Corporation  
 7960 S. Kolb Road  
 Tucson AZ 85706

Gordon R. Love  
 Aluminum Company of America  
 Alcoa Technical Center  
 Alcoa Center PA 15960

Lydia Luckevich  
 Ortech International  
 2395 Speakman Drive  
 Mississauga Ontario L5K 1B3  
 CANADA

James W. MacBeth  
 Carborundum Company  
 Structural Ceramics Division  
 P.O. Box 1054  
 Niagara Falls NY 14302

George Maczura  
 Aluminum Company of America  
 3450 Park Lane Drive  
 Pittsburgh PA 15275-1119

David Maginnis  
 Tinker AFB  
 OC-ALC/LIIRE  
 Tinker AFB OK 73145-5989

Frank Maginnis  
 Aspen Research, Inc.  
 220 Industrial Boulevard  
 Moore OK 73160

Tai-il Mah  
 Universal Energy Systems, Inc.  
 4401 Dayton-Xenia Road  
 Dayton OH 45432

Kenneth M. Mailliar  
 Barbour Stockwell Company  
 83 Linskey Way  
 Cambridge MA 02142

S. G. Malghan  
 NIST  
 I-270 & Clopper Road  
 Gaithersburg MD 20899

Lars Malmrup  
 United Turbine AB  
 Box 13027  
 Malmo S-200 44  
 SWEDEN

John Mangels  
 Ceradyne, Inc.  
 3169 Redhill Avenue  
 Costa Mesa CA 92626

Murli Manghnani  
 University of Hawaii  
 2525 Correa Road  
 Honolulu HI 96822

Russell V. Mann  
 Matec Applied Sciences, Inc.  
 75 South Street  
 Hopkinton MA 01748

William R. Manning  
Champion Aviation Products Div  
P.O. Box 686  
Liberty SC 29657

Ken Marnoch  
Amercom, Inc.  
8928 Fullbright Avenue  
Chatsworth CA 91311

Robert A. Marra  
Aluminum Company of America  
Alcoa Technical Center  
Alcoa Center PA 15069

Chauncey L. Martin  
3M Company  
3M Center, Building 60-1N-01  
St. Paul MN 55144

Steve C. Martin  
Advanced Refractory Technologies  
699 Hertel Avenue  
Buffalo NY 14207

Kelly J. Mather  
William International Corporation  
2280 W. Maple Road  
Walled Lake MI 48088

James P. Mathers  
3M Company  
3M Center, Bldg. 201-3N-06  
St. Paul MN 55144

Ron Mayville  
Arthur D. Little, Inc.  
15-163 Acorn Park  
Cambridge MA 02140

F. N. Mazadarany  
General Electric Company  
Bldg. K-1, Room MB-159  
P.O. Box 8  
Schenectady NY 12301

James W. McCauley  
Alfred University  
Binns-Merrill Hall  
Alfred NY 14802

Louis R. McCreight  
2763 San Ramon Drive  
Rancho Palos Verdes CA 90274

Colin F. McDonald  
McDonald Thermal Engineering  
1730 Castellana Road  
La Jolla CA 92037

B. J. McEntire  
Norton Company  
10 Airport Park Road  
East Granby CT 06026

Chuck McFadden  
Coors Ceramics Company  
600 9th Street  
Golden CO 80401

Thomas D. McGee  
Iowa State University  
110 Engineering Annex  
Ames IA 50011

Carol McGill  
Corning Inc.  
Sullivan Park, FR-02-08  
Corning NY 14831

James McLaughlin  
Sundstrand Power Systems  
4400 Ruffin Road  
P.O. Box 85757  
San Diego CA 92186-5757

Matt McMonigle  
U.S. Department of Energy  
Improved Energy Productivity  
CE-231, Forrestal Building  
Washington DC 20585

J. C. McVickers  
AlliedSignal Engines  
P.O. Box 52180, MS:9317-2  
Phoenix AZ 85072-2180

D. B. Meadowcroft  
"Jura," The Ridgeway  
Oxshott  
Leatherhead Surrey KT22 OLG  
UNITED KINGDOM

Joseph J. Meindl  
Reynolds International, Inc.  
6603 W. Broad Street  
P.O. Box 27002  
Richmond VA 23261-7003

Michael D. Meiser  
AlliedSignal, Inc.  
Ceramic Components  
P.O. Box 2960, MS:T21  
Torrance CA 90509-2960

George Messenger  
National Research Council of  
Canada  
Building M-7  
Ottawa Ontario K1A 0R6  
CANADA

D. Messier  
U.S. Army Materials Technology  
SLCMT-EMC  
405 Arsenal Street  
Watertown MA 02172-0001

Arthur G. Metcalfe  
Arthur G. Metcalfe and  
Associates, Inc.  
2108 East 24th Street  
National City CA 91950

R. Metselaar  
Eindhoven University  
P.O. Box 513  
Eindhoven 5600 MB  
THE NETHERLANDS

David J. Michael  
Harbison-Walker Refractories Co.  
P.O. Box 98037  
Pittsburgh PA 15227

Ken Michaels  
Chrysler Motors Corporation  
P.O. Box 1118, CIMS:418-17-09  
Detroit MI 48288

Bernd Michel  
Institute of Mechanics  
P.O. Box 408  
D-9010 Chemnitz  
GERMANY

D. E. Miles  
Commission of the European Comm.  
rue de la Loi 200  
B-1049 Brussels  
BELGIUM

Carl E. Miller  
AC Rochester  
1300 N. Dort Highway, MS:32-31  
Flint MI 48556

Charles W. Miller, Jr.  
Centorr Furnaces/Vacuum  
Industries  
542 Amherst Street  
Nashua NH 03063

R. Minimmi  
Enichem America  
2000 Cornwall Road  
Monmouth Junction NJ 08852

Michele V. Mitchell  
AlliedSignal, Inc.  
Ceramic Components  
P.O. Box 2960, MS:T21  
Torrance CA 90509-2960

Howard Mizuhara  
WESGO  
477 Harbor Boulevard  
Belmont CA 94002

Helen Moeller  
Babcock & Wilcox  
P.O. Box 11165  
Lynchburg VA 24506-1165

Francois R. Mollard  
Concurrent Technologies Corp.  
1450 Scalp Avenue  
Johnstown PA 15904-3374

Phil Mooney  
Panametrics  
221 Crescent Street  
Waltham MA 02254

Geoffrey P. Morris  
3M Company  
3M Traffic Control Materials  
Bldg. 209-BW-10, 3M Center  
St. Paul MN 55144-1000

Jay A. Morrison  
Rolls-Royce, Inc.  
2849 Paces Ferry Road, Suite 450  
Atlanta GA 30339-3769

Joel P. Moskowitz  
Ceradyne, Inc.  
3169 Redhill Avenue  
Costa Mesa CA 92626

Brij Moudgil  
University of Florida  
Material Science & Engineering  
Gainesville FL 32611

Christoph J. Mueller  
Sprechsaal Publishing Group  
P.O. Box 2962, Mauer 2  
D-8630 Coburg  
GERMANY

Thomas W. Mullan  
Vapor Technologies Inc.  
345 Route 17 South  
Upper Saddle River NJ 07458

Theresa A. Mursick-Meyer  
Norton Company  
SGNICC/NRDC  
Goddard Road  
Northboro MA 01532-1545

M. K. Murthy  
MkM Consultants International  
10 Avoca Avenue, Unit 1906  
Toronto Ontario M4T 2B7  
CANADA

David L. Mustoe  
Custom Technical Ceramics  
8041 West I-70 Service Rd. Unit 6  
Arvada CO 80002

Curtis V. Nakaishi  
U.S. Department of Energy  
Morgantown Energy Technology Ctr.  
P.O. Box 880  
Morgantown WV 26507-0880

Yoshio Nakamura  
Faicera Research Institute  
3-11-12 Misono  
Sagamihara, Tokyo  
JAPAN

Stefan Nann  
Roland Berger & Partner GmbH  
Georg-Glock-Str. 3  
40474 Dusseldorf  
GERMANY

K. S. Narasimhan  
Hoeganaes Corporation  
River Road  
Riverton NJ 08077

Robert Naum  
Applied Resources, Inc.  
P.O. Box 241  
Pittsford NY 14534

Malcolm Naylor  
Cummins Engine Company, Inc.  
P.O. Box 3005, Mail Code 50183  
Columbus IN 47202-3005

Fred A. Nichols  
Argonne National Laboratory  
9700 S. Cass Avenue  
Argonne IL 60439

H. Nickel  
Forschungszentrum Juelich (KFA)  
Postfach 1913  
D-52425 Juelich  
GERMANY



Dale E. Niesz  
Rutgers University  
Center for Ceramic Research  
P.O. Box 909  
Piscataway NJ 08855-0909

Paul W. Niskanen  
Lanxide Corporation  
P.O. Box 6077  
Newark DE 19714-6077

David M. Nissley  
United Technologies Corporation  
Pratt & Whitney Aircraft  
400 Main Street, MS:163-10  
East Hartford CT 06108

Bruce E. Novich  
Ceramics Process Systems Corp.  
155 Fortune Boulevard  
Milford MA 01757

Daniel Oblas  
50 Meadowbrook Drive  
Bedford MA 01730

Don Ohanehi  
Magnetic Bearings, Inc.  
1908 Sussex Road  
Blacksburg VA 24060

Hitoshi Ohmori  
ELID Team  
Itabashi Branch  
1-7 13 Kaga Itabashi  
Tokyo 173  
JAPAN

Robert Orenstein  
General Electric Company  
55-112, River Road  
Schenectady NY 12345

Norb Osborn  
Aerodyne Dallas  
151 Regal Row, Suite 120  
Dallas TX 75247

Richard Palicka  
Cercom, Inc.  
1960 Watson Way  
Vista CA 92083

Muktesh Paliwal  
GTE Products Corporation  
Hawes Street  
Towanda PA 18848

Joseph N. Panzarino  
Norton Company  
SGNICC/NRDC  
Goddard Road  
Northboro MA 01532-1545

Pellegrino Papa  
Corning Inc.  
MP-WX-02-1  
Corning NY 14831

Terry Paquet  
Boride Products Inc.  
2879 Aero Park Drive  
Traverse City MI 49684

E. Beth Pardue  
MPC  
8297 Williams Ferry Road  
Lenoir City TN 37771

Soon C. Park  
3M Company  
Building 142-4N-02  
P.O. Box 2963  
St. Paul MN 55144

Vijay M. Parthasarathy  
Caterpillar/Solar Turbines  
2200 Pacific Highway  
P.O. Box 85376  
San Diego CA 92186-5376

Harmut Paschke  
Schott Glaswerke  
Christoph-Dorner-Strasse 29  
D-8300 Landshut  
GERMANY

James W. Patten  
Cummins Engine Company, Inc.  
P.O. Box 3005, Mail Code 50183  
Columbus IN 47202-3005

Robert A. Penty  
Eastman Kodak Company  
Kodak Park  
Bldg., 326, 3rd Floor  
Rochester NY 14652-5120

Robert W. Pepper  
Textron Specialty Materials  
2 Industrial Avenue  
Lowell MA 01851

Peter Perdue  
Detroit Diesel Corporation  
13400 Outer Drive West,  
Speed Code L-04  
Detroit MI 48239-4001

John J. Petrovic  
Los Alamos National Laboratory  
Group MST-4, MS:G771  
Los Alamos NM 87545

Frederick S. Pettit  
University of Pittsburgh  
Pittsburgh PA 15261

Ben A. Phillips  
Phillips Engineering Company  
721 Pleasant Street  
St. Joseph MI 49085

Richard C. Phoenix  
Ohmtek, Inc.  
2160 Liberty Drive  
Niagara Falls NY 14302

Bruce J. Pletka  
Michigan Technological University  
Metallurgical & Materials Engr.  
Houghton MI 49931

John P. Pollinger  
AlliedSignal, Inc.  
Ceramic Components  
P.O. Box 2960, MS:T21  
Torrance CA 90509-2960

P. Popper  
High Tech Ceramics International  
Journal  
22 Pembroke Drive - Westlands  
Newcastle-under-Lyme  
Staffs ST5 2JN  
ENGLAND

F. Porz  
Universitat Karlsruhe  
Institut fur Keramik Im  
Maschinendau  
Postfach 6980  
D-76128 Karlsruhe  
GERMANY

Harry L. Potma  
Royal Netherlands Embassy  
Science and Technology  
4200 Linnean Avenue, N.W.  
Washington DC 20008

Bob R. Powell  
North American Operations  
Metallurgy Department  
Box 9055  
Warren MI 48090-9055

Stephen C. Pred  
ICD Group, Inc.  
1100 Valley Brook Avenue  
Lyndhurst NJ 07071

Karl M. Prewo  
United Technologies Research Ctr.  
411 Silver Lane, MS:24  
East Hartford CT 06108

Vimal K. Pujari  
Norton Company  
SGNICC/NRDC  
Goddard Road  
Northboro MA 01532-1545

George Quinn  
NIST  
Ceramics Division, Bldg. 223  
Gaithersburg MD 20899

Ramas V. Raman  
Ceracon, Inc.  
1101 N. Market Boulevard, Suite 9  
Sacramento CA 95834

Charles F. Rapp  
Owens Corning Fiberglass  
2790 Columbus Road  
Granville OH 43023-1200

Dennis W. Readey  
Colorado School of Mines  
Metallurgy and Materials Engr.  
Golden CO 80401

Wilfred J. Rebello  
PAR Enterprises, Inc.  
12601 Clifton Hunt Lane  
Clifton VA 22024

Harold Rechter  
Chicago Fire Brick Company  
7531 S. Ashland Avenue  
Chicago IL 60620

Robert R. Reeber  
U.S. Army Research Office  
P.O. Box 12211  
Research Triangle Park NC  
27709-2211

K. L. Reifsnider  
VPI & SU  
Engineering Science and Mechanics  
Blacksburg VA 24061

Paul E. Rempes  
McDonnell Douglass Aircraft Co.  
P.O. Box 516, Mail Code:0642263  
St. Louis MO 63166-0516

Gopal S. Revankar  
John Deere Company  
3300 River Drive  
Moline IL 61265

K. Y. Rhee  
Rutgers University  
P.O. Box 909  
Piscataway NJ 08854

James Rhodes  
Advanced Composite Materials Corp  
1525 S. Buncombe Road  
Greer SC 29651

Roy W. Rice  
W. R. Grace and Company  
7379 Route 32  
Columbia MD 21044

David W. Richerson  
2093 E. Delmont Drive  
Salt Lake City UT 84117

Tomas Richter  
J. H. France Refractories  
1944 Clarence Road  
Snow Shoe PA 16874

Michel Rigaud  
Ecole Polytechnique  
Campus Universite De Montreal  
P.O. Box 6079, Station A  
Montreal, P.Q. Quebec H3C 3A7  
CANADA

John E. Ritter  
University of Massachusetts  
Mechanical Engineering Department  
Amherst MA 01003

Frank L. Roberge  
AlliedSignal Engines  
P.O. Box 52180  
Phoenix AZ 85072-2180

W. Eric Roberts  
Advanced Ceramic Technology, Inc.  
990 "F" Enterprise Street  
Orange CA 92667

Y. G. Roman  
TNO TPD Keramick  
P.O. Box 595  
Eindhoven 5600 AN  
HOLLAND

Michael Rossetti  
Arthur D. Little, Inc.  
15 Acorn Park  
Cambridge MA 01240

Barry Rossing  
Lanxide Corporation  
P.O. Box 6077  
Newark DE 19714-6077

Steven L. Rotz  
Lubrizol Corporation  
29400 Lakeland Boulevard  
Wickliffe OH 44092

Robert Ruh  
Wright Laboratory  
WL/MLLM  
Wright-Patterson AFB OH 45433

Robert J. Russell  
17 Highgate Road  
Framingham MA 01701

Jon A. Salem  
NASA Lewis Research Center  
21000 Brookpark Road  
Cleveland OH 44135

W. A. Sanders  
NASA Lewis Research Center  
21000 Brookpark Road, MS:49-3  
Cleveland OH 44135

J. Sankar  
North Carolina A&T State Univ.  
Dept. of Mechanical Engineering  
Greensboro NC 27406

Yasushi Sato  
NGK Spark Plugs (U.S.A.), Inc.  
1200 Business Center Drive, #300  
Mt. Prospect IL 60056

Maxine L. Savitz  
AlliedSignal, Inc.  
Ceramic Components  
P.O. Box 2960, MS:T21  
Torrance CA 90509-2960

Ashok Saxena  
GTRI  
Materials Engineering  
Atlanta GA 30332-0245

David W. Scanlon  
Instron Corporation  
100 Royall Street  
Canton MA 02021

Charles A. Schacht  
Schacht Consulting Services  
12 Holland Road  
Pittsburgh PA 15235

Robert E. Schafrik  
National Materials Advisory Board  
2101 Constitution Ave., N.W.  
Washington DC 20418

James Schienle  
AlliedSignal Engines  
P.O. Box 52180, MS:1302-2P  
Phoenix AZ 85072-2180

John C. Schneider  
San Juan Technologies, Inc.  
3210 Arena Road  
Colorado Springs CO 80921-1503

Gary Schnittgrund  
Rocketdyne, BA05  
6633 Canoga Avenue  
Canoga Park CA 91303

Mark Schomp  
Lonza, Inc.  
17-17 Route 208  
Fair Lann NJ 07410

Joop Schoonman  
Delft University of Technology  
P.O. Box 5045  
2600 GA Delft  
THE NETHERLANDS

Robert B. Schulz  
U.S. Department of Energy  
Office of Transportation Matr's.  
CE-34, Forrestal Building  
Washington DC 20585

Murray A. Schwartz  
Materials Technology Consulting  
30 Orchard Way, North  
Potomac MD 20854

Peter Schwarzkopf  
SRI International  
333 Ravenswood Avenue  
Menlo Park CA 94025

William T. Schwessinger  
Multi-Arc Scientific Coatings  
1064 Chicago Road  
Troy MI 48083-4297

W. D. Scott  
University of Washington  
Materials Science Department  
Mail Stop:FB10  
Seattle WA 98195

Nancy Scoville  
Thermo Electron Technologies  
P.O. Box 9046  
Waltham MA 02254-9046

Thomas M. Sebestyen  
U.S. Department of Energy  
Advanced Propulsion Division  
CE-322, Forrestal Building  
Washington DC 20585

Brian Seegmiller  
Coors Ceramics Company  
600 9th Street  
Golden CO 80401

T. B. Selover  
AICRE/DIPPR  
3575 Traver Road  
Shaker Heights OH 44122

Charles E. Semler  
Semler Materials Services  
4160 Mumford Court  
Columbus OH 43220

Thomas Service  
Service Engineering Laboratory  
324 Wells Street  
Greenfield MA 01301

Kish Seth  
Ethyl Corporation  
P.O. Box 341  
Baton Rouge LA 70821

William J. Shack  
Argonne National Laboratory  
9700 S. Cass Avenue, Bldg. 212  
Argonne IL 60439

Peter T.B. Shaffer  
Technical Ceramics Laboratories,  
4045 Nine/McFarland Drive  
Alpharetta GA 30201

Richard K. Shaltens  
NASA Lewis Research Center  
21000 Brookpark Road, MS:302-2  
Cleveland OH 44135

Robert S. Shane  
1904 NW 22nd Street  
Stuart FL 34994-9270

Ravi Shankar  
Chromalloy  
Research and Technology Division  
Blaisdell Road  
Orangeburg NY 10962

Terence Sheehan  
Alpex Wheel Company  
727 Berkley Street  
New Milford NJ 07646

Dinesh K. Shetty  
University of Utah  
Materials Science and Engineering  
Salt Lake City UT 84112

Masahide Shimizu  
New Ceramics Association  
Shirasagi 2-13-1-208, Nakano-ku  
Tokyo 165  
JAPAN

Thomas Shreves  
American Ceramic Society, Inc.  
735 Ceramic Place  
Westerville OH 43081-8720

Jack D. Sibold  
Coors Ceramics Company  
4545 McIntyre Street  
Golden CO 80403

Johann Siebels  
Volkswagen AG  
Werkstofftechnologie  
Postfach 3180  
Wolfsburg 1  
GERMANY

George H. Siegel  
Point North Associates, Inc.  
P.O. Box 907  
Madison NJ 07940

Richard Silberglitt  
FM Technologies, Inc.  
10529-B Braddock Road  
Fairfax VA 22032

Mary Silverberg  
Norton Company  
SGNICC/NRDC  
Goddard Road  
Northboro MA 01532-1545

Gurpreet Singh  
Department of the Navy  
Code 56X31  
Washington DC 20362-5101

Maurice J. Sinnott  
University of Michigan  
5106 IST Building  
Ann Arbor MI 48109-2099

John Skildum  
3M Company  
3M Center  
Building 224-2S-25  
St. Paul MN 55144

Richard H. Smoak  
Smoak & Associates  
3554 Hollislope Road  
Altadena CA 91001-3923

Jay R. Smyth  
AlliedSignal Engines  
111 S. 34th Street, MS:503-412  
Phoenix AZ 85034

Rafal A. Sobotowski  
British Petroleum Company  
Technical Center, Broadway  
3092 Broadway Avenue  
Cleveland OH 44115

S. Somiya  
Nishi Tokyo University  
3-7-19 Seijo, Setagaya  
Tokyo 157  
JAPAN

Boyd W. Sorenson  
DuPont Lanxide Composites  
1300 Marrows Road  
Newark DE 19711

Charles A. Sorrell  
U.S. Department of Energy  
Advanced Industrial Concepts  
CE-232, Forrestal Building  
Washington DC 20585

C. Spencer  
EA Technology  
Capenhurst Chester CH1 6ES  
UNITED KINGDOM

Allen Spizzo  
Hercules Inc.  
Hercules Plaza  
Wilmington DE 19894

Richard M. Spriggs  
Alfred University  
Center for Advanced Ceramic  
Technology  
Alfred NY 14802

Charles Spuckler  
NASA Lewis Research Center  
21000 Brookpark Road, MS:5-11  
Cleveland OH 44135-3191

M. Srinivasan  
Material Solutions  
P.O. Box 663  
Grand Island NY 14702-0663

Gordon L. Starr  
Cummins Engine Company, Inc.  
P.O. Box 3005, Mail Code:50182  
Columbus IN 47202-3005

Tom Stillwagon  
AlliedSignal, Inc.  
Ceramic Components  
P.O. Box 2960, MS:T21  
Torrance CA 90509-2960

H. M. Stoller  
TPL Inc.  
3754 Hawkins, N.E.  
Albuquerque NM 87109

Paul D. Stone  
Dow Chemical USA  
1776 "Eye" Street, N.W., #575  
Washington DC 20006

F. W. Stringer  
Aero & Industrial Technology Ltd.  
P.O. Box 46, Wood Top  
Burnley Lancashire BB11 4BX  
UNITED KINGDOM

Thomas N. Strom  
NASA Lewis Research Center  
21000 Brookpark Road, MS:86-6  
Cleveland OH 44135

M. F. Stroosnijder  
Institute for Advanced Materials  
Joint Research Centre  
21020 Ispra (VA)  
ITALY

Karsten Styhr  
30604 Ganado Drive  
Rancho Palos Verdes CA 90274

T. S. Sudarshan  
Materials Modification, Inc.  
2929-P1 Eskridge Center  
Fairfax VA 22031

Glenn J. Sundberg  
Norton Company  
Goddard Road  
Northboro, MA 01532-1545

M. J. Sundaresan  
University of Miami  
P.O. Box 248294  
Coral Gables FL 33124

Patrick L. Sutton  
U.S. Department of Energy  
Office of Propulsion Systems  
CE-322, Forrestal Building  
Washington DC 20585

Willard H. Sutton  
United Technologies Corporation  
Silver Lane, MS:24  
East Hartford CT 06108

J. J. Swab  
U.S. Army Materials Technology  
Ceramics Research Division,  
SLCMT-EMC  
405 Arsenal Street  
Watertown MA 02172

Robert E. Swanson  
Metalworking Technology, Inc.  
1450 Scalp Avenue  
Johnstown PA 15904

Steve Szaruga  
Air Force Wright Aeronautical Lab  
WL/MLBC  
Wright-Patterson AFB OH  
45433-6533

Yo Tajima  
NGK Spark Plug Company  
2808 Iwasaki  
Komaki-shi Aichi-ken 485  
JAPAN

Fred Teeter  
5 Tralee Terrace  
East Amherst NY 14051

Monika O. Ten Eyck  
Carborundum Microelectronics  
P.O. Box 2467  
Niagara Falls NY 14302-2467

David F. Thompson  
Corning Glass Works  
SP-DV-02-1  
Corning NY 14831

Merle L. Thorpe  
Hobart Tafa Technologies, Inc.  
20 Ridge Road  
Concord NH 03301-3010

T. Y. Tien  
University of Michigan  
Materials Science and Engineering  
Dow Building  
Ann Arbor MI 48103

D. M. Tracey  
Norton Company  
SGNICC/NRDC  
Goddard Road  
Northboro MA 01532-1545

L. J. Trostel, Jr.  
Box 199  
Princeton MA 01541

W. T. Tucker  
General Electric Company  
P.O. Box 8, Bldg. K1-4C35  
Schenectady NY 12301

Masanori Ueki  
Nippon Steel Corporation  
1618 Ida  
Nakahara-Ku Kawasaki 211  
JAPAN

Filippo M. Ugolini  
ATA Studio  
Via Degli Scipioni, 268A  
ROMA, 00192  
ITALY

Donald L. Vaccari  
General Motors Corporation  
Allison Gas Turbines  
P.O. Box 420, Speed Code S49  
Indianapolis IN 46206-0420

Carl F. Van Conant  
Boride Products, Inc.  
2879 Aero Park Drive  
Traverse City MI 49684

Marcel H. Van De Voorde  
Commission of the European Comm.  
P.O. Box 2  
1755 ZG Petten  
THE NETHERLANDS

O. Van Der Biest  
Katholieke Universiteit Leuven  
Dept. Metaalkunde en Toegepaste  
de Croylaan 2  
B-3030 Leuven  
BELGIUM

Michael Vannier  
Washington University, St. Louis  
510 S. Kings Highway  
St. Louis MO 63110

Ara M. Vartabedian  
Norton Company  
Goddard Road  
Northboro, MA 01532-1545

Stan Venkatesan  
Southern Coke & Coal Corporation  
P.O. Box 52383  
Knoxville TN 37950

V. Venkateswaran  
Carborundum Company  
Niagara Falls R&D Center  
P.O. Box 832  
Niagara Falls NY 14302

Dennis Viechnicki  
U.S. Army Materials Technology  
405 Arsenal Street  
Watertown MA 02172-0001

Ted Vojnovich  
U.S. Department of Energy, ST-311  
Office of Energy Research, 3F077P  
Washington DC 20585



John D. Volt  
E.I. Dupont de Nemours & Co. Inc.  
P.O. Box 80262  
Wilmington DE 19880

John B. Wachtman  
Rutgers University  
P.O. Box 909  
Piscataway NJ 08855

Shigetaka Wada  
Toyota Central Research Labs  
Nagakute Aichi 480-11  
JAPAN

Janet Wade  
AlliedSignal Engines  
P.O. Box 52180, MS:1303-2  
Phoenix AZ 85072-2180

Jon A. Wade  
Norton Company  
Goddard Road  
Northboro, MA 01532-1545

Richard L. Wagner  
Ceramic Technologies, Inc.  
537 Turtle Creek South Dr., #24D  
Indianapolis IN 46227

J. Bruce Wagner, Jr.  
Arizona State University  
Center for Solid State Science  
Tempe AZ 85287-1704

Daniel J. Wahlen  
Kohler, Co.  
444 Highland Drive  
Kohler WI 53044

Ingrid Wahlgren  
Royal Institute of Technology  
Studsvik Library  
S-611 82 Nykoping  
SWEDEN

Ron H. Walecki  
AlliedSignal, Inc.  
P.O. Box 2960, MS:T21  
Torrance CA 90509-2960

Michael S. Walsh  
Vapor Technologies Inc.  
6300 Gunpark Drive  
Boulder CO 80301

Chien-Min Wang  
Industrial Technology Research  
Institute  
195 Chung-Hsing Road, Sec. 4  
Chutung Hsinchu 31015 R.O.C.  
TAIWAN

Robert M. Washburn  
ASMT  
11203 Colima Road  
Whittier CA 90604

Gerald Q. Weaver  
Carborundum Specialty Products  
42 Linus Allain Avenue  
Gardner MA 01440-2478

Kevin Webber  
Toyota Technical Center, U.S.A.  
1410 Woodridge, RR7  
Ann Arbor MI 48105

Karen E. Weber  
Detroit Diesel Corporation  
13400 Outer Drive West  
Detroit MI 48239-4001

James K. Weddell  
Du Pont Lanxide Composites Inc.  
P.O. Box 6100  
Newark DE 19714-6100

R. W. Weeks  
Argonne National Laboratory  
MCT-212  
9700 S. Cass Avenue  
Argonne IL 60439

Ludwig Weiler  
ASEA Brown Boveri AG  
Eppelheimer Str. 82  
D-6900 Heidelberg  
GERMANY

James Wessel  
Dow Corning Corporation  
1800 "M" Street, N.W., #325 South  
Washington DC 20036

Robert D. West  
Therm Advanced Ceramics  
P.O. Box 220  
Ithaca NY 14851

Thomas J. Whalen  
Ford Motor Company  
SRL Bldg., Mail Drop 2313  
P.O. Box 2053  
Dearborn MI 48121-2053

Charles S. White  
Norton Company  
Goddard Road  
Northboro, MA 01532-1545

Ian A. White  
Hoeganaes Corporation  
River Road  
Riverton NJ 08077

Sheldon M. Wiederhorn  
NIST  
Building 223, Room A329  
Gaithersburg MD 20899

John F. Wight  
Alfred University  
McMahon Building  
Alfred NY 14802

D. S. Wilkinson  
McMaster University  
1280 Main Street, West  
Hamilton Ontario L8S 4L7  
CANADA

James C. Williams  
General Electric Company  
Engineering Materials Technology  
One Neumann Way, Mail Drop:H85  
Cincinnati OH 45215-6301

Steve J. Williams  
RCG Hagler Bailly, Inc.  
1530 Wilson Boulevard, Suite 900  
Arlington VA 22209-2406

Thomas A. Williams  
National Renewable Energy Lab  
1617 Cole Boulevard  
Golden CO 80401

Craig A. Willkens  
Norton Company  
SGNICC/NRDC  
Goddard Road  
Northboro MA 01532-1545

Roger R. Wills  
TRW, Inc.  
Valve Division  
1455 East 185th Street  
Cleveland OH 44110

David Gordon Wilson  
Massachusetts Institute of  
Technology  
77 Massachusetts Ave., Room 3-455  
Cambridge MA 02139

Matthew F. Winkler  
Seaworthy Systems, Inc.  
P.O. Box 965  
Essex CT 06426

Gerhard Winter  
Hermann C. Starck Berlin GmbH  
P.O. Box 25 40  
D-3380 Goslar 3380  
GERMANY

William T. Wintucky  
NASA Lewis Research Center  
Terrestrial Propulsion Office  
21000 Brookpark Road, MS:86-6  
Cleveland OH 44135

Thomas J. Wissing  
Eaton Corporation  
Engineering and Research Center  
P.O. Box 766  
Southfield MI 48037

James C. Withers  
MER Corporation  
7960 S. Kolb Road  
Building F  
Tucson AZ 85706

Dale E. Wittmer  
Southern Illinois University  
Mechanical Engineering Department  
Carbondale IL 62901

Warren W. Wolf  
Owens Corning Fiberglass  
2790 Columbus Road, Route 16  
Granville OH 43023

Egon E. Wolff  
Caterpillar Inc.  
Technical Center  
P.O. Box 1875  
Peoria IL 61656-1875

George W. Wolter  
Howmet Turbine Components Corp.  
Technical Center  
699 Benston Road  
Whitehall MI 49461

James C. Wood  
NASA Lewis Research Center  
21000 Brookpark Road, MS:86-6  
Cleveland OH 44135

Marrill Wood  
LECO Corporation  
P.O. Box 211688  
Augusta GA 30917-1688

Wayne L. Worrell  
University of Pennsylvania  
3231 Walnut Street  
Philadelphia PA 19104

John F. Wosinski  
Corning Inc.  
ME-2 E-5 H8  
Corning NY 14830

Ian G. Wright  
BCL  
505 King Avenue  
Columbus OH 43201

Ruth Wroe  
ERDC  
Capenhurst Chester CH1 6ES  
ENGLAND

Bernard J. Wrona  
Advanced Composite Materials Corp  
1525 S. Buncombe Road  
Greer SC 29651

Carl C. M. Wu  
Naval Research Laboratory  
Ceramic Branch, Code 6373  
Washington DC 20375

John C. Wurst  
U. of Dayton Research Institute  
300 College Park  
Dayton OH 45469-0101

Neil Wyant  
ARCH Development Corp.  
9700 S. Cass Avenue, Bldg. 202  
Argonne IL 60439

Roy Yamamoto  
Texaco Inc.  
P.O. Box 509  
Beacon NY 12508-0509

John Yamanis  
AlliedSignal Aerospace Company  
P.O. Box 1021  
Morristown NJ 07962-1021

Harry C. Yeh  
AlliedSignal, Inc.  
Ceramic Components  
P.O. Box 2960, MS:T21  
Torrance CA 90509-2960

Hiroshi Yokoyama  
Hitachi Research Lab  
4026 Kuji-Cho  
Hitachi-shi Ibaraki 319-12  
JAPAN

Thomas M. Yonushonis  
Cummins Engine Company, Inc.  
P.O. Box 3005, Mail Code 50183  
Columbus IN 47202-3005

Thomas J. Yost  
Corning Inc.  
Technical Products Div., 21-1-2  
Corning NY 14831

Jong Yung  
Sundstrand Aviation Operations  
4747 Harrison Avenue  
Rockford IL 61125

A. L. Zadoks  
Caterpillar Inc.  
Technical Center, Building L  
P.O. Box 1875  
Peoria IL 61656-1875

Avi Zangvil  
University of Illinois  
104 S. Goodwin Avenue  
Urbana IL 61801

Charles H. Zenuk  
Transtech  
6662 E. Paseo San Andres  
Tucson AZ 85710-2106

Carl Zweben  
General Electric Company  
P.O. Box 8555, VFSC/V4019  
Philadelphia PA 19101

Department of Energy  
Oak Ridge Operations Office  
Assistant Manager for Energy  
Research and Development  
P.O. Box 2001  
Oak Ridge, TN 37831-8600

Department of Energy (2)  
Office of Scientific and  
Technical  
Information  
Office of Information Services  
P.O. Box 62  
Oak Ridge, TN 37831

For distribution by microfiche  
as shown in DOE/OSTI-4500,  
Distribution Category UC-332  
(Ceramics/Advanced Materials).